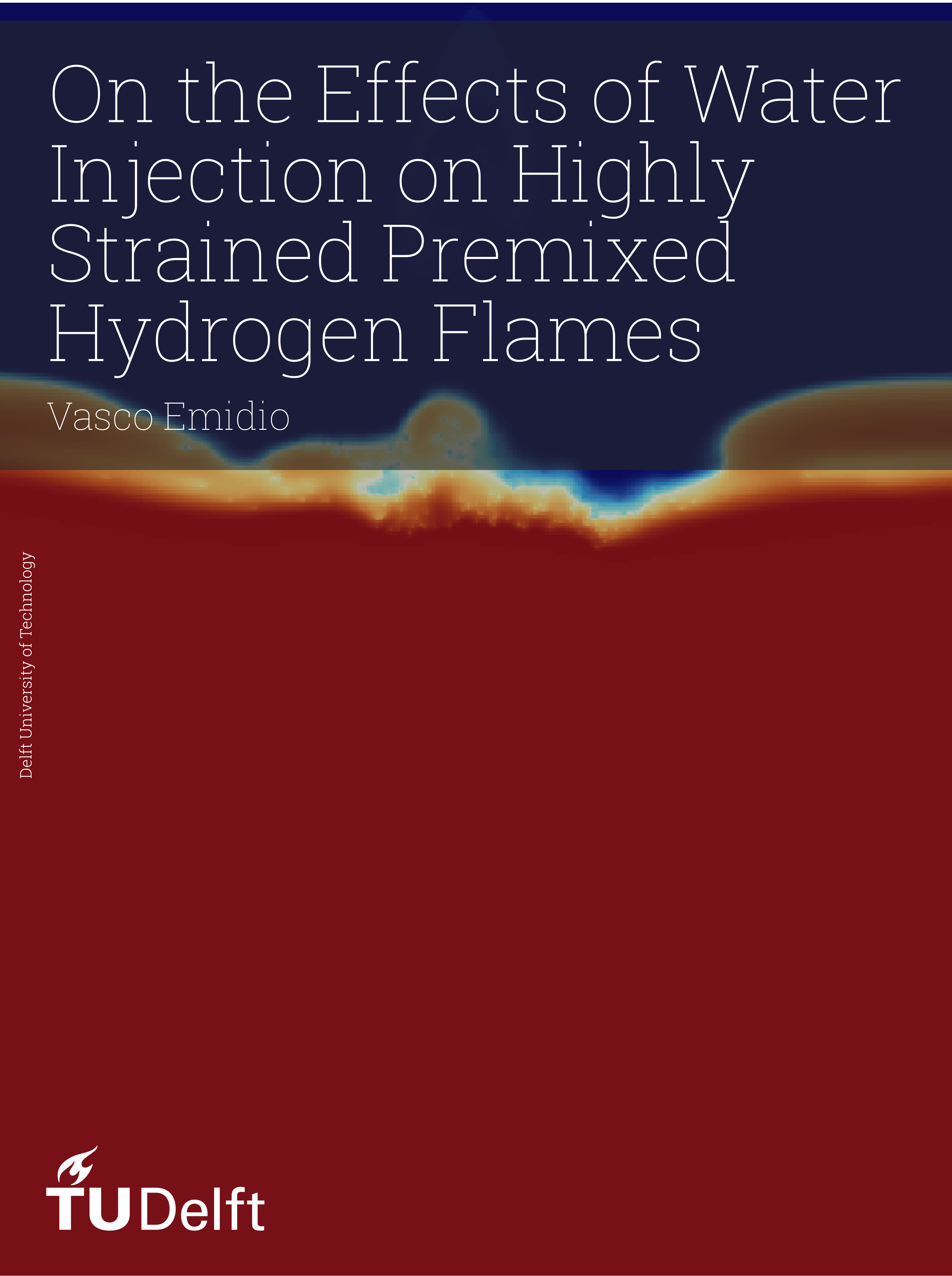

On the Effects of Water Injection on Highly Strained Premixed Hydrogen Flames

Vasco Emidio

Delft University of Technology

On the Effects of Water Injection on Highly Strained Premixed Hydrogen Flames

by

Vasco Emidio

to obtain the degree of Master of Science
at the Delft University of Technology,
to be defended publicly on Monday April 1, 2026 at 11:30 AM.

Student number:	5844746	
Project duration:	March 3, 2025 – April 1, 2026	
Thesis committee:	Dr. I. Langella,	TU Delft, supervisor
	Prof. Dr. S. Hickel,	TU Delft, chair
	Dr. F. De Domenico,	TU Delft, examiner

Acknowledgments

This thesis is not only the culmination of my last year of work, but most importantly the culmination of my time as a university student. This project was also the perfect mirror to my life as a student as it was filled with delays and complications, some due to the consequences of my own actions and some because (in the words of my favorite comedian, Brennan Lee Mullingan) “Luck is [...] an acknowledgment of the preponderance of factors outside of any one individual’s control”. The last two and a half years as a TU Delft student have taken me places I could never imagine and allowed me to experience life in two new countries, to meet new and diverse individuals from different cultural and socioeconomic backgrounds, and most importantly it allowed me to grow and get to know sides of myself I didn’t know existed. Reflecting on this journey and the circumstances that led to this moment, I can’t help but smile as I realize the many ways I reinvented myself to deal with the ups and downs this adventure threw at me and all of them make this project all the more meaningful and this graduation all the more significant.

This journey and this thesis could not have been completed without the help and guidance of many individuals, all of which are worth acknowledging. Firstly, I would like to express my most sincere thanks to my supervisor, Dr. Ivan Langella, for allowing me to take on this thesis research project and for his guidance and support over its entire duration. Moreover, I also have to thank Marisa and Vittorio , the two PhD candidates that supported and helped me infinitely throughout this project. Without their patience and help I have serious doubts I would finish this project.

Secondly, I would like to thank my Aeroamigos: Delille, Joana, Pedro, Ricardo, and Zé. Without them my academic life would have been a lot more gray. Thank you for being there for me and I am sorry for all the venting you have endured on my end. I owe all of you a café in Civil, even if we no longer attend IST. Additionally, I would also like to thank Adam, Alin, Diogo, and Sérgio for being the first friends I made in Delft.

Thirdly, I would like to thank my group of friends from high school, in particular my two closest friends: Tiago Escrata and Gillo. You saw me grow and change, you have stood by me as I became an adult and always offered kind words and friendship when I needed the most. You also motivated me to keep going when all I could think of was giving up. I want to thank you both for all the late night talks, all the laughs, all the memes, and all the silly jokes.

Finally, and most importantly, I would like to thank my family. My step-father, Filipe, who truly was the father that stepped up and has watched me become the man I am today. To my younger brother Tiago, that keeps making me infinitely proud of being his older brother and is at the same time my biggest hater and my most loyal fan. And the biggest and most sincere thanks to my mother, Rute, whose love and support allowed me to grow and explore life in another country. I know it hasn’t always been easy, but thank you for always believing in me.

Since every new beginning is some other beginning’s end, as this beginning’s conclusion arises, I can’t help but wonder what my next beginning will be, but that is a problem for future me. On high we go!

Vasco Emidio
Delft, March 2026

Abstract

The aerospace industry is under increasing pressure to reduce emissions and transition toward a more sustainable future. With recent technological advances and stronger emphasis on environmental protection, liquid hydrogen has gained attention as an alternative fuel for civil aviation due to its favorable thermochemical properties, including low minimum ignition energy, wide flammability limits, high energy content, and potential as a zero-carbon alternative to fossil fuels. However, operating hydrogen under such conditions presents challenges, including potentially higher engine-out NO_x emissions due to higher flame temperatures, onboard storage difficulties, higher laminar flame speeds, and an adiabatic stoichiometric flame temperature higher than that of natural gas. To mitigate NO_x formation, water injection has emerged as a possible method due to water's high specific heat capacity and latent heat of evaporation absorb heat and lower combustion temperatures, with liquid water injection generally proving more effective than steam. Additionally, introducing flame strain has emerged as another potential strategy as highly strained flames have shown promising results for reducing NO_x emissions. This thesis aims to qualitatively and quantitatively analyze the effect of water injection on highly strained premixed laminar hydrogen flames through the use of computational methods and in this way infer the possibility of combining these two methods to reduce NO_x emissions in hydrogen combustion. In order to do that, Direct Numerical Simulations (DNS) of highly strained hydrogen flames with water injection with different setups were performed to conducted a parametric analysis of the effect of spray injection velocity, droplet diameter, and strain rate on the flame structure and emissions of NO_x related species. The results revealed that for the baseline case with water injection a sharp reduction in the presence of key flame radicals and reductions in hydrogen reactivity and domain temperature, which lead to reductions of NNH, N_2O, and NO emissions. These effects are enhanced with increasing water injection velocity likely due to the increasing momentum resulting in the evaporation of the droplet occurring closer to the flame front. Regarding the effect of increasing droplet diameter, it was verified that increasing diameters are also associated with larger reductions in NO emissions and radical presence, likely due to the higher droplet volume requiring more energy to evaporate and therefore evaporation occurring closer to the flame front. In a computational setup with a flame with higher strain rate than the baseline case, when injected with water at similar water loading, the reductions in radical compositions, hydrogen rate of production and NO emissions are more significant in the case with higher bulk flame strain rate. From these results, it can be concluded that increasing droplet diameter and water injection velocity has positive effects on reducing emissions of NO_x related species. Furthermore, it can also be concluded that higher strain rates enhance the effects of water injection, presenting sharper reductions in key radicals and emissions of NO_x related species.

Keywords: Hydrogen; Flame; Water Injection; Emissions; NO_x; Strain Rate; Stretch; Flame Structure; Parametric Study

Contents

List of Figures

List of Tables

Nomenclature

Abbreviations

Abbreviation	Definition
DNS	Direct Numerical Simulations
LES	Large Eddy Simulations
SMD	Standard Mean Diameter

Symbols

Symbol	Definition	Unit
A	Drying Factor	[-]
a	Strain Rate	[s$^{-}1$]
B	Arrhenius factor	[m^3/(mol · s)]
C_d	Drag Coefficient	[-]
$c(\mathrm{H}_2)$	Progress Variable	[-]
C_p	Heat Capacity	[J/K]
c_p	Specific Heat Capacity	[J/(K · kg)]
d	Diameter	[m]
F_{lift}	Lift Force	[N]
h	Enthalpy	[J]
k	Rate constant	[m^3/(mol · s)]
Le	Lewis Number	[-]
m	Mass	[kg]
Nu	Nusselt Number	[-]
p	Pressure	[Pa]
Pr	Prandtl Number	[-]
R	Ideal Gas Constant	[J/K · mol]
Re	Reynolds Number	[-]
Sc	Schmidt Number	[-]
Sh	Sherwood Number	[-]
T	Temperature	[K]
t	Time	[s]
U	Velocity	[m/s]
V_k	Species Diffusion Velocity	[m/s]
W	Molecular Weight	[-]

Symbol	**Definition**	**Unit**
Y_k	Mass Fraction of Species k	[-]
Z_{bilger}	Bilger Mixture Fraction	[-]
Z_k	Elemental Mass Fraction	[-]
α	Thermal Diffusivity	[m^2/s]
γ_k	Weighting Factor of Each Element	[-]
Γ	Gamma Function	[-]
λ	Air–fuel equivalence ratio	[-]
μ	Dynamic Viscosity	[Pa $\cdot$ s]
ρ	Density	[kg/m^3]
$\dot{\omega}$	Molar Production Rates	[mol/s]
ϕ	Fuel–air Equivalence Ration	[-]
θ	Cone Angle	[deg]

Chemical species

Symbol	**Chemical Species**
CH	Methylidyne Radical
CHn	Hydrocarbon Radicals
CN	Cyanide
CO	Carbon Monoxide
CO_2	Carbon Dioxide
H	Hydrogen Radical
HO_2	Hydroperoxyl Radical
H_2	Molecular Hydrogen
H_2O	Water
H_2O_2	Hydrogen Peroxide
N	Nitrogen Radical
N_2	Molecular Nitrogen
NCN	NCN Radical
NCO	Isocyanate Radical
NH	Nitrogen Hydride
NH_2	Amidogen
NNH	Diazynium
N_2O	Nitrous Oxide
NO	Nitric Oxide
NO_2	Nitric Dioxide
NOx	Nitric Oxides
O	Oxygen Radical
O_2	Molecular Oxygen
OH	Hydroxyl Radical

1

Introduction

As the world faces the rise of the effects associated with climate change, the global energy demand is still on the rise with world energy consumption being projected to grow by about 0.7% annually until 2040 [1]. Currently, more than 70% of the world's energy demand is satisfied by fossil fuels and about 90% of all of it originates from combustion, which significantly contribute for the aggravation of the current climate change situation by increasing the amount of green house gas emissions [1, 2]. Some renewable energy sources, like wind turbines, have fluctuating energy production and, as such, robust and flexible backup facilities become more crucial for electrical grid stability [3, 4]. Similarly, due to the various effects of climate change and its consequences on human lives and society, the aerospace industry is facing an increasingly amount of pressure to reduce emissions and move towards a greener and more sustainable future. However, diminishing results have been achieved towards this goal despite the technological improvements made to the current engines being utilized in civil aviation [5]. Specially since the amount of passengers and business jet operations is expected to continuously rise until 2050, and with it greenhouse gases and NO_x emissions as well [6].

With current day technological advances and with emphases on environmental protection and emission reductions, the potential of utilizing liquid hydrogen as an alternative fuel for civil aviation has become more relevant [7], with companies investing in research on this topic [8, 9]. Hydrogen has extremely desirable characteristics for a fuel: it has excellent thermochemical properties such as low minimum ignition energy, wide flammability limits, a high energy content, and has the potential to be a zero-carbon fuel alternative to conventional fossil fuels [10, 11]. Moreover, hydrogen's characteristic molecular diffusivity facilitates mixing, while its high flame speed results in a lower residence time, which together may allow for shorter combustor lengths [9]. However, operating hydrogen under these conditions raises serious challenges and concerns, such as an potential increase of engine-out NOx emissions due to potentially higher flame temperatures, but also vehicular on-board storage challenges. Moreover, the higher reactivity of hydrogen also leads to a higher laminar flame speed and the adiabatic stoichiometric flame temperature of a hydrogen flame is about 150 K higher than that of a natural gas flame. The ignition delay time, which is is the time required for a mixture of fuel and oxidizer to react at a certain temperature and pressure, has also shown to be shorter with increasing hydrogen content in fuel components. Furthermore, due to the high reactivity of hydrogen, flashback and auto-ignition are also more prone to occur [4, 11, 12].

Humidification and water injection into hydrogen combustion have emerged has potential methods to reduce NOx emissions by reducing hydrogen reactivity and lower the flame temperature [4]. This is possible due to water's high specific heat capacity and latent heat of evaporation, which absorbs heat from the combustion process, and thus decreasing its temperature and, consequently, NOx emissions. Liquid water injection is has shown to be more effective at this than water steam since additional energy for evaporation is required. Moreover, steam also changes the NOx formation since it alters the main reaction pathways, which may further reduce NOx emissions due to suppression of radicals necessary for these species formation [4, 13].

Another emergent method to reduce NOx emissions in hydrogen flames is the addition of flame strain to the combustion process. Flame strain rate is one of the main contributors towards flame stretch and hydrogen flames have been shown to present an increasing consumption speed as the strain rate is increased due to its negative Markstein length. Moreover, highly strained hydrogen flames have shown promising results when it comes to reducing NOx emissions [14, 15], with Porcarelli, Kruljević, and Langella [14] having identified that this suppression occurs mainly on the thermal NOx mechanism without reducing the reactivity of the fuel.

This thesis aims to qualitatively and quantitatively analyze the effect of water injection on highly strained premixed laminar hydrogen flames through the use of computational methods and in this way infer about the possibility of combining these two methods in order to reduce NOx emissions in hydrogen combustion.

1.1. Thesis Structure

The structure of the thesis report is as follows:

In chapter 2, a literature review on the effects of water injection and high-strain-rate conditions on hydrogen premixed flames is presented. The main NOx formation mechanisms are discussed and the chemical species involved identified. Then, the effects of water injection in a multitude of flame conditions, both experimental and numerical, are analyzed based on studies and trends from the current literature. The primary focus is on the effects of water injection on flame structure and emissions, with a brief discussion of its flashback-prevention potential. To conclude this chapter, an analysis on the behavior of hydrogen premixed flames under high-strain conditions is done.

In chapter 3, the topic's background and research relevance are discussed. A brief discussion and exposure of the research gaps identified upon the makings of the literature review is presented. The chapter concludes with the formulation of the thesis proposal and research questions that guide its scientific process.

A description of the overall methodology employed for the purposes of studying the effects of water injection in highly strained hydrogen flames and that was used to guide this thesis project is presented in chapter 4. An overview of the mathematical model, the mathematical approach, and the numerical model used is provided, which includes the reduced chemical mechanism employed, the droplet modeling approach, and the variable definition used to quantify emission reductions and post process the attained results. A sensitivity analysis of the model used is also presented and briefly analyzed. This chapter concludes with the exposition of a simulation matrix, that provides information regarding the parameters varied for each case studied analyzed.

In chapter 5 the results obtained for all the numerical simulations made are exposed and discussed. Firstly, the results for the baseline simulation with water injection will be exposed and analyzed. The flame structure is analyzed in terms of radical mass fractions, temperature profiles, and hydrogen consumption rate. Moreover, the effect of water injection on the flame is further evaluated in terms of its impact on NO_x emissions. Once the baseline results are presented and discussed, a parametric analysis will be performed to assess the effect of water injection parameters. In particular, the injection velocity, standard mean diameter (SMD), and strain rate will be systematically varied, and the results will be compared with the baseline case in order to evaluate their impact.

Finally, chapter 6 provides a summary of the overall findings, whilst also providing an outline and directions for future research based on the results and goals of this thesis project.

2

Literature Review

In this chapter, a comprehensive literature review on the effects of water injection and high-strain-rate conditions on hydrogen premixed flames is presented; however, firstly an overview of the NOx formation mechanisms is presented, with a focus on the more relevant pathways of NOx formation in hydrogen flames.

Subsequently, the effects of water injection in a multitude of flame conditions, both experimental and numerical, are analyzed based on studies and trends from the current literature. The primary focus is on the effects of water injection on flame structure and emissions, with a brief discussion of its flashback-prevention potential.

Finally, a section focused on the behavior of hydrogen premixed flames under high-strain conditions, highlighting literature findings on the impact of strain on emissions.

2.1. NOx Formation Mechanisms

In order to analyze how water injection impacts NOx emissions in flames, it first necessary to grasp how nitrogen oxides are most commonly formed in hydrogen flames. The most common nitrogen oxides found in hydrogen flames are NO, NO_2, and N_2O, with NO being the most common of them once the combustion process is concluded, but is subsequently oxidized to NO_2 in the atmosphere [16, 17]. When in the atmosphere, NO and NO_2 act as precursors to acid rain and are a key element in the formation of photochemical smog, whilst N_2O is a greenhouse gas with a fairly long lifetime (around 150 to 200 years) in the troposphere [16, 18]. Moreover, these chemical species are responsible for a reduction of ozone (O_3) in the troposphere (where it is vital to protect the planet from the ultraviolet rays), whilst promoting its formation in the stratosphere [19]. Reducing NOx emissions is vital and the formation of these species is tied with numerous factors, such as residence time, temperature, equivalence ratio, and pressure. The main formation pathways for NO are as follows:

- **Zeldovich or Thermal NOx Mechanism:** The Zeldovich mechanism is the most relevant source of NOx formation at elevated temperatures (above 1894 K [20]). It is a well know and studied mechanism and its first step is an attack from an oxygen atom into the triple bond present in the N_2 molecule [16, 21].
  - R1: $N_2 + O \rightleftharpoons NO + N \quad k_1 = 1.8 \cdot 10^{14}\ \text{exp}(-318\ \text{kJ·mol}^{-1}/(RT))\ \text{cm}^3/(\text{mol·s})$

  Afterwards, the nitrogen atom will quickly oxidize by reacting with either OH or O_2:

  - R2: $N + O_2 \rightleftharpoons NO + O \quad k_2 = 6.4 \cdot 10^{9}\, T\ \text{exp}(-26\ \text{kJ·mol}^{-1}/(RT))\ \text{cm}^3/(\text{mol·s})$
  - R3: $N + OH \rightleftharpoons NO + H \quad k_3 = 3.8 \cdot 10^{13}\ \text{cm}^3/(\text{mol·s})$

  The first reaction is the rate limiting step when it comes to thermal NOx formation due to its very high activation energy caused by the triple bond present in the N_2 molecule. When water is injected into a flame, the humidity will promote the reaction $O + H_2O \rightleftharpoons OH + OH$ which will cause a deficit in O radicals, leading to a reduction in thermal NOx formed. Moreover, the increase in humidity will also cause a reduction in flame temperature, which translates to a deficit of energy necessary to fulfill the high activation energy requirements of the first reaction, further reducing emissions caused by this NOx formation mechanism [20, 21].

- **N_2O Mechanism:** In fuel-lean flames, at moderate temperatures and elevated pressures the N_2O pathway gains a lot of significance. This mechanisms initiates with the recombination of molecular nitrogen into N_2O by reacting with oxygen radicals [16]:

  - R4: $O + N_2$ (+M)$\rightleftharpoons$ N_2O (+M)

  The N_2O can then react with atomic hydrogen or oxidize with atomic oxygen, producing NO:

  - R5: N_2O + H$\rightleftharpoons$ NH + NO
  - R6: N_2O + O$\rightleftharpoons$ NO + NO

  This mechanism can be suppressed if reaction R4 is made to proceed backwards. Water injection can help doing this due to provoking a deficit in O radicals present in the environment, similar to the aforementioned Zeldovich mechanism, however the lower temperature caused by injecting water may also make this mechanism comparatively relevant [17, 20].

- **NNH Pathway:** Similar to the N_2O mechanism, this mechanism starts with the recombination of molecular nitrogen, but this time by reacting with atomic hydrogen radicals to form NNH:

  - R7: $H + N_2$ (+M)$\rightleftharpoons$ NNH (+M)

  The formed NNH will then react with either atomic oxygen or OH to give origin to NO:

  - R8: NNH + O$\rightleftharpoons$ NH + NO
  - R9: NNH + OH$\rightleftharpoons$ NO + NH_2

  In the case of reaction R8, the NH formed will also further oxidize. This pathway is specially relevant at temperatures exceeding 1100-1200 K and in the reaction zone. Reducing the presence of key radicals in these chemical reactions (O, H, and OH) by injecting water can be a way to suppress this pathway [16, 22].

- **Fenimore or Prompt NOx Pathway:** The prompt NOx pathway consists of reactions between molecular nitrogen and hydrocarbon radicals, CHn. The reactions that guide this mechanism are the following [19, 23]:

  - R10: N_2 + CH$\rightleftharpoons$ NCN + H
  - R11: NCN + O$\rightleftharpoons$ NO + CN
  - R12: CN + O_2 $\rightleftharpoons$ NO + CO
  - R13: NCO + O$\rightleftharpoons$ NO + CO

  This pathway requires the existence of CH radicals to produce any NOx emissions. As such, since this chemical species are lacking in the combustion of pure hydrogen, this mechanism is mostly irrelevant when discussing hydrogen flame emissions [17].

- **Fuel NO Pathway:** This mechanism stems from the dissociation of nitrogen-hydrogen or nitrogen-carbon compounds when nitrogen is chemically bound to the fuel. This causes certain radicals, like CN, NH, HCN, and N to be formed in the reaction zone and be converted into NOx. Nitrogen is mostly bounded in solid and liquid fuels, being missing in the combustion of pure hydrogen. As such, this mechanism is mostly irrelevant when discussing its impact on emissions in hydrogen flames [19, 24].

2.2. Literature Overview on the Effects of Water-Injection on Flames

In this section, an overview of the literature comprising information regarding the effects of water injection on flames is presented. Key developments and trends are analyzed and discussed, along with the identification of possible research gaps and technological limitations.

The primary effects observed relating to the interaction between liquid water and flame include: cooling derived from the heat extraction due to phase change; dilution, originated from an increase in water vapor concentration, from which results a decrease in fuel and oxidizer concentrations; and chemical effects on the flame due to changes in radical production and temperature distribution within the flame due to the presence of steam, thus altering the flame structure. Moreover, since water is a combustion product of a considerable amount of fuels, the injection of water alters the thermo-chemical equilibrium of the system [25].

2.2.1. Chemical and Physical Effects of Water Injection on Combustion

Water-flame interaction has been thoroughly studied throughout the last century with safety applications in mind [26, 27]. In fact, since the ban of halogen based agents to extinguish fires, water mist as been studied as an alternative to them. Countless studies on its main mechanisms of flame extinguishment have been done and it has become well established that the interaction between a pre-mixture of fuel, water mist and air can lead to to quench deflagration and/or detonation, gas explosion mitigation, and diffusion flame extinction. Surprisingly, it has also shown potential to accelerate flame propagation [26, 27]. Furthermore, Nicoli, Haldenwang, and Denet [27], have expanded on these observations and studied the propagation of a nearly stoichiometric premixed flame within a 2D-lattice of water droplets, having found that for smaller droplet inter-distance, a sufficient amount of water injected can quench the combustion. However, for for larger droplet inter-distances and suitable drop size the phenomena aforementioned where flame propagation acceleration occurs is observed.

Furthermore, Lentati and Chelliah [28] using a hybrid Eulerian–Lagrangian formulation for the gas-droplet flow modeled the effects of water injection on laminar counterflow methane–air non-premixed flames for water droplets ranging from 5-50 μm. According to the aforementioned article, when water droplets are introduced into to suppress flames, the air surrounding it will be saturated with water vapor, that can reduce the flame strength and decrease the extinguish strain rate of a counterflow flame. The results there exposed found a maximum decrease of around 25 $\%$ for the extinguish strain rate, partly due to dilution, but also due to the water's high thermal capacity. The results from the article can be found in Figure 2.1.

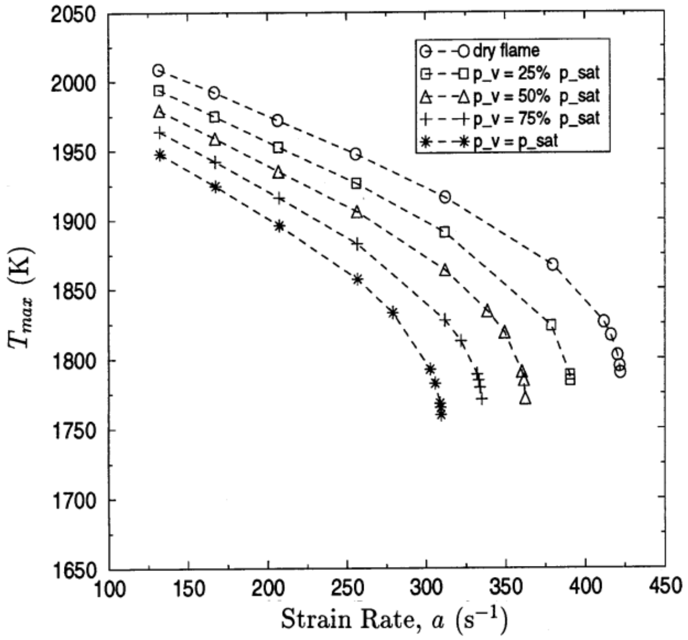

Figure 2.1: Comparison of the maximum flame temperature, T$_{max}$, vs. flow strain rate, a, for different inflow water vapor partial pressures [28]

The flame extinction strain rate has shown to have a nonmonotonic behavior for different monodisperse droplet sizes in premixed counterflow methane flames. When the amount of water injected into the air stream exceeds the saturation pressure, the excess water will condense and take the form of water droplets. These will in turn also affect the extinction strain rate. The results indicate that the strain rate reduces with water vapor mass fraction for all droplet diameters. Furthermore, the extinction strain rate was found to be the smallest for droplet diameters of 15 μm and for diameters above the diminishing trend of extinction strain is reversed [28].

An approach more focused on chemistry is given by Le Cong and Dagaut [29] as it was found a decrease in the mole fraction of O radical and OH and a 50 K increase in the temperature at which hydrogen starts to react with O_2-N_2 mixtures when 10% water is introduced to the combustion process. This observations can be found in Figure 2.2. The reaction pathways that lead to these species formation was also seen to change, as the water vapor presence promotes the chemical reaction $H + O_2 + M \longrightarrow HO_2 + M$, which competes with the main branching reaction $H + O_2 \longrightarrow OH + O$ by turning the reactive H atoms into the less reactive HO_2 radicals. An increase in OH production was also verified for the following chemical reactions:

$$H_2O + O = OH + OH$$
$$H_2O_2\,(^{+}M) = OH + OH\,(^{+}M)$$

And a reduction in OH production through the following chemical reaction:

$$O + H_2 = OH + H$$

Furthermore, it was observed that the presence of water reduces the burning velocities of hydrogen-air mixtures. A limiting factor of the aforementioned study is that the kinetic models used only qualitatively represent the data which can suffer from underestimated flame stretch and/or overestimate the amount of water vapor present.

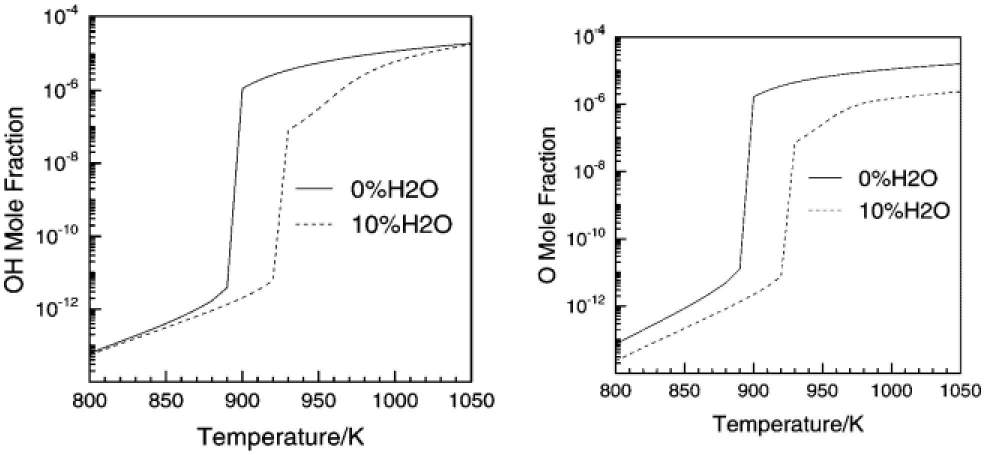

Figure 2.2: Computed O and OH profiles during the oxidation of 1%H_2+ O_2 + N_2 w/o (continuous lines) or with 10% H_2O (dotted lines) at p = 0.5 atm and p = 1 atm [29]

2.2.2. Flashback Prevention in Hydrogen Flames

A flame can be called stable once the kinematics of the flame velocity are balanced together with the velocity at which the incoming mixture is being supplied to the flame [30]. An unstable flame can be blown off or alternatively can propagate upstream, a phenomena called ”flashback”.

There are five different mechanisms/causes that give rise to the flashback phenomena, which are briefly summarized in the following:

- **Flashback in the Boundary Layer:** caused by the low velocities in the boundary layer that promote the upstream flame propagation, since in the walls of a premix tube the flow velocity reaches zero due to the no-slip condition. The heat loss to the wall may cause flame quenching, which can prevent flame flashback. For a highly reactive fuels, like hydrogen, the quenching distance is small and, thus the flame is highly likely to flashback. This is one of the main mechanisms of flame flashback in gas turbines [31, 32].

- **Flashback Due to Combustion Instabilities:** Combustion instabilities may cause upstream flame propagation in both the core flow and in the boundary layer. These instabilities can be generated by the interaction of acoustic modes, fluctuating heat release of the reacting mixture in the primary zone, and flow structure which cause velocity fluctuations. If the pulsations reach a high enough level, velocity deficits will be generated periodically in the flow. Flashback can occur when the frequency of the velocity deficits is low enough [31, 32, 33].
- **Turbulent Flame Propagation in the Core Flow:** The consequence of the turbulent burning velocity exceeding the local flow velocity in the core flow is the upstream flame propagation. In modern days this has stopped being one of the main reasons for flashback in modern gas turbines due to the fact that the core flow velocity in the premixer is in most cases well above the turbulent flame speed [31, 32].
- **Combustion-Induced Vortex Breakdown:** Burners with a center body or fuel lance provide a recirculation zone on the axis even without swirl. However, imposing a swirl on the main flow may lead to an amplification of the backflow of hot gases and a better flame stabilization. Nevertheless, this internal recirculation zone may cause flashback under certain conditions [31, 32].
- **Flashback by Autoignition:** Autoignition is defined as the spontaneous ignition of a combustible mixture due solely to its thermodynamic state, without the need for an external ignition source. Autoignition occurs after a specific period known as the ignition delay time ($_{ig}$), which can range from microseconds to several seconds depending on the mixture's initial thermodynamic conditions [34]. In premixed gas turbine combustion, longer residence times in the premixer help create a more homogeneous fuel–air mixture. However, this conflicts with the need to prevent autoignition. For safe operation, the residence time must be shorter than the autoignition delay time, yet still long enough to ensure proper mixing. This is challenging because real combustors have complex flow patterns and inhomogeneities, making it difficult to define a single ignition delay time. Even a small region of mixture that remains long enough to autoignite can trigger ignition of the entire combustible mixture in the premixer [34].

Water injection into the combustor chamber has shown potential to reduce the flashback probability in hydrogen flames, which as stated before are specifically prone to flashback due to the small quenching distance in the boundary layer.

Pappa et al. [35] performed Large Eddy Simulations (LES) in a typical Turbec T100 (without redesign) combustion chamber with classical methane-air and hydrogen-enriched methane-air flames. The results there provided showed that using hydrogen enriched fuel without water injection lead to flashback due to the high temperatures and reaction rates reached in the combustor. However when water dilution was considered, the reaction rate of the hydrogen reduced and flashback was prevented, which allowed the use of the aforementioned combustor with hydrogen enriched fuel.

Expanding on the water dilution capabilities of preventing flashback, Rouco Pousada et al. [36] has utilized LES simulations with a thickened flame approach and detailed chemistry in a simplified geometry of the hydrogen-fueled reheat combustor to assess the water injection flashback prevention capabilities. An optimized solution was found that reduced NOx in 17 % that also significantly reduced oscillations and flashback.

2.2.3. Effect on Preferential Diffusion and Flame Speed

Concetti et al. [25] analyzed the effects of liquid water addition on turbulent premixed hydrogen/air combustion through Direct Numerical Simulations (DNS) simulations. In this study, the droplets were introduced into the unburned gas domain region at random points while using a homogeneous distribution to avoid clustering and with an initial temperature equal to the unburned gas. The droplet size analyzed corresponded to about $10 - 20\mu m$. It was found that the effects associated with non-unity Lewis number were less significant in the strongly lean case (for an equivalence ration, $\phi = 0.6$) and more prominent in mildly fuel-lean case ($\phi = 0.8$), due to the thicker flames at lower equivalence ratios serving to reduce the extent of flame wrinkling upon water injection. Moreover, the characteristics of water evaporation were shown to be highly dependent on the droplet size, and that smaller sized water droplets show a higher evaporation rate.

Furthermore, water injection was shown to be effective at attenuating the non-unity Lewis number effects of differential diffusion, particularly in smaller sized droplets, due to the aforementioned higher evaporation rate. The effects of water injection were also found to be substantially less pronounced in strongly lean cases, comparatively with mildly-lean and stoichiometric cases, with the latter presenting substantially less wrinkling upon injection of water droplets [25].

2.2.4. Emission Impact of Hydrogen Fuel and Water Injection

NO_x emissions are more efficiently suppressed with shorter residence times, better mixing, and lower reactivity [4, 37]. Humidification and water injection are a method that aims to reduce NO_x emissions of gas turbine combustors by injecting steam and water in order to reduce the hydrogen reactivity and lower the flame temperature [4]. This is possible since water has a high specific heat capacity and latent heat of evaporation absorbs heat from the combustion process, thus decreasing its temperature and, consequently, NO_x emissions. If liquid water is injected instead of water steam than this effect is even more noticeable as additional energy for evaporation is needed. Moreover, steam also changes the NO_x formation since it alters the main reaction pathways [13, 4]. Regarding this Le Cong and Dagaut [29] tested the oxidation of H_2 and CH_4 experimentally in a fused silica jet-stirred reactor from fuel-lean to fuel-rich conditions, over the temperature range 800-1300 K, first without adding H_2O and afterwards adding 10% mol of H_2O. The results obtained indicate a reduction in NO_x emissions when water is injected into the reactor and that this reduction occurs mainly due to dilution, reduction of N_2 concentration, and thermal effects. Increased concentrations of H_2O in premixed flames yield lower flame speeds and lower adiabatic temperature, thus reducing NO_x emissions. In fuel-lean conditions the water was shown to reduce NO_x concentrations by reducing the formation of oxygen radical, the main agent of NO_x production, through the reactions $H + O_2 + M \longrightarrow HO_2 + M$ and $H_2O + O \longrightarrow 2\,OH$.

Sharkey and Zare [38] have recently studied the impact of water injection and hydrogen fuel on performance and emissions in a hydrogen/diesel dual-fuel engine. The approach taken consisted of a modeling study where ten hydrogen energy ratios (0–90$\%$) and nine water injection rates (0–700 mg/-cycle) were tested in a turbocharged Cummins ISBe 220 31 six-cylinder diesel engine. The results yield showed that both water injection and the increase of hydrogen contents on the fuel resulted in a better performance in key metrics such as power, mechanical efficiency, thermal efficiency, indicated mean effective pressure, but worse results regarding brake-specific fuel consumption due to the hydrogen's reduced energy density. Regarding the emissions, the study results indicate that at 90$\%$ hydrogen contents, the CO and CO_2 emissions had been reduced by 94$\%$ and 96$\%$, respectively. An additional decrease in CO was observable when hydrogen rich fuel was paired with water injection. NO_x emissions rose approximately 70% over the range of hydrogen ratios, as expected due to the higher flame temperatures, however water injection was shown to reduce NO and NO_2 emissions up to 16% and 83% respectively, resulting in a net decrease in NO_x emissions in many test cases, with both hydrogen injection and without. To validate the model used an engine experiment was complete [38]. Similarly, Novella et al. [39] found an approximate reduction of 80 $\%$ in NO_x emissions when water injection is applied to hydrogen-powered internal combustion engines geared towards transportation applications.

Banerjee et al. [13] analyzed the effects of steam and water spray on NO_x emissions using a simplified reactor network, which can be used to model a lab-scale combustor. Three different droplet sizes were analyzed in the combustor to study the effect of droplet size. The results showed a reduction of NO_x production when steam and water were injected into the combustor. Part of this results are expressed in Figure 2.3, as it can be observed the total NO_x decreased with steam and water injection (being a more prominent reduction when water was considered) for all equivalence ratios. Bigger droplets were observed to be the most efficient in lowering said emissions . Thermal NO_x was observed to be the dominant mechanism of NO formation and the water and spray addition served to reduce emissions related to this mechanism by lowering flame temperature and the chemical reactions associated with it were seen to become less prominent with steam addition. Prompt NO_x was also affected by steam addition, becoming less prominent. Finally, the study also concluded that injection into the primary combustion zone proved to be the most preferable regarding lowering emissions.

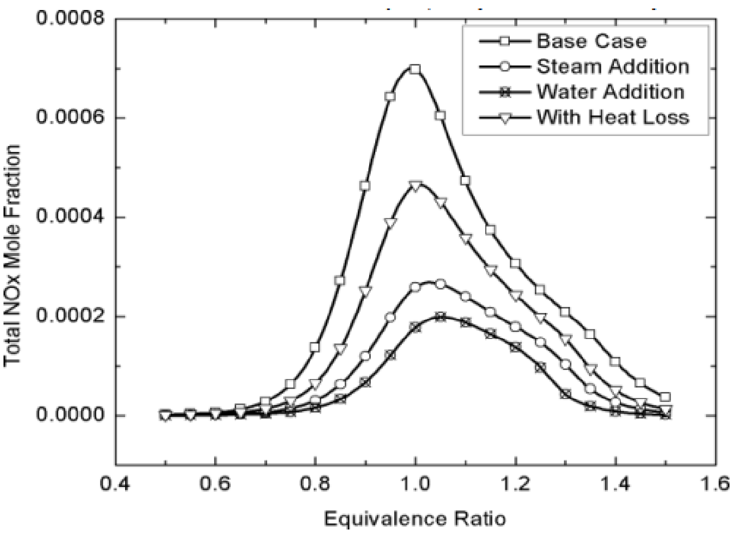

Figure 2.3: Total Mole Fraction of NOx production in the PSR in different equivalence ratios [13].

Xu et al. [40] analyzed the characteristics of combustion and emissions of a hydrogen fueled spark ignition engine in regards to the amount of water injected and its timing. The aforementioned authors concluded that as the amount of water injected grew, the in-cylinder pressure decreased, the indicated thermal efficiency increased, and the flame development and propagation periods prolonged. Furthermore, when the combustion process was subjected to an amount of injected water of 4.5 mg/cycle, the NOx were observed to decrease around 53.7% for an excess air ratio, λ, of 1.15. It was also possible to observe that an early timing for water injection had positive effects on the reduction of NOx emissions, corroborating the conclusions from Banerjee et al. [13].

2.3. Literature Overview on highly strained hydrogen flames

In this section, an overview of the literature comprising information regarding the effects of strain on hydrogen flames is presented. Key developments and trends are analyzed and discussed, along with the identification of possible research gaps and technological limitations.

Flame stretch is the fractional rate of change of a flame surface element A, as described by Eq.(2.1). In a non-uniform flow, any flame front is subject to strain and curvature effects, leading to changes in the flame area [41]. These changes are measured by stretch and a general expression of stretch may be developed for a thin flame sheet, with a subdivision of the strain component and curvature component of it [41]. Said equation is described in Eq.(2.2), where $-\vec{\mathrm{n}}\vec{\mathrm{n}} : \nabla\vec{\mathrm{w}}$ corresponds to the strain component of stretch and the operator $(\vec{\mathrm{n}}\vec{\mathrm{n}} : \nabla)$ represents the gradient operator normal to the flame surface, whose vectorial form is expressed in Eq.(2.3). In this set of equations $\vec{\mathrm{n}}$ corresponds to the unit vector normal to the flame surface pointing towards the fresh gases, $\vec{\mathrm{w}}$ is the velocity of the flame surface [41].

$$K = \frac{1}{A}\frac{dA}{dt} \tag{2.1}$$

30

$$K = -\vec{\mathrm{n}}\vec{\mathrm{n}} : \nabla\vec{\mathrm{w}} + \nabla \cdot \vec{\mathrm{w}} \tag{2.2}$$

$$\vec{\mathrm{n}}\vec{\mathrm{n}} : \nabla\vec{\mathrm{w}} = \left[n_i n_j \frac{dw_i}{dx_j} \right] \tag{2.3}$$

Two-dimensional thermodiffusive instabilities play a major role in hydrogen lean premixed flames. Due to the effective Lewis number below unity found in such mixtures, the propagation of these thermodiffusive instabilities is unstable, and self-amplifying. Under stretch, lean hydrogen flames have also been shown to have an increasing consumption rate as stretch is increased, a property opposite of what is found in hydrocarbon fuels. Stretch was identified to be the main responsible for the increase in consumption speed of a thermodiffusive-unstable flame in comparison with its unstretched equivalent [42].

Chu et al. [43] observed that for laminar flame kernel, differential diffusion causes the stretch factor to exceed unity due to the Markstein effect. In contrast, for a turbulent kernel, it is observed that these instabilities are initiated by turbulence at a radius much smaller than the critical radius [43]. The resulting strong thermodiffusive instabilities significantly increase the stretch factor—by as much as a factor of four compared with a turbulent kernel without such instabilities—thereby substantially promoting early flame kernel growth under engine conditions [43]. Strong thermodiffusive instabilities produce large fluctuations in the local fuel–air equivalence ratio, leading to superadiabatic temperature rises of up to 500 K. Differential diffusion strongly affects the relationship between the local flame displacement speed and curvature through contributions from normal flame propagation and the Soret effect [43]. Moreover, thermodiffusive instabilities alter the surface-area growth process, significantly increasing both the production and destruction of flame surface area during propagation [43].

Hydrogen flames have been shown to present an increasing consumption speed as the strain rate is increased due to its negative Markstein length. Moreover, hydrogen flames have been proven to withstand very high strain rates, and their maximum heat release rates have been shown to increase with strain [42]. Additionally, flame tangential strain has proven to be effective at delaying lean blow-off in bluff body stabilized laminar flames [42, 44]. Increases on flame temperature and decreases in $\mathrm{NO_x}$ emissions have also been observed in highly strained hydrogen flames. [14, 42].

There are two strained flamelet configurations commonly used: the first configuration is represented by a reactants-to-reactants counterflow configuration, where two flames are stabilized symmetrically with respect to the flow stagnation plane, and the second one which is represented by a reactants-to-products, where a single flame stabilizes on the reactants side of the domain. [14]. These configurations are both represented in Figure 2.4. The first configuration has been thoroughly studied in literature [15, 45, 46, 47]. The effects of hydrogen enrichment, strain on lean blowoff, extinction strain, mass burning rate, and $\mathrm{NO_x}$ emissions are considered. Xie and Wang [15] identified the NNH pathway as the main mechanism for $\mathrm{NO_x}$ formation in rich pure-hydrogen strained flames. Similar results were obtained by Ning, Fan, and Yao [46], but for a fuel mixture of molecular hydrogen and carbon monoxide flames. The latter study revealed that at smaller strains the NO formations occurs more easily in the syngas containing less $\mathrm{H_2}$ and more CO at small strain rates, at large strain rates this tendency inverts and it occurs more easily in the syngas with higher hydrogen percentage. Xie and Wang [15] found that in counter-flow premixed hydrogen-air flames, at low stretch rates, the temperature is high and thermal mechanism contribute more towardsNO production and vice-versa for the high stretch rate situation. The same study also revealed that overall NO production decreases with stretch rate due to decreasing temperature and reaction volume at higher stretch.

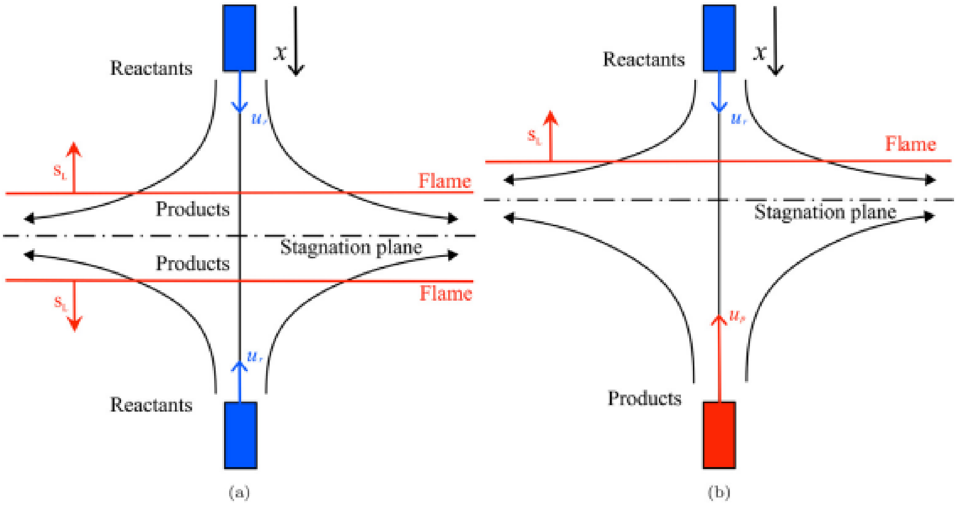

Figure 2.4: Sketch of the reactants-to-reactants (a) and reactants to-products (b) counter-flow premixed strained flame configurations [14].

The second configuration (reactants to-products) is characterized for having a single flame located on the reactants domain. This allows for very high strain flames to have an elevated degree of combustion completion, since the fuel and the radicals have enough space to burn entirely [14]. Moreover, the extinction strain rate has been shown to be possible to calculate. However, the presence of complete combustion products on one of the boundaries may precondition the problem [14]. Porcarelli, Kruljević, and Langella [14] used this configuration to computationally predict NOx emissions in highly strained counterflow laminar flames, arguing that this configuration is more suited for investigation exactly because of the high completion combustion rate at very high strains it allows. The results found suggest that NOx emissions can be suppressed with highly strained flames, despite increasing reactivity of the hydrogen. Moreover, these results suggest that the reduction occurs mainly due to a decrease in the thermal NOx pathway due to the local redistribution of radicals, even though the temperature across the flame does not decrease with strain. Finally, the authors also concluded that the NOx suppression identified can be achieved for both lean and ultra-lean hydrogen flames.

Figure 2.5 shows the NO mass fraction across the longitudinal length in a one-dimensional hydrogen-air flamelet obtained by Porcarelli, Kruljević, and Langella [14].

Fathi et al. [48] performed DNS simulations of hydrogen/air flame for increasing levels of applied strain on a turbulent reactants-to-products counterflow configuration with the goal of investigating how tangential strain affects the general flame behaviour and NOx emissions. It was observed that NOx emissions are reduced within the simulation domain due to the redistribution of flame radicals, in particular OH radicals [48]. It was also observed that the NOx reduction in highly strained hydrogen flames comes mostly from bulk effects as little correlation was found between local fluctuations flame-tangential strain rate and NOx production [48].

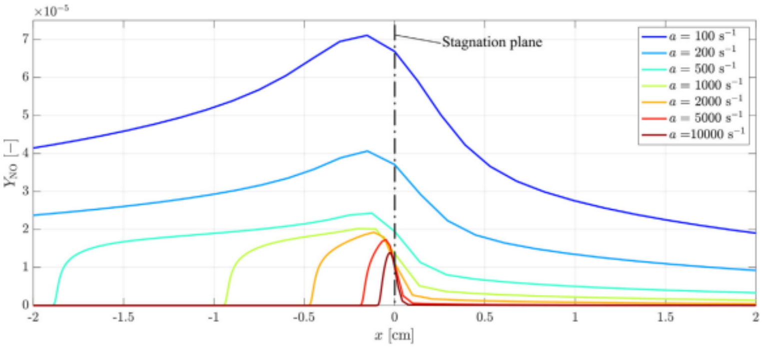

Figure 2.5: NO mass fraction (Y_{NO}) across the longitudinal coordinate x in a one-dimensional hydrogen-air flamelet at equivalence ratio ϕ = 0.7, for different applied strain rates a [14].

3

Research Relevance & Questions

This chapter's objective is to highlight the topic's background and research relevance. The research gaps identified are exposed and briefly discussed and to conclude this chapter a thesis proposal and the research questions that guide it are formulated.

3.1. Research Relevance

Hydrogen as a fuel source has the potential to substitute fossil fuels in both the energy generating market, but also in the vehicle fuel industry as it can be produced with renewable energy sources, and is carbon free since the majority of green house gases cannot form due to the lack of carbon atoms in the fuel [10, 11, 38, 4]. For hydrogen powered vehicles current technologies offer two possibilities: the hydrogen fuel cell and direct hydrogen combustion. Hydrogen fuel cell requires high-purity hydrogen to prevent the cell from being poisoned, while internal combustion can work with lower purity hydrogen [49]. However, storage of hydrogen and challenges regarding its combustion make this transition challenging. Furthermore, due to its higher flame temperature, the NO_x emissions associated with direct hydrogen combustion tend to be higher then traditional fossil fuels.

In recent years, water injection has risen as a solution to mitigate NO_x emissions since the addition of water decreases the flame's temperature due to its high specific heat capacity and causes changes in the reaction pathways that lead to the formation of NO_x [13]. Moreover, liquid water injection reduces the concentration of fuel and oxidizer due to dilution (increase in water vapor concentration) and can alter the thermo-chemical equilibrium since it is a combustion product of certain fuels [25]. Currently, Pratt $\&$ Whitney are researching a concept turbine engine running on liquid hydrogen fuel, using water vapor recovery and steam injection technology [50]. This conceptual design named Hydrogen Steam Injected, Inter-Cooled Turbine Engine (HySIITE) aims to make use of water vapor and steam injection technology to reduce NOx emissions up to 99.3% and increase energy efficiency by up to 35%. Nevertheless, further investigation is required and new combustor designs and emission analysis are necessary since burning hydrogen or hydrogen containing fuels in gas turbines significantly affects the thermodynamic process and component performance due to its high reactivity, high burning velocity, and shorter ignition time delay which can increase the risk of flashback and auto-ignition [4].

3.2. Thesis Proposal & Research Questions

The literature review revealed some research gaps and constraints regarding the effects of water-injection on the emissions on highly strained hydrogen flames. Firstly, it was identified that the application of water injection for emission control in hydrogen premixed hydrogen flames has been explored only in a limited set of flame configurations and applications. Moreover, the combined effects of high-strain conditions and water injection on emissions have not yet been examined in the available literature. Consequently, a clear research gap can be identified in this respect.

Existing literature has shown that both highly strained flames and water injection can serve as methods to reduce emissions.

The following research question was formulated as MSc Thesis Project, based on the work done and the research gaps identified throughout the literature review:

How does water injection, under prescribed high-strain-rate conditions, affect NO_x emissions and flame structure in hydrogen premixed flames?”

Some sub-questions can also be formulated in order to guide and support the main research question. Such as:

1. How does the injection velocity of water affect NO_x emissions and flame structure of highly strained hydrogen flames?
2. How does the droplet diameter of the injected water affect NO_x emissions and flame structure of highly strained hydrogen flames?
3. How does a flame strain increment affect NO_x emissions and flame structure of highly strained hydrogen flames with water injection?

To guarantee a good organization and facilitate the MSc thesis development, the described problem will be divided into multiple work packages that can be consulted underneath:

1. **Literature Review:** development of a first draft literature review to identify research gaps and insights on relevant developments on technologies and studies relevant to the topic. Continuous work shall be done to the literature review as the thesis project develops.
2. **Familiarize with OpenFoam:** Time will be allocated to increase the degree of familiarization with OpenFoam, the open-source CFD software to be used for this project. The objective is to obtain a elevated degree of computational knowledge, which will be required for the project completion.
3. **Develop CFD Model**: develop the CFD model required to obtain the computational simulations, based on the insights obtained from the literature review and the OpenFoam expertise acquired.
4. **Validation and Analysis**: Validate the results of the model with the data from literature and conduct a sensitivity analysis of the impact on emissions of water-injection on highly strained hydrogen flows.
5. **Writing the Thesis Report**: Writing the thesis report. This process should start throughout the previously defined work packages.
6. **Thesis Defense and Presentation**

4

Methodology

In this chapter a description of the overall methodology employed for the purposes of studying the effects of water injection in highly strained hydrogen flames is presented. First, an overview of the mathematical model and the mathematical approach taken is provided, which includes the reduced chemical mechanism used, the droplet modeling approach, and the variable definition used to quantify emission reductions. Secondly, a brief description of the 1D simulations gathered to define the boundary conditions for the flame and Bilger mixture fractions for the dry case and the wet baseline case is provided. Finally, information regarding the method used for the 2D simulation's domain and the resulting sensitivity analysis is shown. The chapter concludes with a subsection that aims at providing information regarding the simulation matrix, i.e, showing the parameters varied for each case studied analyzed.

4.1. Mathematical Model

In this section of the report the information concerning the overall mathematical model utilized during the thesis project is exposed. Firstly, the chemical mechanisms for hydrogen/air reactions and NOx formation are described, with the chemical reactions guiding them being summarized. Then the information and approximations regarding the model for the droplets in the spray are exposed. Finally, the variables defined to account for the emission reduction of relevant species and Bilger mixture fraction calculations are described.

4.1.1. Chemical Mechanisms

In order to study the changes in emission and flame temperature and chemistry caused by injecting water, planar premixed hydrogen/air flames are analyzed using two dimensional detailed chemistry simulations. For this purpose, a reduced chemical mechanism is used for fuel oxydation recently proposed by Sánchez and Williams [51] consisting of 18 reactions involving 8 different chemical species. The chemical reactions are expressed in Table 4.1. This reduced chemistry model is coupled with the NOx mechanism used in [52], which contains 7 nitrogen based species and 25 reactions, summarized in Table 4.2.

Table 4.1: Rate coefficients in Arrhenius form $k = BT^n exp(T_a/T)$ for the skeletal mechanism with rate parameters in mol, s, cm^3, kJ, and K, based on [51]

	Reaction	B	n	T_a
1f	$H + O_2 \rightarrow OH + O$	$3.52 \cdot 10^{16}$	-0.7	8590
1b	$OH + O \rightarrow H + O_2$	$1.05 \cdot 10^{14}$	-0.313	132
2f	$H_2 + O \rightarrow OH + H$	$5.06 \cdot 10^{4}$	2.67	3165
2b	$OH + H \rightarrow H_2 + O$	$3.03 \cdot 10^{4}$	2.63	2433
3f	$H_2 + OH \rightarrow H_2O + H$	$1.17 \cdot 10^{9}$	1.3	1825
3b	$H_2O + H \rightarrow H_2 + OH$	$1.28 \cdot 10^{10}$	1.18	9412
4	$H + O_2 \rightarrow HO_2$ k_0	$5.75 \cdot 10^{19}$	-1.4	0.0
	k_∞	$4.65 \cdot 10^{12}$	-0.44	0.0
5	$HO_2 + H \rightarrow OH + OH$	$7.08 \cdot 10^{13}$	0.0	148
6f	$HO_2 + H \rightarrow H_2 + O_2$	$1.66 \cdot 10^{13}$	0.0	414
6b	$H_2 + O_2 \rightarrow HO_2 + H$	$2.69 \cdot 10^{12}$	0.36	27888
7	$HO_2 + OH \rightarrow H_2O + O_2$	$2.89 \cdot 10^{13}$	0.0	-250
		$4.50 \cdot 10^{14}$	0.0	5500
8f	$H + OH \rightarrow H_2O$	$4.22 \cdot 10^{22}$	-2.0	0.0
8b	$H_2O \rightarrow H + OH$	$1.03 \cdot 10^{23}$	-1.75	59675
9f	$H + H + M \rightarrow H_2 + M$	$1.30 \cdot 10^{18}$	-1.0	0.0
9b	$H_2 + M \rightarrow H + H + M$	$3.04 \cdot 10^{17}$	-0.65	52092
10	$H_2O_2 \rightarrow OH + OH$ k_0	$7.60 \cdot 10^{30}$	-4.20	25703
	k_∞	$2.63 \cdot 10^{19}$	-1.27	25703
11	$HO_2 + H_2 \rightarrow H_2O_2 + H$	$1.03 \cdot 10^{14}$	0.0	5556
		$1.94 \cdot 10^{11}$	0.0	-709
12	$HO_2 + H_2 \rightarrow H_2O_2 + H$	$7.80 \cdot 10^{10}$	0.61	12045

Table 4.2: Rate coefficients in Arrhenius form $k = BT^n exp(T_a/T)$ for the skeletal mechanism with rate parameters in kmol, s, m^3, kJ, and K for the NO_x mechanism, based on [52]

	Reaction	B	n	T_a
1	$H + NH_2 \rightarrow H_2 + NH$	$4.00 \cdot 10^{10}$	0.0	1837
2	$NH_2 + O \rightarrow NH + OH$	$6.80 \cdot 10^{9}$	0.0	0
3	$NH_2 + OH \rightarrow H_2O + NH$	$4.00 \cdot 10^{3}$	2.0	503
4	$N + NH_2 \rightarrow H + H + N_2$	$7.00 \cdot 10^{10}$	0.0	0
5	$NH_2 + NO \rightarrow NNH + OH$	$4.30 \cdot 10^{7}$	0.294	-436
6	$H + NH \rightarrow H_2 + N$	$3.00 \cdot 10^{10}$	0.0	0
7	$NH + O \rightarrow H + NO$	$9.20 \cdot 10^{10}$	0.0	0
8	$NH + OH \rightarrow H_2O + N$	$5.00 \cdot 10^{8}$	0.5	1006
9	$OH + NH \rightarrow H_2 + NO$	$1.00 \cdot 10^{10}$	0.0	0
10	$NH + O_2 \rightarrow NO + OH$	$9.90 \cdot 10^{7}$	0.0	770
11	$NH + NO \rightarrow N_2 + OH$	$2.20 \cdot 10^{10}$	-0.23	0
12	$N + OH \rightarrow NO + H$	$3.80 \cdot 10^{10}$	0.0	0
13	$N + O_2 \rightarrow NO + O$	$6.40 \cdot 10^{6}$	1.0	3160
14	$N + NO \rightarrow N_2 + O$	$9.40 \cdot 10^{9}$	0.14	0
15	$NNH \rightarrow N_2 + H$	$1.00 \cdot 10^{9}$	0.0	0
16	$H + NNH \rightarrow H_2 + N_2$	$1.00 \cdot 10^{11}$	0.0	0
17	$N_2O \rightarrow N_2 + O$ k_0	$6.00 \cdot 10^{11}$	0.0	28905
	k_∞	$9.90 \cdot 10^{10}$	0.0	29135
18	$NNH + O \rightarrow H + N_2O$	$1.90 \cdot 10^{11}$	-0.274	-11
19	$NNH + O \rightarrow NO + NH$	$5.20 \cdot 10^{8}$	0.388	-206
20	$NNH + OH \rightarrow H_2O + N_2$	$5.00 \cdot 10^{10}$	0.0	0
21	$NNH + O_2 \rightarrow HO_2 + N_2$	$5.60 \cdot 10^{11}$	-0.385	-7
22	$N_2O + H \rightarrow N_2 + OH$	$6.40 \cdot 10^{4}$	1.835	6790
23	$NH + NO \rightarrow N_2O + H$	$2.70 \cdot 10^{12}$	-0.78	10
24	$N_2O + O \rightarrow NO + NO$	$9.20 \cdot 10^{10}$	0.0	13928
25	$N_2O + O \rightarrow N_2 + O_2$	$9.20 \cdot 10^{10}$	0.61	13928

4.1.2. Droplet Modeling

The injection of liquid droplets on a premixed hydrogen flame can be studied by means numerical simulations employing an Eulerian Lagrangian approach. In this approach the gas phase which has higher volume fraction, is considered the carrier phase and the governing equations are the classic Navier-Stokes equations solved in an Eulerian framework, whilst the liquid phase, in this case liquid droplets, are treated as point particles and are tracked in a Lagrangian referenced frame. This Eulerian-Lagrangian approach is more deeply analyzed in Yang and Kee [53],Veynante and Poinsot [41], and Modak et al. [54], here only an overview of the governing equations of the taken Eulerian-Lagrangian framework will be shown:

Gas-phase conservation equations

The equations presented here describe the conservation equations for reacting flows

ρ, u, c_p, and T are the gas-phase variables for mass density, velocity, heat capacity, and temperature, respectively. Y_k corresponds to the species mass fractions, h_k corresponds to the species enthalpies, $\dot{\omega}_k$ respects the molar production rates by chemical reaction, W_k the species molecular weights, and V_k the species diffusion velocities [41].

Mass Continuity:

$$\frac{\partial \rho}{\partial t} + \frac{\partial (\rho u_i)}{\partial x_i} = 0 \tag{4.1}$$

Species Conservation (for $k = 1$ to $N - 1$, or N if total mass is not used):

$$\frac{\partial(\rho Y_k)}{\partial t} + \frac{\partial(\rho(u_i + V_{k,i})Y_k)}{\partial x_i} = \dot{\omega}_k \tag{4.2}$$

By definition,

$$\sum_{k=1}^{N} Y_k V_{k,i} = 0 \tag{4.3}$$

$$\sum_{k=1}^{N} \dot{\omega}_k = 0 \tag{4.4}$$

With Hirschfelder and Curtiss approximation:

$$\frac{\partial(\rho Y_k)}{\partial t} + \frac{\partial(\rho(u_i + V_i^c)Y_k)}{\partial x_i} = \frac{\partial(\rho D_k \frac{W_k}{W}\frac{\partial X_k}{\partial x_i})}{\partial x_i} + \dot{\omega}_k \tag{4.5}$$

with,

$$\sum_{k=1}^{N} D_k \frac{W_k}{W}\frac{\partial X_k}{\partial x_i} = V_i^c \tag{4.6}$$

Momentum:

$$\frac{\partial \rho u_j}{\partial t} + \frac{\partial \rho u_j u_i}{\partial x_i} = -\frac{\partial p}{\partial x_j} + \frac{\partial \tau_{ij}}{\partial x_i} + \rho \sum_{k=1}^{N} f_{k,j} Y_k \tag{4.7}$$

Energy:

Sum of sensible and formation enthalpies (assuming negligible viscous heating, null body forces, and, since low Mach number flow is assumed, the pressure effect is also negligible):

$$\frac{\partial \rho h_s}{\partial t} + \frac{\partial(\rho u_i h_s)}{\partial x_i} = \dot{\omega}_T - \frac{\partial J_{h_s}}{\partial x_i} + \dot{S}_h, \;\; with \;\; \dot{\omega}_T = -\sum_{k=1}^{N} \Delta h_{f,k}^{o} \dot{\omega}_k \tag{4.8}$$

where h_s is the mixture's sensible enthalpy and J_{h_s} is the mixture sensible enthalpy diffusion fluxes.

Droplet equations

The droplet dynamics can be described in the Lagrangian reference frame by the following set of equations. Since a low-Stokes number can be assumed due to the droplet's reduced dimensions, it can be assumed that the droplet and its surrounding packet travel together through the gas-phase domain, as represented by the solution on a Eulerian mesh. During evaporation, the droplet interacts locally with the gas in its encasing packet. The subscript "d" represents the variables related to the properties and parameters of the droplet [53, 55].

Droplet's Equation of Motion:

$$m_d \frac{du_d}{dt} = \frac{\pi d_d^3}{6}(\rho_d - \rho)g + \frac{C_d \rho \pi d_d^2}{8}|u_d - u|(u_d - u) + F_{lift} \tag{4.9}$$

Droplet's Energy Conservation Equation:

$$m_d C_{p,d} \frac{dT_d}{dt} = h \pi d_d^2 (T - T_d) + \frac{dm_d}{dt} h_{fg} \tag{4.10}$$

Energy Transport from Lagrangian to Eulerian phase:

$$Q_d = \frac{\sum_{i=1}^{N}(\pi d_{d,i}^2 h (T - T_{d,i}))}{V_{cell}} \tag{4.11}$$

Droplet Reynolds Number:

$$Re_d = \frac{d_d \rho |u_D - u|}{\mu} \tag{4.12}$$

Schmidt Number:

$$Sc = \frac{\mu}{\rho D} \tag{4.13}$$

Droplet Drag Coefficient:

$$C_D = max\{\frac{24}{Re_D}(1 + 0.15 Re_d^{0.687}); 0.44\} \tag{4.14}$$

Ranz-Marshall Correlation for Nusselt Number:

$$Nu = \frac{hd_d}{k_t} = 2.0 + 0.6 Re_d^{1/2} Pr^{1/3}, \quad Pr = \frac{\mu}{\rho\alpha} \tag{4.15}$$

Ranz-Marshall Correlation for Sherwood Number:

$$Sh = \frac{k_{mt} d_d}{D} = 2.0 + 0.6 Re_d^{1/2} Sc^{1/3} \tag{4.16}$$

Droplet Diameter:

$$d_d = \left(\frac{6m_d}{\pi \rho_d}\right)^{\frac{1}{3}} \tag{4.17}$$

Droplet Evaporation Term:

$$\frac{dm_d}{dt} = \pi d^2 m_{wl} k_{mt} \left(\frac{p_{sat}}{RT_d} - X\frac{p}{RT}\right) \tag{4.18}$$

Furthermore, since the shape of the particle size distribution curve is best described by a continuous function [56], a Rosin-Rammler distribution for particle size was used to estimate this distribution coupled with Lefebvre's characteristic diameter.

The equation for the Rosin-Rammler distribution is at least partially based on empirical data and is given by [56]:

$$Y = 1 - exp\left(\frac{-x}{x_0}\right)^n \tag{4.19}$$

where Y is the cumulative fraction of material by weight less than size x; x_0 is the characteristic particle size, in this case Lefebvre's characteristic diameter; and n is the uniformity constant.

Lefebvre's characteristic diameter is computed based on Sauter Mean Diameter (SMD) and given by the following expression:

$$x_0 = \mathrm{SMD} \cdot \Gamma\left[1 - \frac{1}{\mathrm{n}}\right] \tag{4.20}$$

where SMD is the Sauter Mean Diameter, n the uniformity constant, and Γ the gamma function.

For the baseline case, the values defined for n was arbitrary chosen to be 2.5, while SMD was placed at $10\ \mu m$, based on the literature studies by [28] and [25], whose observations show that at diameters around this order of magnitude a favorable evaporation rate is observed.

4.1.3. Variables Definition

This section introduces and defines the variables employed in this work to evaluate the impact of water injection on the flame structure and NO emissions. In order to study the emissions of NOx formation related species, i.e, NNH,N_2O, and NO, the integral of such species in the domain is defined by Eq.(4.21), Eq.(4.22), and Eq.(4.23), respectively.

$$I_{\mathrm{NNH}} = \int\int Y_{\mathrm{NNH}}\ dxdy \tag{4.21}$$

Similarly for N_2O and NO we have:

$$I_{\mathrm{N_2O}} = \int\int Y_{\mathrm{N_2O}}\ dxdy \tag{4.22}$$

$$I_{\mathrm{NO}} = \int\int Y_{\mathrm{NO}}\ dxdy \tag{4.23}$$

From these integrals, figures of gain for each aforementioned chemical species are defined by equations 4.24, 4.25, and 4.26. These are used in order to quantify the reduction in species emissions observed when water is injected.

$$f_I^{\mathrm{NNH}} = \frac{I_{\mathrm{NNH}}}{I_{\mathrm{NNH}}^{dry}} \tag{4.24}$$

$$f_I^{\mathrm{N_2O}} = \frac{I_{\mathrm{N_2O}}}{I_{\mathrm{N_2O}}^{dry}} \tag{4.25}$$

$$f_I^{\mathrm{NO}} = \frac{I_{\mathrm{NO}}}{I_{\mathrm{NO}}^{dry}} \tag{4.26}$$

Moreover, the bulk strain rate a is computed as:

$$a = -\left(\frac{du_x}{dx}\right)_p \tag{4.27}$$

In order to isolate the impact of the chemical and physical effects of water injection on the flame, a correction for dilution is applied for radical and NOx emission analysis. The method employed for this correction is partly based on the work by Douglas et al. [57]: the water is removed by multiplying the species to be analyzed by a drying factor, A, defined in Eq.(4.28) at each cell of the domain. Since water is also a product of the reaction, once comparing the radical concentrations and NOx emission data treated this way, they will be compared against a corrected dry case where water is also removed through the use of the same method.

$$A = \frac{1}{1 - Y_{\mathrm{H_2O}}} \tag{4.28}$$

where $Y_{\mathrm{H_2O}}$ is the cell value for the water mass fraction.

For the analysis relating stretch and water injection to preferential diffusion, the Bilger mixture fraction of each simulation will be compared with the Bilger mixture fractions obtained in 1D simulations and the 2D dry case. The mathematical expression defining the Bilger mixture fractions is:

$$Z_{\mathrm{Bilger}} = \frac{\beta - \beta_{ox}}{\beta_{fuel} - \beta_{ox}} \tag{4.29}$$

where β is defined as:

$$\beta = \sum \gamma_k Z_k \tag{4.30}$$

where γ_k is the weighting factor of each element and Z_k is the elemental mass fraction of every chemical element.

To conclude this section the definition used to compute the hydrogen progress variable is presented. In premixed flames, a progress variable is the primary control variable used to define chemical reaction progress [58]. For this analysis two progress variables will be considered: one based on the molecular hydrogen mass fraction, whose concentration peaks at the fuel zone and reaches a minimum on the products side, and the other progress variable used is based on the mass fraction variation of molecular oxygen. Although the latter was intended to be used to guarantee that a thorough analysis is done, since H_2 is more sensitive than O_2 to changes in chemical pathways and thermophysical changes in the flame caused by water injection, it was verified that the lack of monotonicity of the oxygen based progress variable made it hard to analyze. As such, the hydrogen progress variable was chosen to be used in this analysis and its definition is presented in Eq.(4.31) based on the work by Hasslberger et al. [59].

$$c(\mathrm{H_2}) = \frac{\mathrm{Y_{H_2,0}} - \mathrm{Y_{H_2}}}{\mathrm{Y_{H_2,0}} - \mathrm{Y_{H_2,b}}} \tag{4.31}$$

where subscript 0 corresponds to the reactants flow composition and subscript b corresponds to the chemical equilibrium.

4.2. 1D Simulations

To define the boundary conditions for the 2D simulations, a preliminary iteration with Cantera [60] software was performed. This was done through simulating a freely propagating flame in 1D for an equivalence ratio of $\phi = 0.7$, which means that for this freely propagating 1D flame the ratio between the actual fuel-to-oxidizer ratio and the fuel-to-oxidizer stoichiometric ratio is 0.7. Once the solution of freely propagating flame is obtained, it is used to initialize a 1D premixed reactants to-products counterflow flame by imposing at the product stream the product of complete combustion. These 1D simulations are then compared to the higher fidelity 2D results for the dry case and the for the cases with water injection in order to derive conclusions.

For the case study where a strain rate of $a = 8000$ s^{-1} is used, an additional preliminary iteration with Cantera was done in order to find a new set of reactants and products injection velocity that would guarantee the desired strain rate where the flame position within the domain remains similar to the original set of cases.

4.3. 2D Simulations

In this section of the report, the information regarding the simulation domain and mesh sensitivity analysis completed are exposed. The Navier-Stokes equations with low-Mach number approximation for these 2D simulations are discretized using the finite volume method presented in the OpenFoam [61] software and utilizing the reactingParcelFoam solver to solve them [61]. A Gaussian linear second-order accurate numerical interpolation scheme was used for all gradients and divergences in conjunction with implicit Euler time integration.

Regarding the boundary conditions, the one the reactants side of the counter-flow setup the mass fractions of H_2, O_2, N_2, and H_2O are 0.02, 0.228, 0.752, and 0, respectively, with this species being injected at a temperature of 300 K. On the product side, the respective mass fractions of H_2, O_2, N_2, and H_2O are 0, 0.068, 0.752, and 0.18 with a temperature of 2027 K and a pressure of 101325 Pa is imposed. A zero-gradient condition for the pressure is prescribed. The injection velocities of both the products and reactants can be consulted in Table 4.4 for each case.

The mesh sensitivity analysis was conducted for both the dry case and one of the wet cases to guarantee the scientific validity of the results obtained. Moreover, a comparison between the 1D simulations described in the previous section and the dry case is done for their Bilger mixture fraction to prove that the 2D model used can properly estimate the effects fo stretching and water injection on preferential diffusion. Finally, this section ends with the presentation of the simulation matrix, containing information regarding each simulation case and showing the parameter variations between them.

4.3.1. Computational Domain and Mesh Sensitivity Analysis

Figure 4.1 presents the fluid domain for the computational setup. It has a rectangular shape, with a width $L_y = 1.36$ cm and a length of $L_x = 1.81$ cm. When water injection is active, it is injected from the mid point of the left side limit of the domain wall in a conical spray with an inner angle $\theta_{in} = 0$ and an outer cone angle of $\theta_{out} = 45°$. The pressure in the domain remains constant and equal to 101325 Pa throughout the entire simulation process.

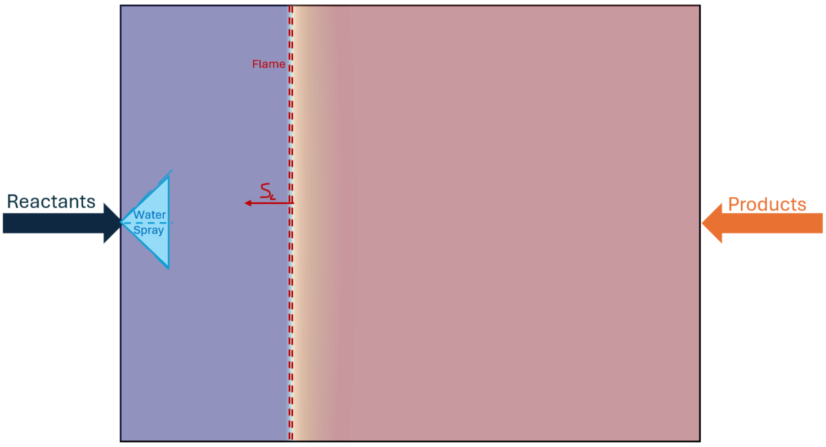

Figure 4.1: Sketch of the Fluid Computational Domain. The two red dashed lines are indicative of the flame region.

Table 4.3: Mesh information of the Mesh Sensitivity Analysis Cases.

Number of Cells	Cell Length [cm]	Number of Cells Within the Flame Thickness
160k	$3.92 \cdot 10^{-}3$	8
520k	$2.18 \cdot 10^{-}3$	15
1200k	$1.43 \cdot 10^{-}3$	22

In order to guaranty the validity and quality of the attained results, a mesh convergence study was initially carried out in the dry case, where three different meshes on different refinement levels are compared against each other. The first refinement level consists of a mesh with approximately 160 thousand cells, with cell dimensions being, approximately, $l_x = 3.92 \cdot 10^{-}3$ cm and $l_y = 3.92 \cdot 10^{-}3$ cm, which is approximately 8 times smaller than the thermal flame thickness which stands at $\delta_{th} = 3.2 \cdot 10^{-2}$ cm; the second refinement level consists of a mesh with approximately 520 thousand cells, with cell dimensions being, approximately, $l_x = 2.18 \cdot 10^{-}3$ cm and $l_y = 2.18 \cdot 10^{-}3$ cm, which is approximately 15 times smaller than the thermal flame thickness; and the third is made with a mesh of approximately 1200 thousand cells, with cell dimensions being, approximately, $l_x = 1.43 \cdot 10^{-}3$ cm and $l_y = 1.43 \cdot 10^{-}3$ cm, which is approximately 22 times smaller than the thermal flame thickness. This information is summarized in Table 4.3. To compare these refinement levels the temperature and mass fractions of intermediate species across the centerline are plotted. The results are expressed in Figure 4.2a, Figure 4.3a, Figure 4.4a, Figure 4.5a, and Figure 4.6a, and as it is possible to observe very little difference between the results from the different meshes. As such, it was decided that the coarser mesh was already refined enough to provide accurate results whilst reducing the computational load necessary and a second refinement analysis was done in a case with water injection.

The second mesh sensitivity analysis was done in a case with water injected at 20% of the reactants velocity at a time step of 1 ms after water is injected into the domain. This injection velocity corresponds to the highest injection velocity analyzed and was chosen to be used for the sensitivity analysis since it presents the lowest computational cost as the higher injection velocity translates into having less total parcels in the simulation domain at the same time, reducing computational load. Similarly to the dry case sensitivity analysis, the temperature and mass fractions of intermediate species across the centerline are plotted and the results are shown in Figure 4.2b, Figure 4.3b, Figure 4.4b, Figure 4.5b, and Figure 4.6b.

In this second sensitivity analysis, although the location of local maxima and minima are mismatched, their magnitude is correctly retrieved and the overall trend remains consistent

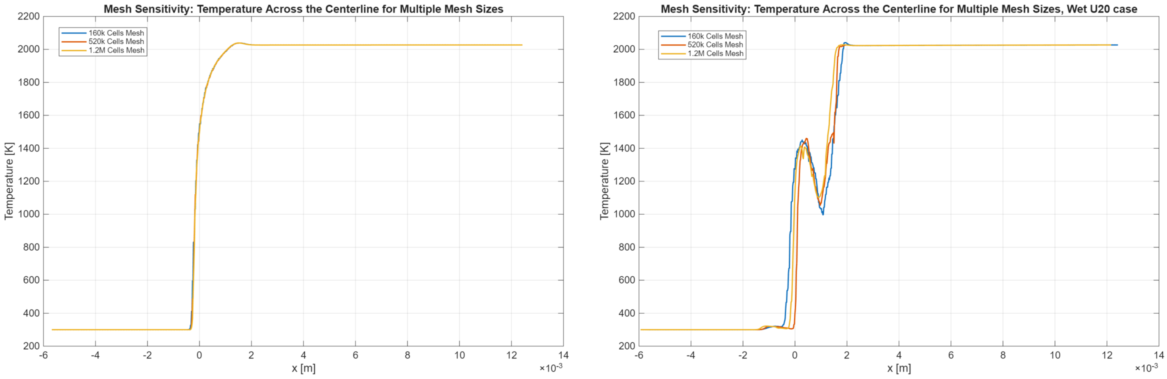

(a) Mesh Sensitivity: Temperature Across the Centerline for Multiple Mesh Sizes, Dry Case.

(b) Mesh Sensitivity: Temperature Across the Centerline for Multiple Mesh Sizes, Wet Case U20.

Figure 4.2: Mesh Sensitivity: Temperature Across the Centerline for Multiple Mesh Sizes.

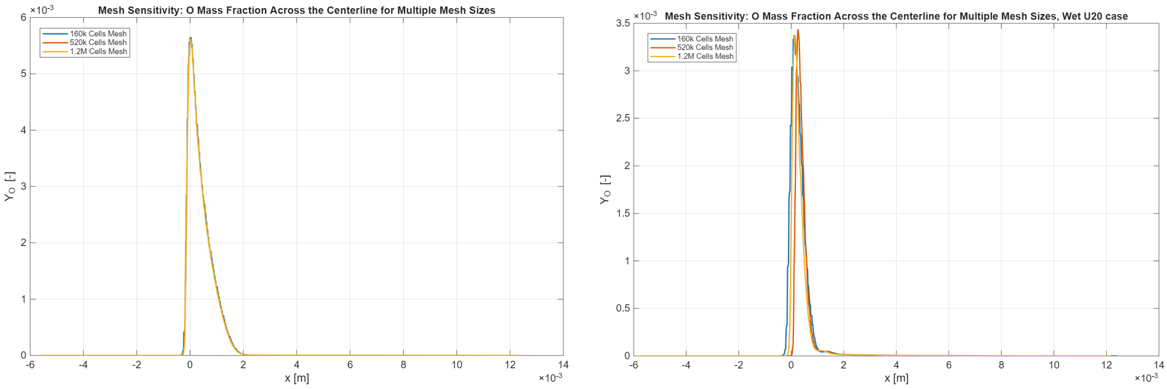

(a) Mesh Sensitivity: Y_O Across the Centerline for Multiple Mesh Sizes, Dry Case.

(b) Mesh Sensitivity: Y_O Across the Centerline for Multiple Mesh Sizes, Wet Case U20.

Figure 4.3: Mesh Sensitivity: Y_O Across the Centerline for Multiple Mesh Sizes.

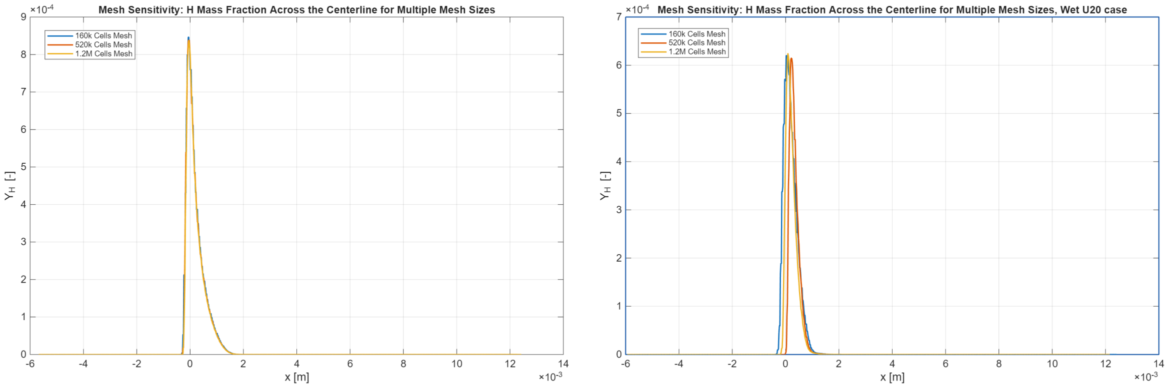

(a) Mesh Sensitivity: Y_H Across the Centerline for Multiple Mesh Sizes, Dry Case.

(b) Mesh Sensitivity: Y_H Across the Centerline for Multiple Mesh Sizes, Wet Case U20.

Figure 4.4: Mesh Sensitivity: Y_H Across the Centerline for Multiple Mesh Sizes.

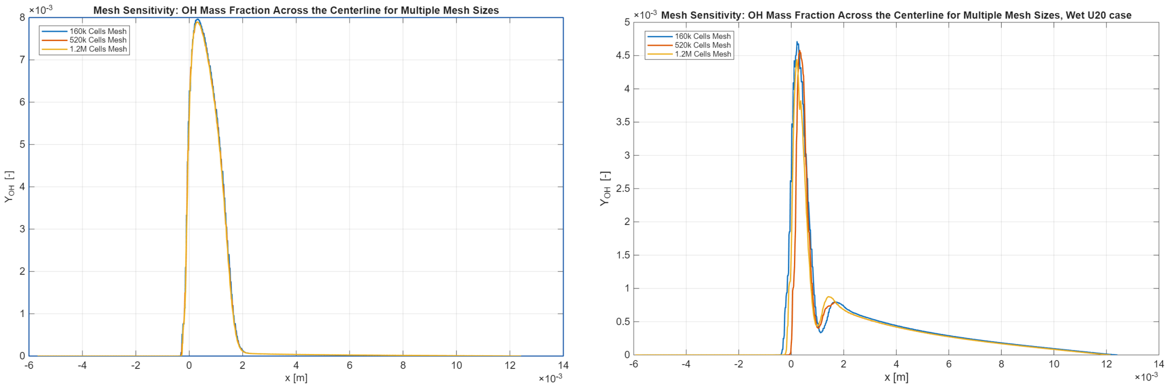

(a) Mesh Sensitivity: $\mathrm{Y_{OH}}$ Across the Centerline for Multiple Mesh Sizes, Dry Case.

(b) Mesh Sensitivity: $\mathrm{Y_{OH}}$ Across the Centerline for Multiple Mesh Sizes, Wet Case U20.

Figure 4.5: Mesh Sensitivity: $\mathrm{Y_{OH}}$ Across the Centerline for Multiple Mesh Sizes.

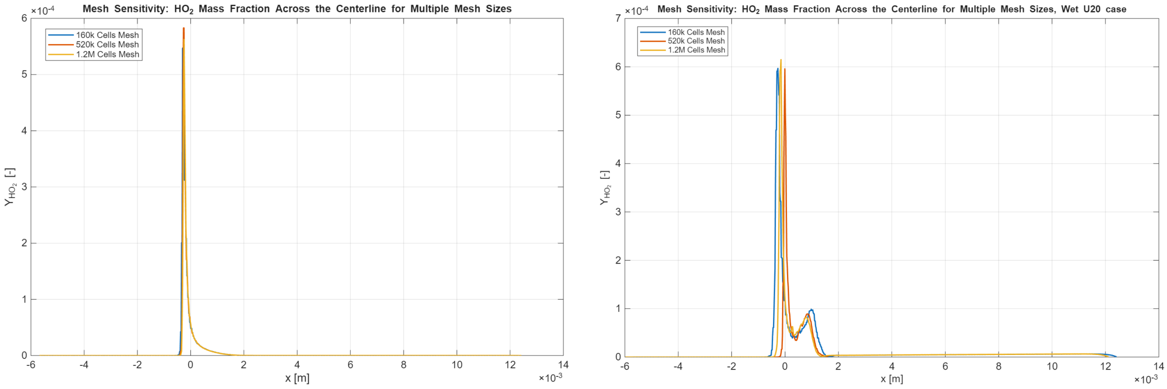

(a) Mesh Sensitivity: $\mathrm{Y_{HO_2}}$ Across the Centerline for Multiple Mesh Sizes, Dry Case.

(b) Mesh Sensitivity: $\mathrm{Y_{HO_2}}$ Across the Centerline for Multiple Mesh Sizes, Wet Case U20.

Figure 4.6: Mesh Sensitivity: $\mathrm{Y_{HO_2}}$ Across the Centerline for Multiple Mesh Sizes.

Figure 4.7 shows the Bilger mixture fraction in function of the hydrogen progress variable for the 2D dry case, the 1D stretched flame, and the 1D unstretched flame. In a case where Le is artificially imposed to be equal to 1, preferential and differential diffusion are non-existent, and thus the curve takes the shape of a uniform straight line for all values of the considered progress variable [42]. However, due to the different values for the species diffusivity, in particular due to the hydrogen's low Lewis number, a local imbalance between fuel and oxidizer is created and a local dip in mixture fraction is observed [42]. A local enrichment at higher hydrogen progess variable values, $c(\mathrm{H}_2)$ (defined in Eq.(4.31)) values and a reduced dip are observed in stretched flames, due to the effects of strain on the flame as noted by [62], [63], and [42].

As it is observable, the 2D setup created closely follows the 1D framework defined in the previous section, but the characteristic peak caused by the stretch is slightly less accentuated in the 2D domain. Moreover, it is observable that the characteristic dip associated with preferential diffusion is less noticeable in the 2D setup than it is in the 1D cases. The errors between the 1D dry stretch flame and the 2D domain are approximately a 0.9% difference at the peak and a 5.3% error at the dip. These observable changes are likely due to the lower fidelity associated with the 1D results when comparing them with the 2D solutions

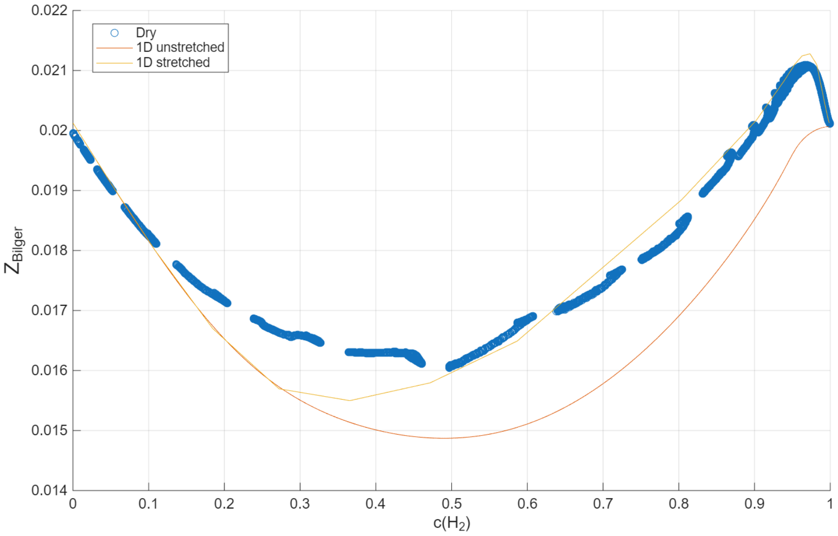

Figure 4.7: Bilger Mass Fraction Across the Domain in Function of the Hydrogen Progress Variable, Dry Case.

4.3.2. Simulation Matrix

Table 4.4 and Table 4.5 provide information regarding the operating conditions and key parameters for the simulation setups considered with water injection. As it can be observed, the baseline case with water injection consists of a hydrogen flame with an equivalence ratio of 0.7, where the reactants are injected at 14.59 m/s and the products injection velocity is 56.9 m/s, placing its bulk strain rate (defined in Eq.(4.27)) at around 4000 s^{-1}. The key spray parameters varied are the injection velocity of the water and the droplet standard mean diameter, SMD and for the baseline case considered they take the values of 0.73 m/s (corresponding to 5% of the reactants injection velocity) and 10 μm, respectively. The conditions for cases U10 and U20 are equal to the baseline with the exception of the injection velocity, where it is varied to 1.46 m/s and 2.92 m/s, respectively, which correspond to an injection velocity of 10% and 20% of the reactants injection velocity. The baseline SMD was chosen based on the literature study by Concetti et al. [25] that showed that for droplet diameters of 10-20 μm a good evaporation rate is observed. The injection velocity of the baseline case was selected by simulating the selected baseline with U10 and U20, and the case with the lowest reduction in emissions observed was selected.

Cases SMD15 and SMD25 occur under the same reactants and products conditions of the baseline case, with the exception of SMD, which is increased to 11.5 μm and 12.5 μm, respectively. Finally, case S2 refers to a computational setup where the strain rate is increased to 8000 s^{-1}, and as such the reactants and products injection velocity are altered compared to the baseline case. Regarding the spray parameters in setup S2, they are the same as the baseline case, with the exception of the injection speed since the reactants injection velocity increases in order to guarantee that this case also presents an injection velocity of 5% the value of the injection velocity also needs to be increased.

Table 4.4: Varying Operating Conditions and Key Parameters for the Simulation Setups.

Quantity	Symbol	Units	Baseline	U10	U20	SMD15	SMD25	S2
Reactants Injection Velocity	U_{reac}	m/s	14.59					30.00
Products Injection Velocity	U_{prod}	m/s	56.90					114.80
Droplet SMD	SMD	μm	10.00			11.50	12.50	10.00
Spray Injection Velocity	U_{spray}	m/s	0.73	1.46	2.92	0.73		1.50

Table 4.5: Operating Conditions and Key Parameters for the Simulation Setups that are Constant in All Cases.

Quantity	**Symbol**	**Units**	**Value**
Equivalence Ratio	ϕ	[-]	0.7
Reactants Temperature	T_{reac}	K	300
Operating Pressure	p	Pa	101325
Reactants Density	ρ_{reac}	kg/m^3	0.9242
Products Temperature	T_{prod}	K	2027
Products Density	ρ_{prod}	kg/m^3	0.1553
Conical Spray Inner Angle	θ_{in}	$\circ$	0
Conical Spray Outer Angle	θ_{out}	$\circ$	45

5

Results

In this chapter, the results obtained for all the simulations done will be presented and discussed. Firstly, the results for the baseline simulation with water injection will be exposed and analyzed. The flame structure is analyzed in terms of radical mass fractions, temperature profiles, and hydrogen consumption rate. In addition, the effect of the injection of water in the flame is further evaluated in terms of its impact on NO_x emissions. Once the baseline results are presented and discussed, a parametric analysis will be performed to assess the effect of water injection parameters. In particular, the injection velocity, SMD, and strain rate will be systematically varied, and the results will be compared with the baseline case in order to evaluate their impact.

Throughout the chapter, observations are made regarding the obtained results and their comparison with the reviewed literature.

5.1. Base Simulation: Injection Velocity Equal to 5% of Reactants Injection Velocity and SMD = $1.0 \cdot 10^{-5}$ meters

In this section the results corresponding to the baseline case for all simulations are presented and commented. The baseline case was selected as described in chapter 4 and has a water injection velocity, U, equal to 5% of the reactants injection velocity and a droplet mean diameter, SMD, of $1.0 \cdot 10^{-5}$ meters.

5.1.1. Radical Concentrations on the Flame Region

Figures 5.1, 5.2, 5.3, and 5.4 show plots of the distribution of O, H, OH, and HO_2 radical mass fraction across the flame zone. As it can be observed, injecting water into the domain provided some key changes in the flame radical composition. Figure 5.1 provides information regarding the mean mass fraction of oxygen radicals in the flame region during 4 ms after the water is injected into the simulation domain. As it can be observed in Figure 5.1, immediately after the water is injected, there is a small drop in this species' mass fraction that remains relatively constant until around 0.6 ms.

After the water droplets reach the flame, a sudden drop in mass fraction of O, H, and OH is observed, with the mass fractions of these radicals starting to stabilize into a new value at around 2.5 ms. During this time period (0.6 to 2.5 ms) the mass fractions of O, H, and OH drop approximately 93%, 95%, and 71%, respectively.

The opposite behavior is observed in Figure 5.4. For the HO_2 radical, a sudden increase in the mass fraction of this radical is observable, peaking at $t = 1.4$ ms and then dropping to a value slightly higher than the one observed in the dry case.

These results are in line with what was observed in the literature study, specifically in Le Cong and Dagaut [29] as they showed that water presence promotes the chemical reaction $H + O_2 + M \longrightarrow HO_2 + M$, which competes with the main branching reaction $H + O_2 \longrightarrow OH + O$ by turning the reactive H atoms into the less reactive HO_2 radicals. Regarding the other radicals, the observed decrease is also consistent with the trend shown in the literature [29]. There is a significant drop in O and H radicals due to the changes in reaction pathways discussed in chapter 2, and a smaller, but still a substantial decrease in OH mass fractions. In fact, injecting water into a flame leads to reduction to radical mass fractions through dilution and by promoting certain chemical reactions like the aforementioned $H + O_2 + M \longrightarrow HO_2 + M$, but also promotes the formation of this radical due to the increased humidity, which promotes the chemical reactions $H_2O + O = OH + OH$ and $H_2O_2\,(^{+}M) = OH + OH\,(^{+}M)$ [29], slightly which makes the decrease in this radical's mass fraction less pronounced than H and O radicals.

In the aforementioned figures, the mean species mass fractions corrected for dilution are also plotted, using a drying factor defined in Eq.(4.28). The approach to the method used for making meaningful comparisons without considering dilution is also described in subsection 4.1.3. As it is observable, once a correction is applied the reduction in the mass fraction present observable is less pronounced, as expected, but it also demonstrates the the bulk of the reduction observed in the data without dilution correction for the species O, H, and OH is due to the chemical and physical effects of water discussed in the last paragraph. Moreover, applying this correction also permits observing the increasing production of HO_2 more clearly, coinciding with the literature study and data seen in [29], as removing the water dilution effect permits isolating the chemical effects aforementioned that predict an increase in HO_2 mass fraction.

Overall for the baseline configuration it was observed a sharp reduction in the presence of O,H, and OH radicals caused by dilutions and by changes in the chemical pathways caused by the injection of water, whilst a an increase in HO_2 radicals is seen due to the promotion of this species formation. These results are indicative of a reduction in hydrogen reactivity, as such it is expected that the rate of production of hydrogen will decrease in absolute value. Moreover, the reduction in O, H, and OH radicals should translate into a sharp reduction in emissions, as these radicals are necessary species in the NOx formation mechanisms, which are described in section 2.1.

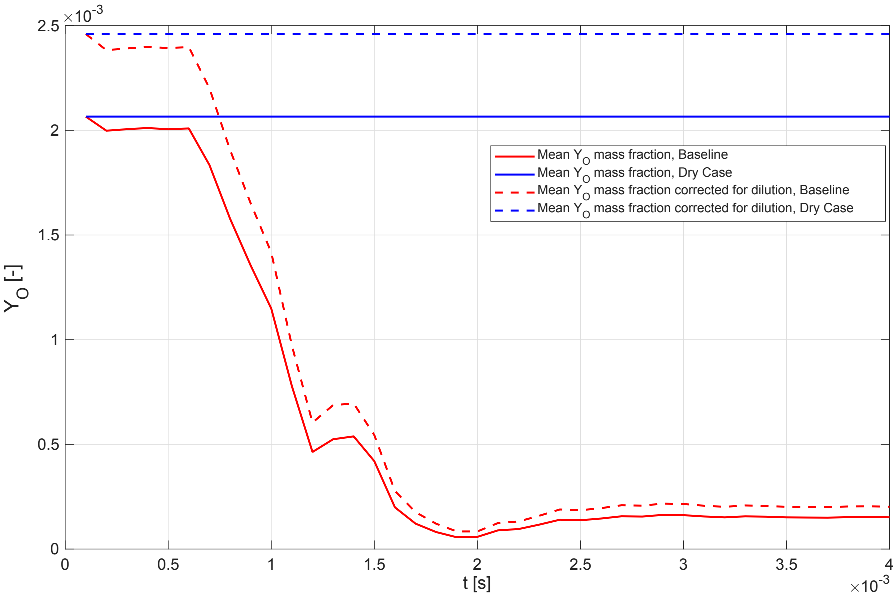

Figure 5.1: Mean Y_O as a function of time. Baseline case (see Table 4.4 and Table 4.5).

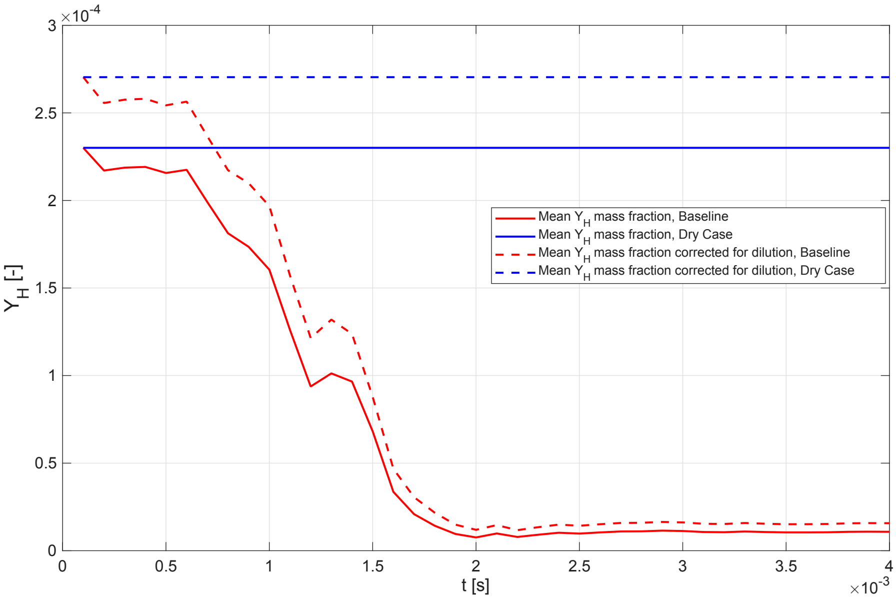

Figure 5.2: Mean Y_{H} as a function of time. Baseline case (see Table 4.4 and Table 4.5).

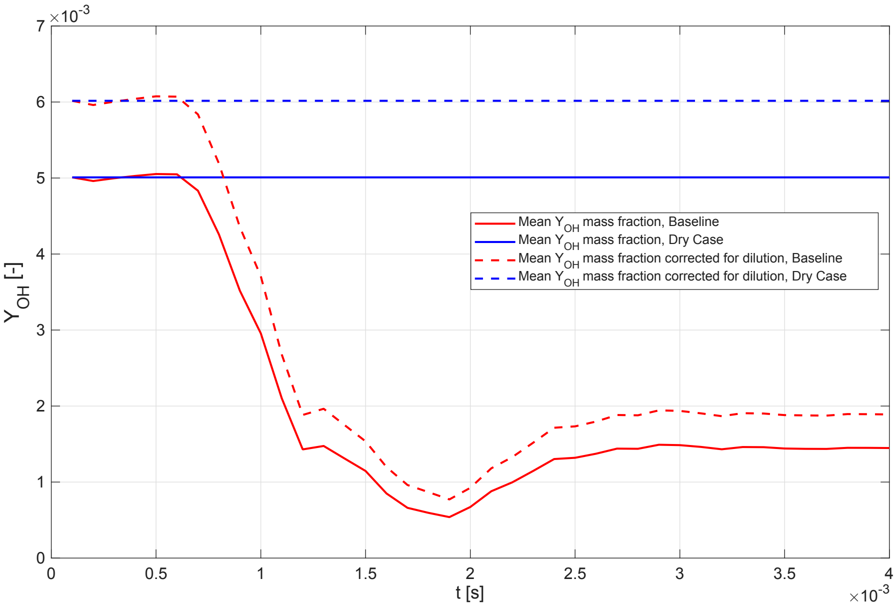

Figure 5.3: Mean Y_{OH} as a function of time. Baseline case (see Table 4.4 and Table 4.5).

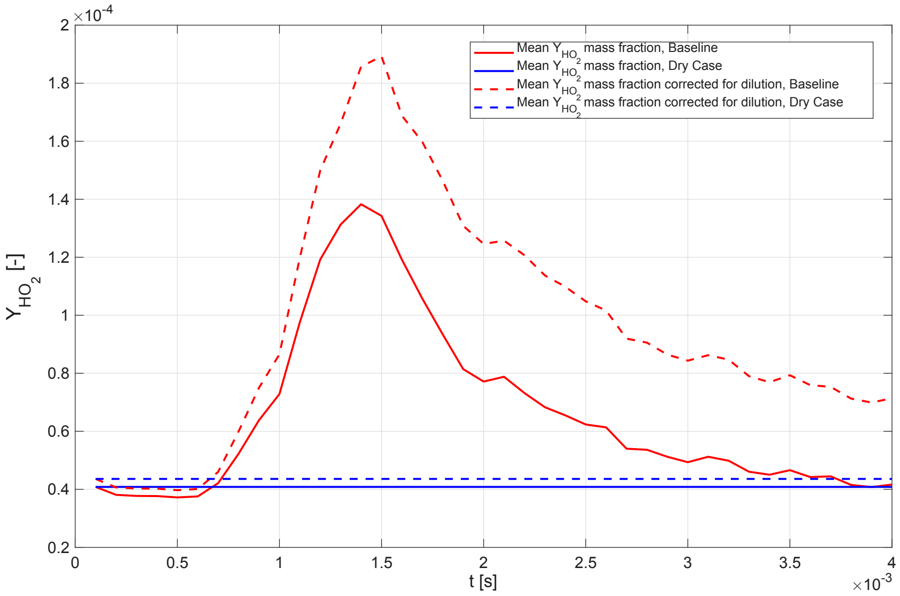

Figure 5.4: Mean $\mathrm{Y}_{\mathrm{HO}_2}$ as a function of time. Baseline case (see Table 4.4 and Table 4.5).

5.1.2. Temperature and Hydrogen Rate of Production

Figure 5.5 and Figure 5.6 show the behavior of the mean hydrogen rate of production and the mean temperature around the flame region, i.e, the zones where a stronger hydrogen consumption was observed.

Figure 5.5 shows that the hydrogen rate of production starts - before the water injection - at a strongly negative value and remains clearly negative throughout the early part of the time range, meaning that hydrogen is being consumed rather than produced, as expected. Throughout the initial time steps of the simulated time period, the consumption fluctuates but stays at relatively large negative values, although less negative than the original dry case, signifying an immediate reduction of consumption even before the water reaches the flame. The observed fluctuations in the hydrogen consumption rate are likely caused by the upstream effect of injecting water into the domain. The water upstream evaporates causing the local reactivity to fluctuate, whilst also altering the shape of the flame and wrinkling it, provoking changes in the hydrogen consumption rates. At t = 1 ms, a rapid rise in the curve is observable: the hydrogen consumption weakens, and the values move quickly towards a much smaller negative number (meaning that the rate of consumption of hydrogen was vastly decreased). After this sharp transition, the curve levels off and approaches a nearly steady state, indicating that the hydrogen consumption becomes much smaller and stabilizes. Overall, a very sharp decrease in hydrogen consumption is observed, with its value going from 14.5 kg/(m^{3}s) to approximately 0.5 kg/(m^{3}s) after 2.2 ms and stabilizing around this value for the remainder simulation time, with the majority of this decrease occurring once the water comes into contact with the flame.

Additionally Figure 5.6 shows the effect of water injection on the mean temperature profile in the region oh highest reactivity. As it can be seen that initially the temperature stays nearly constant at a high temperature, showing a slight increase possibly due to perturbations due to the injected water upstream, but also because of the observable radical concentration changes expressed in figures 5.1, 5.2, 5.3, and 5.4, then begins a pronounced drop. This decrease is sharp and continues until the temperature hits a low of about 1130 K at around 1.7 ms. After this minimum point, the baseline curve starts to rise again, recovering gradually, and then settles into a slower upward-and-downward variation at a lower temperature level compared to the beginning.

Comparing both graphs, the timing of the strongest temperature decrease in the baseline case aligns with the period where the hydrogen consumption starts to decrease more sharply. Likewise, the moment when the hydrogen production rate curve moves closer to its asymptotic behavior, the temperature begins to approach its quasi steady-state value. Thus, both graphs show a clear connection in their timing: the major shift in the hydrogen curve occurs at the same point where the temperature changes most significantly.

This results are within what would be expected based on the literature review in chapter 2, specifically the research in [28, 29, 13]. A strong temperature drop in the baseline case is verified due to evaporation effects, and water dilution caused by water injection.

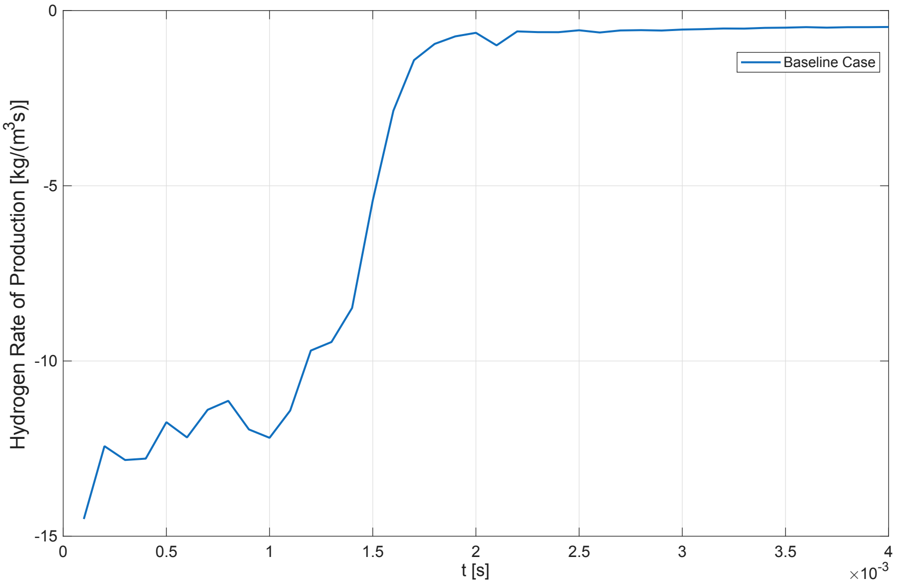

Figure 5.5: Mean hydrogen rate of production on the flame region

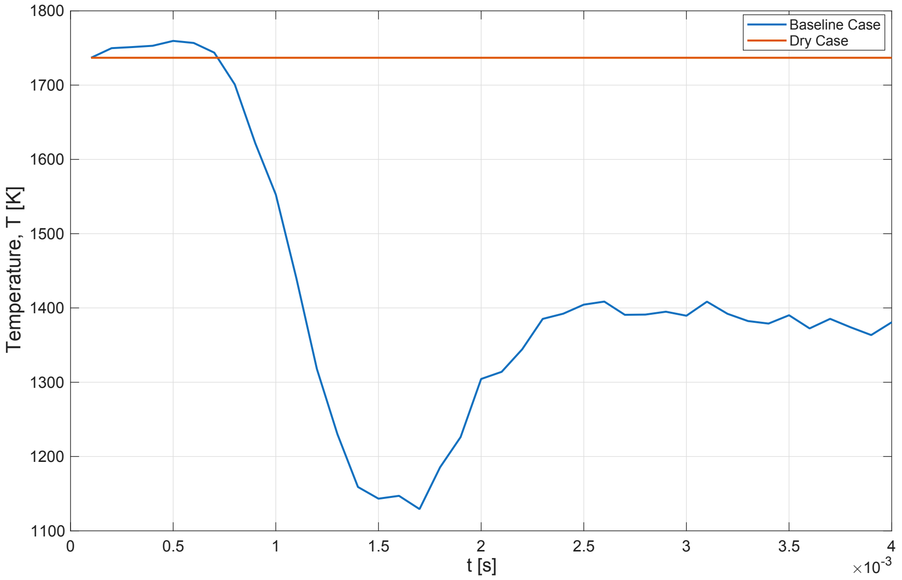

Figure 5.6: Mean Temperature on the flame region.

Figure 5.7 plots the temperature value in each cell in the domain as a function of the progress variable defined in Eq.(4.31). The progress variable is computed for both dry and baseline water injection cases. Analyzing this figure also provides some key insights into the effects of water injection on the flame at t = 4 ms. In this figure, each dot represents the average value of the temperature in each cell in the domain. First, it is observable that the reaction zone moves towards the product region as evidenced in Figure 5.7, where the peak temperature and the sudden increase in flame temperature occur at higher molecular hydrogen progress variable. This is likely due to changes in reaction pathways and chemical effects caused by it such as the increase in HO_2 verified previously and the reduction in hydrogen reactivity observable in Figure 5.5.

Secondly, it is observable that even though the peak temperature occurs in the baseline wet case, the average temperature across the vast majority of domain cells is significantly lower in it as well, which is to be expected based on the results exposed in Figure 5.6 and the literature study presented in chapter 2.

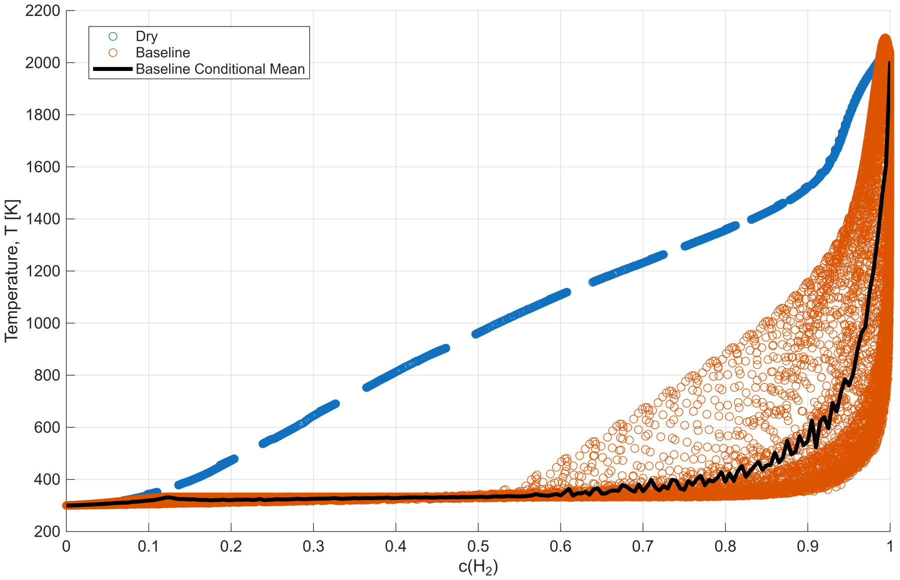

Figure 5.7: Temperature distribution in function of the hydrogen progress variable at t = 4ms.

5.1.3. **NNH** Emission Results

For the baseline case, severe changes in NNH, one of the main chemical species responsible for the formation of NOx as discussed in section 2.1, mass fractions were observed throughout the simulated time frame. These results are expressed in Figure 5.8, where the value of f_I^{NNH} (defined in Eq.(4.24)) is plotted in relation to time. As it can be observed, immediately at the first evaluated time frame an increase of around 20$\%$ of this species emissions is observed. However, as soon as the droplets enter in contact with the flame front, at around $t = 0.6$ ms, a drastic decrease of this species mass fraction is found until $t = 1.3$ ms, where once again the concentrations of NNH increase for a short time frame until they are once again further reduced. This observed increase before resuming decreasing is likely due to the increased flame movements and wrinkling of the flame front that is found along these time steps, as the flames tries to reach a kinematically stable state. At around $t = 2.5$ ms, the value of f_I^{NNH} reaches an asymptotic behavior, signaling the start of a quasi-steady state for the simulation. After this point, the reduction in NNH mass fraction is around 97.4% of the original case without water injection. This goes in accordance to what is observed in the literature study, the water injection reduces the key radicals presence (as observed in subsection 5.1.1) which are specially important in the NNH pathway for NOx formation, as discussed in section 2.1. Indeed, these results are in line with what would be expected from the results presented in subsection 5.1.1: the NNH formation in the NNH mechanism start with the recombination of molecular nitrogen with H, the heavy suppression of H radicals presented in Figure 5.2 leads to the formation of NNH being heavily reduced. Moreover, the reduction in NNH observed combined with the reduction in O radicals observed in Figure 5.1 should heavily reduce the formation of NO from the NNH mechanism as it is described in section 2.1.

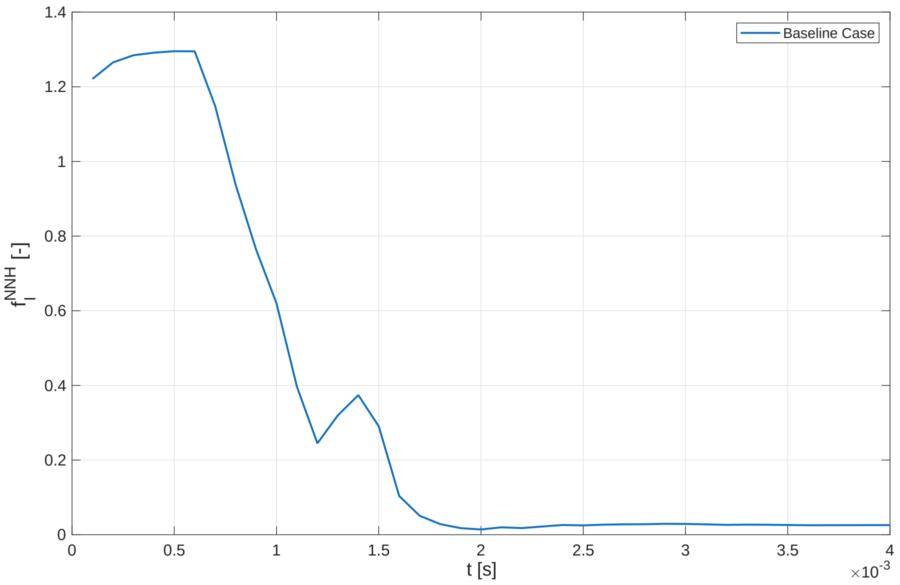

Figure 5.8: f_I^{NNH} Time history with Water Injection, Baseline case (see Table 4.4 and Table 4.5).

Figure 5.9 displays the average NNH mass fractions for every cell of the domain against the molecular hydrogen progress variable (defined in Eq.(4.31)) at $t = 4$ ms. As it can be seen, when compared to the dry case there is a very significant reduction of this species mass fraction for every value of both progress variables. Furthermore, it is observable that the peaks for this concentrations occur at later values of $c(\mathrm{H}_2)$, which translates into the peaks of this reactions occurring closer to the products' region. This is significant since NNH formation occurs mainly on the flame's reaction zone, corroborating this idea, initially described in subsection 5.1.2.

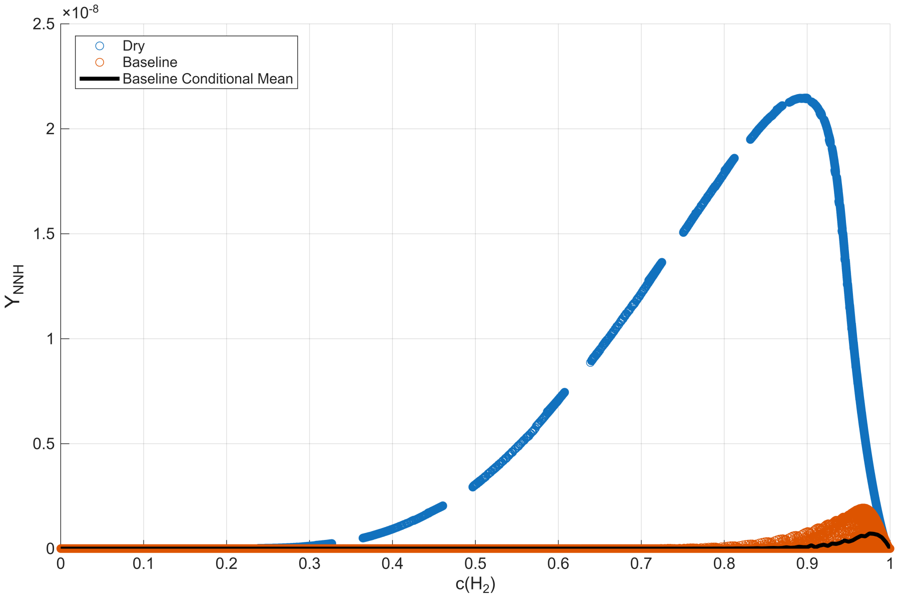

(a) NNH mass fraction distribution in function of the hydrogen progress variable at t = 4ms.

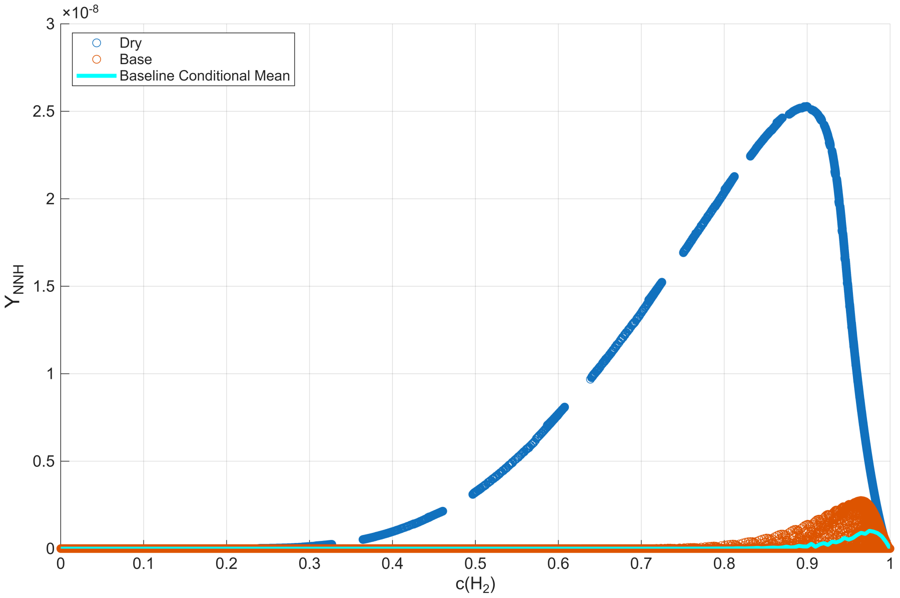

(b) NNH mass fraction distribution in function of the hydrogen progress variable at t = 4ms, corrected for dilution.

Figure 5.9: NNH mass fraction distribution at t = 4ms.

5.1.4. N_2O Emission Results

A similar pattern to the one observed in Figure 5.8 is found in Figure 5.10; however the reduction of this species mass fraction is much less accentuated. Once a quasi-steady state is reached the reduction in N_2O mass fraction observed is around 62.2%. This also is expected, since water injection not only reduces this species mass fraction through dilution, but also reduces the amount of O radicals present by 93%, which are key elements for the formation of this molecule - as described in reaction R4 present in section 2.1. On the other hand, the lower temperatures also promote the N_2O mechanism relevance, by making it chemical reactions present in it more prepense and slightly counter balancing the reduction caused by depriving this chemical mechanism of O radicals.

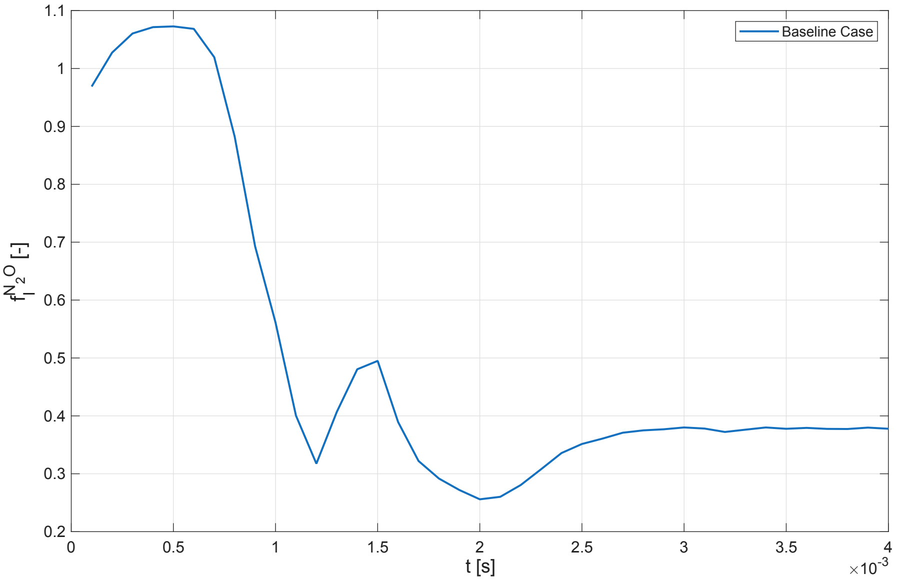

Figure 5.10: $f_I^{\mathrm{N_2O}}$ Time history with Water Injection, Baseline case (see Table 4.4 and Table 4.5).

Further observations regarding how this chemical species mass fraction changes due to the injected water can be inferred from Figure 5.11. Firstly, from the dry case scatter points it is observable that there are two peaks of N_2O mass fraction: one at around $c(H_2)= 0.92$ and one even closer to the product zone at around $c(H_2)= 0.98$. The first peak occurs slightly after the flame location, based on the Figure 5.7 and Figure 5.9, and as it is possible to observe this peak is heavily reduced in the baseline case with water injection, as the figure 5.11a only presents one mass fraction peak. This is likely due to the sharp reduction in O radicals necessary to form N_2O caused by injecting water into the system. As such, the majority of N_2O is located even closer to the product's region than in the dry case. Moreover, it is also possible to observe a reduction in peak $Y_{\mathrm{N_2O}}$, likely caused by the factors aforementioned. Finally, it is observable that at lower values of $c(H_2)$, before the flame front, there is an increase of the mass fraction of N_2O. This is likely due to water evaporation causing changes in the chemical pathways and the decrease in temperature verified across the domain promoting N_2O formation at these locations.

Accounting for the dilution, as observed in Figure 5.11b, it is observable that the increase in $Y_{\mathrm{N_2O}}$ observed at lower equivalence ratios is even larger than expected as the dilution effect masks it slightly. Overall, it is observable that whilst an increase in $Y_{\mathrm{N_2O}}$ is observable at lower values of $c(H_2)$, the verified decrease in $Y_{\mathrm{N_2O}}$ at higher progress variable values due to the changes in radical concentrations discussed in subsection 5.1.1 is enough to cause a sharp reduction of about 62.2% for the value of $f_I^{\mathrm{N_2O}}$ (including dilution).

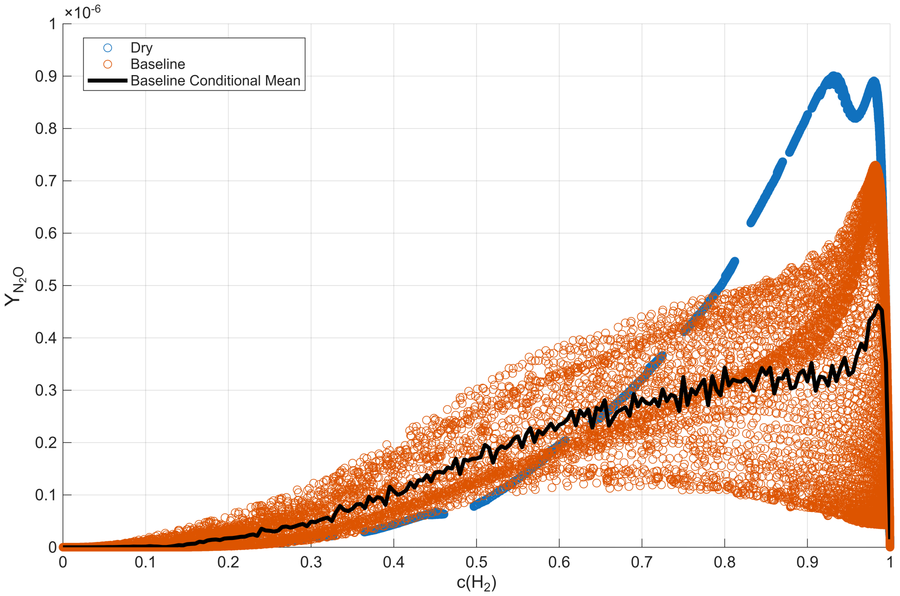

(a) N_2O mass fraction distribution in function of the hydrogen progress variable at t = 4ms.

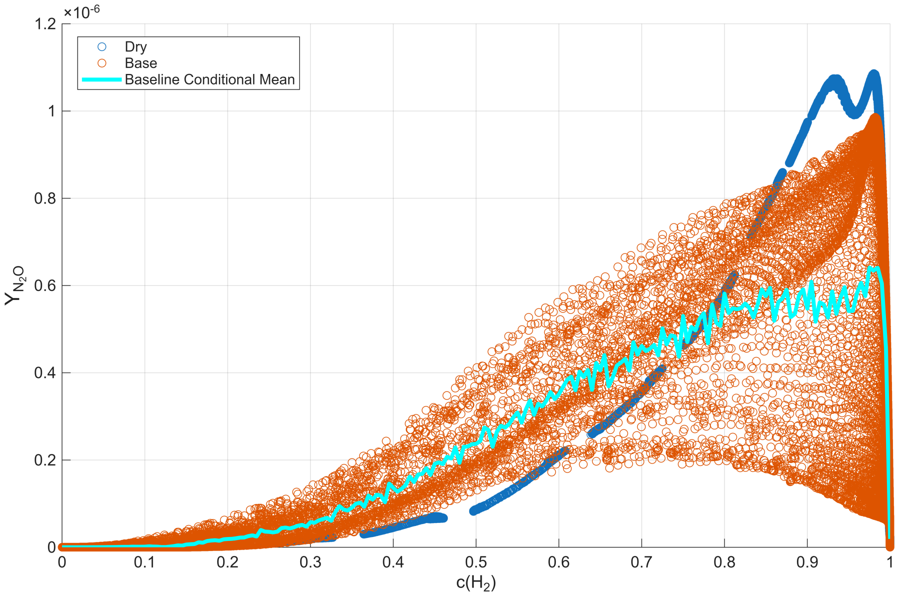

(b) N_2O mass fraction distribution in function of the hydrogen progress variable at t = 4ms, corrected for dilution.

Figure 5.11: N_2O mass fraction distribution at t = 4ms.

5.1.5. NO Emission Results

A similar trend is observed for f_I^{NO}, which is defined in Eq.(4.26). It can be seen in Figure 5.12: after an initial increase, in this case an increase that peaks below 20%, the mass fraction of NO drastically reduces with fluctuations similar to the previous two cases, but slightly delayed likely due to this chemical species' high residence time and its formation occurring mostly in the products zone, after the flame front (as it can be inferred from Figure 5.13a). Furthermore, it is possible to observe that even after 4 ms the NO mass fraction hasn't settle into an asymptotic behavior as clearly pronounce as the ones found in the previous two cases - also due to it's elevated formation time.

Nevertheless, a reduction of approximately 78% is found at $t = 4$ across the entire domain, compared to the dry case, due to the changes in chemical behavior, temperature changes, dilution, and reduction in rate of production of hydrogen previously established in this section.

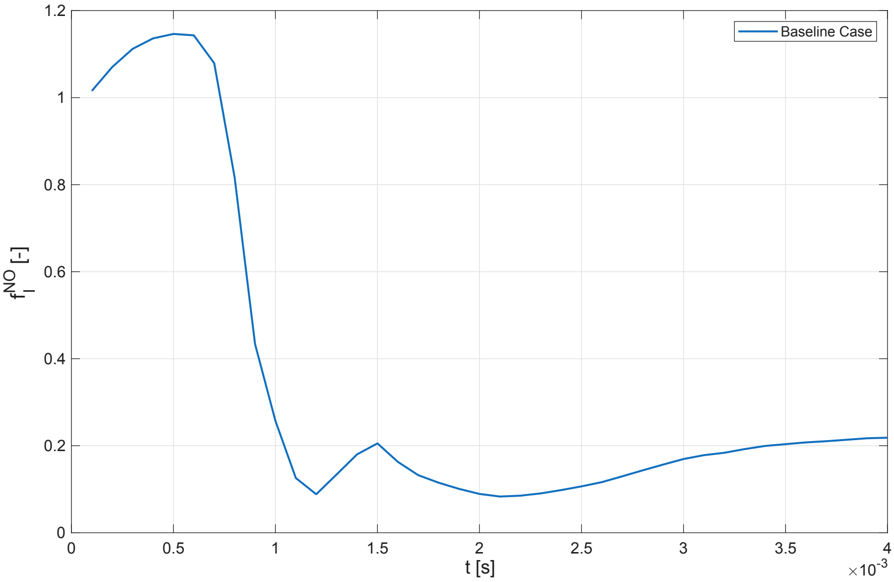

Figure 5.12: f_I^{NO} Time history with Water Injection, Baseline case (see Table 4.4 and Table 4.5).

Akin to the previous case with N_2O, from Figure 5.13 a slight increase in NO mass fractions at lower progress variable values can be observed, specially when correcting the data to account for dilution. This might be due to the reductions in temperature promoting the N_2O formation pathway and increase of N_2O around the same values for the progress variable. Nevertheless, the average value for Y_{NO} across the entire domain is clearly smaller and the peak NO mass fraction is severely reduced compared to the dry case. This peak is, as expected, located for both dry and baseline cases close to the product region, a sign of the importance of the Zeldovich NOx formation pathway, and it's sharp reduction corroborates the results found in literature by [13], and [39].

Overall the changes in NO observed likely stem from the reduction in H, O, and OH radicals hampering the formation of NNH and N_2O, reducing the importance of these mechanisms, combined with the reductions in temperature and O radicals reducing the importance of the Thermal NOx mechanim in accordance to the chemical reactions described in section 2.1.

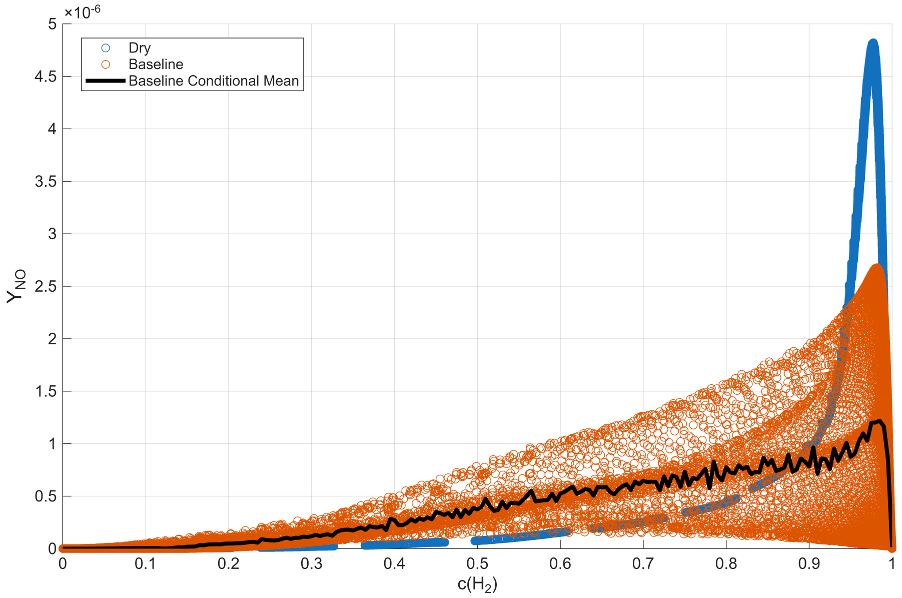

(a) NO mass fraction distribution in function of the hydrogen progress variable at t = 4ms.

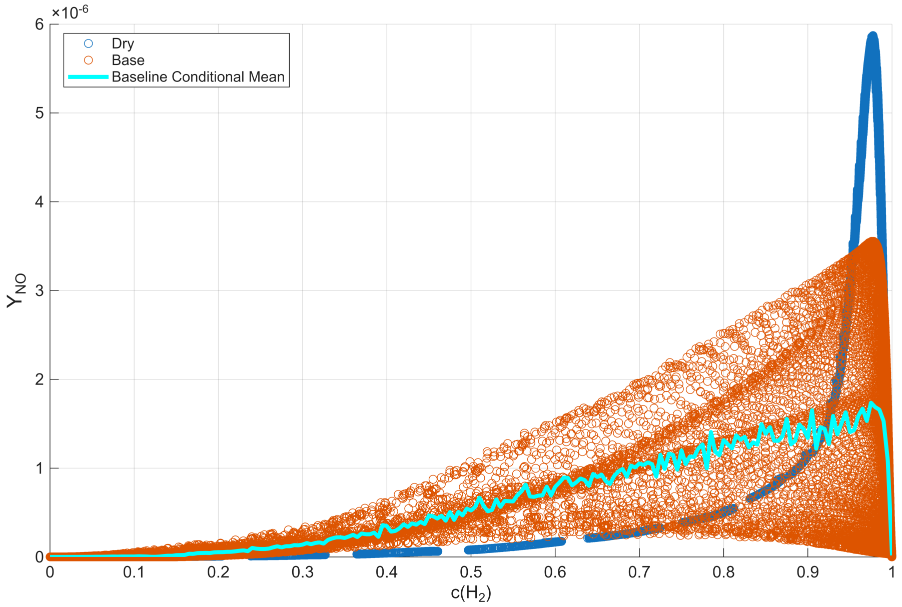

(b) NO mass fraction distribution in function of the oxygen progress variable at t = 4ms, corrected for dilution.

Figure 5.13: NO mass fraction distribution at t = 4ms.

5.1.6. Mixture Fraction and Preferential Diffusion Observations

As discussed in subsection 4.3.1, in a case where preferential diffusion is suppressed by using a unitary-Lewis diffusion model the curve corresponding to the Bilger mixture fraction (defined in Eq.(4.29)) takes the shape of an uniform straight line for all values of $c(\mathrm{H}_2)$ [42]; however, once preferential diffusion is accounted for, a local imbalance between fuel and oxidizer is created due different diffusivity among the fuel and oxydizer, which leads to a dip in the curve due to a leaning of the mixture ahead the flame. In the unstretched configuration, the mixture fraction smoothly relaxes to its inlet value as the progress variable approaches unity. In contrast, under strained conditions, the mixture fraction exhibits a noticeable overshoot at high values of the progress variable. This overshoot becomes more pronounced with increasing strain rate. (see, e.g., [62, 42]). Figure 5.14 shows a comparison between the 2D baseline case with water injection, the 1D dry stretched flamelet, and the 1D dry unstretched flamelet for the Bilger mixture fraction in function of the hydrogen progress variable. As can be observed, with the introduction of water into the domain, the characteristic dip associated with preferential diffusion disappears and is instead substituted by an early overshoot, followed by a small deep back to values close to the value at $c(\mathrm{H}_2) = 0$, and then a further enrichment. These two enrichments likely correspond to the evaporation of water droplets immediately as they enter the domain and as they approach the flame front, as the injected water becomes gaseous and leads to increases in the amount of H and O atoms in the domain. Since the Bilger mixture fraction is computed based on the amount of H and O contained in the reactants and products streams, the addition of water increases the presence of these elements, and thus the overshoot is canceled out. Moreover, the introduction of water causes dilution of the reactants and products, which may also effect the Bilger mixture fraction values. Since the lagrangian terms in the domain are integrated in the cells, it is hard to quantify the local water quantities in an Eulerian-Lagragian approach. Moreover, since the Bilger mixture fraction requires the water mass fraction for it's calculation, it is not possible to account for the dilution effect by simply removing the water contents, similar to the approach utilized in subsection 5.1.1. As such, since this discussion is not the main focus of the research, no analysis without accounting for dilution will be presented. Overall, it is observed that two enrichments caused by the evaporation of water droplets occur once the water is injected into the domain, but no meaningful conclusions relating the impact of water injection on preferential diffusion in highly strained hydrogen flames can be made, since removing the dilution effect proved to be complex due to the local effects being hard to quantify in an Eulerian-Lagragian approach.

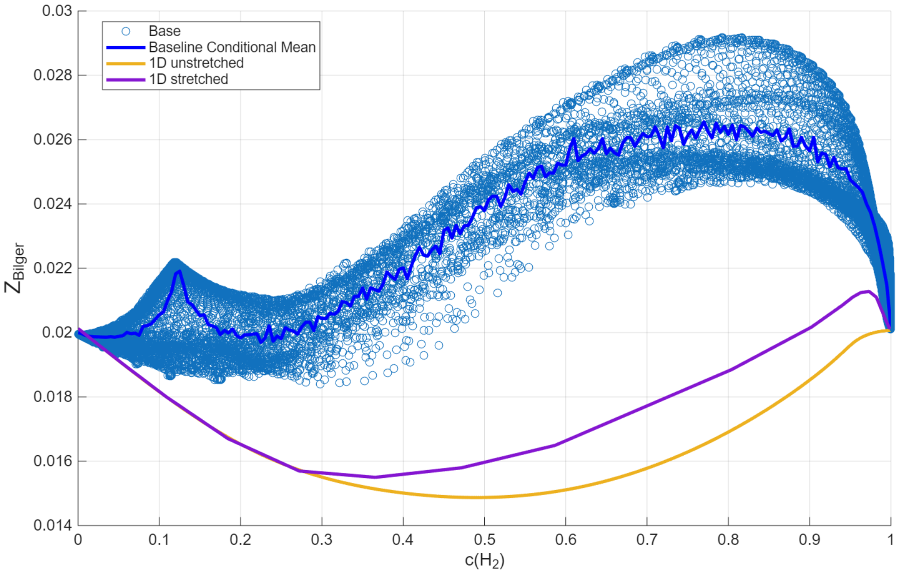

Figure 5.14: Bilger mixture fraction across the domain in function of the hydrogen progress variable, Baseline case.

5.2. Effect of Injection Velocity: Results and Observations

In this section the effects on the results caused by increasing the water injection velocity will be analyzed. For that effect two case studies - U10 and U20 where the injection velocity was increased to 10% and 20% of the reactants injection velocity (as described in Table 4.4) - will be compared to the results obtained for the baseline case, which were analyzed before in this chapter.

5.2.1. Radical Concentrations on the Flame Region

After 4 ms, it is observed that increasing the injection velocity leads to a reduction in the mass fractions of all radicals shown in Figures 5.15–5.21. For the O radical the baseline case showed a reduction of this species mass fraction level out at 93% compared to the dry case. When increasing the injection speed from 0.73 m/s to 1.46 m/s, the reduction value is approximately 95.8% and increasing it from 0.73 m/s to 2.92 m/s results in a reduction of 98.5% from the dry case. Similar reductions were attained for the rest of the radicals in the U10 case, registering a 98.3% reduction in H radicals, a 80.7% reduction in OH radicals, and an 8.3% increase in HO_2 mass fractions at $t = 4$ ms; however the case denominated U20 registered a 99.6% reduction in H radicals, a 90% reduction in OH radicals, but a 33.9% reduction in HO_2 mass fractions at the same time step. These results refer to the cases without accounting for dilution, correcting the data to account for it shows a reduction of 91.8%, 95.3%, and 98.4% (for Baseline, U10, and U20, respectively) of Y_{O} compared to the corrected dry case; a reduction of 94.2%, 98.0%, and 99.5% (for Baseline, U10, and U20, respectively) of Y_{H} compared to the corrected dry case; a reduction of 68.6%, 79.3%, and 89.1% (for Baseline, U10, and U20, respectively) of Y_{OH} compared to the corrected dry case; and an increase of 63.7% (for both Baseline and U10 cases), and a reduction of 0.1% , (for the U20 case) of Y_{HO_2} compared to the corrected dry case. HO_2 is more susceptible to the dilution effect since it presents lower mass fraction values.

The reduction in HO_2 presence for the case U20 contrasts with the increases observed in the baseline and U10 cases. Upon further inspection of Figure 5.21 and Figure 5.22, it is observable that when the injection velocity increases the mass fraction of this radical decreases at $t = 4$ ms. Le Cong and Dagaut [29] showed that the production of HO_2 in the presence of water tend to increase due to chemical and physical changes caused by water injection, but for U20 the results obtained seem to diverge from this pattern. This might be caused by the heavy reduction in H radicals observed in Figure 5.17 for U20, where a reduction in H radicals of 99.5% (accounting for dilution) is observed and since these radicals are necessary for the formation of HO_2 from the chemical reaction $H + O_2 + (M) \longrightarrow HO_2 + (M)$ this reduction might negatively influence the mass fraction of HO_2. Furthermore, in subsection 5.2.2 specifically in Figure 5.23, it can be observed an even further reduction of the consumption rate of hydrogen as the injection velocity of water is increased. This may also negatively impact the amount of HO_2 mass fraction on the flame front and thus further justifying the trend observed.

Overall, increasing injection velocity is shown to enhance the changes in O, H, and OH radicals observed in subsection 5.1.1, meaning that a sharper decrease in these species mass fraction is observed as the injection velocity is increased. Furthermore, the decrease after peaking of HO_2 is observed to be sharper than the baseline case for U20, but less pronounced in U10. These results are indicative of a sharper reduction in hydrogen reactivity as the water injection velocity is incremented, as such it is expected that the rate of production of hydrogen will decrease in absolute value as this parameter is increased. Moreover, the sharper reduction in O, H, and OH radicals should translate into an even more accentuated reduction in emissions, as these radicals are necessary species in the NOx formation mechanisms, which are described in section 2.1.

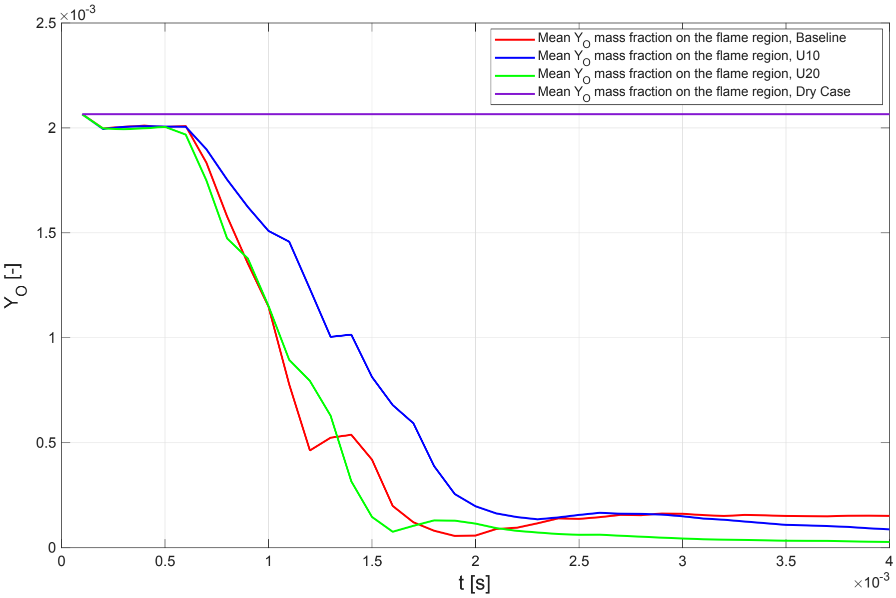

Figure 5.15: Mean Y_{O} as a function of time. Effect of the injection velocity (see Table 4.4 and Table 4.5).

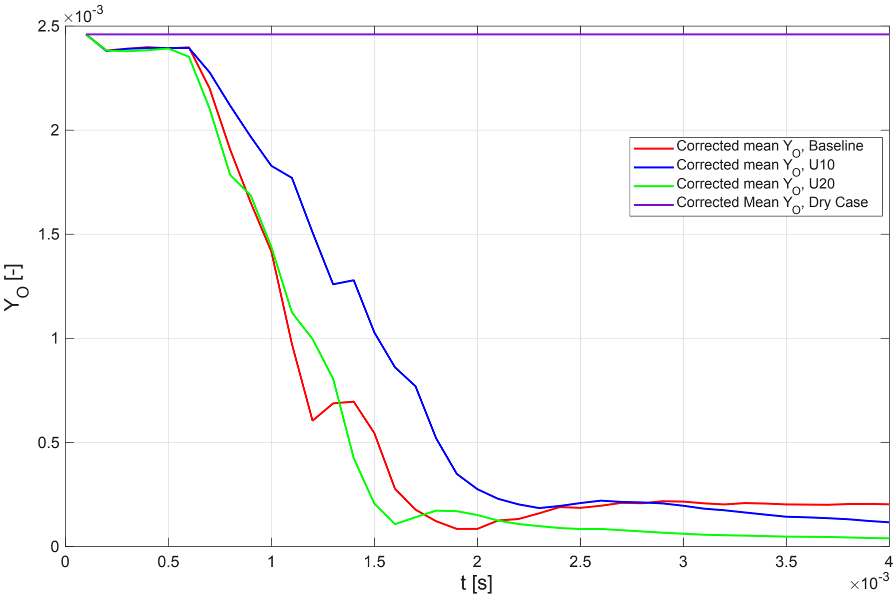

Figure 5.16: Mean Y_O as a function of time. Effect of the injection velocity (see Table 4.4 and Table 4.5) and corrected to account for dilution.

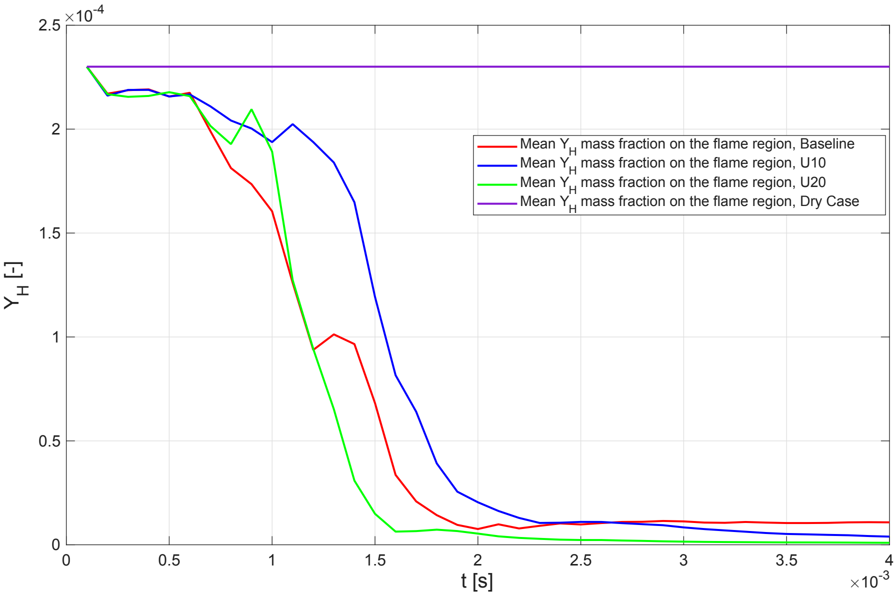

Figure 5.17: Mean Y_H as a function of time. Effect of the injection velocity (see Table 4.4 and Table 4.5).

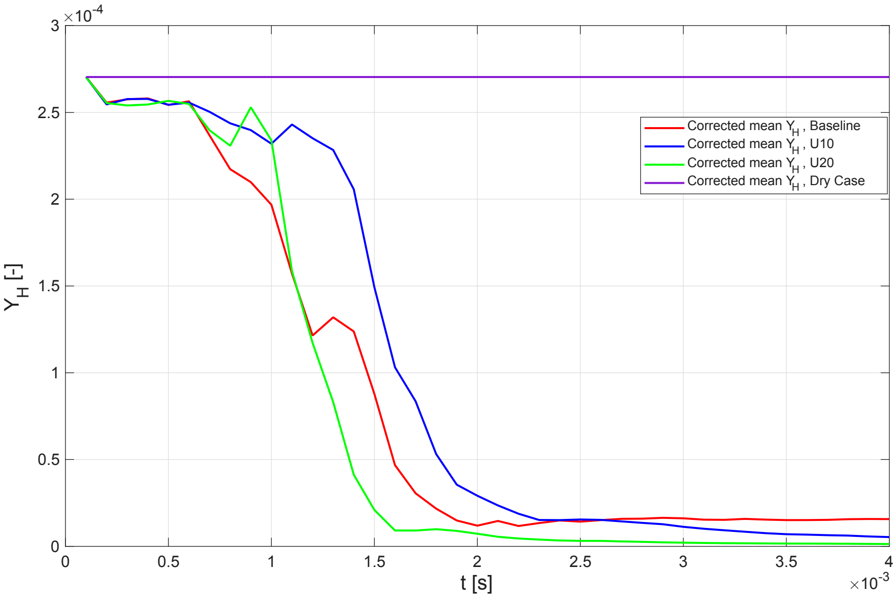

Figure 5.18: Mean $\mathrm{Y_H}$ as a function of time. Effect of the injection velocity (see Table 4.4 and Table 4.5) and corrected to account for dilution.

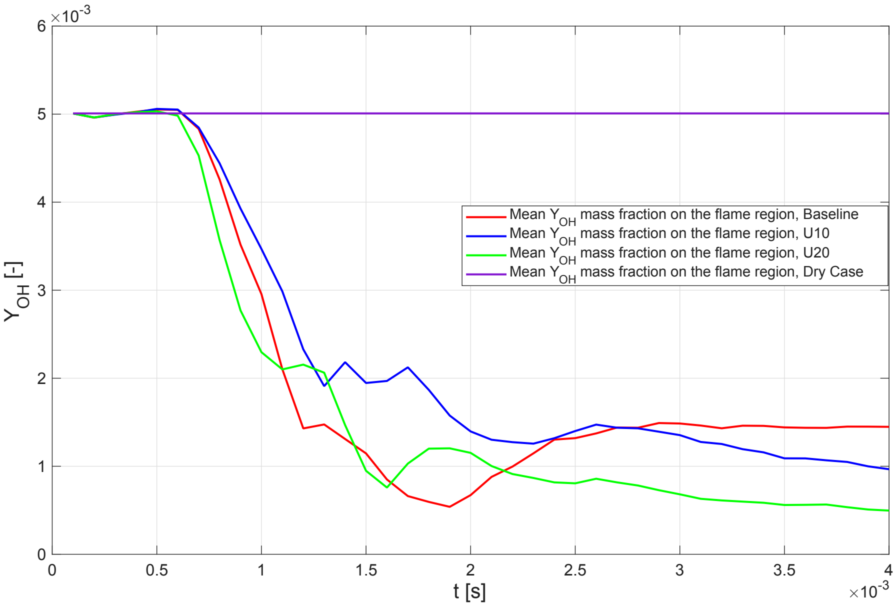

Figure 5.19: Mean $\mathrm{Y_{OH}}$ mass fraction on the flame region as a function of time. Effect of the injection velocity (see Table 4.4 and Table 4.5).

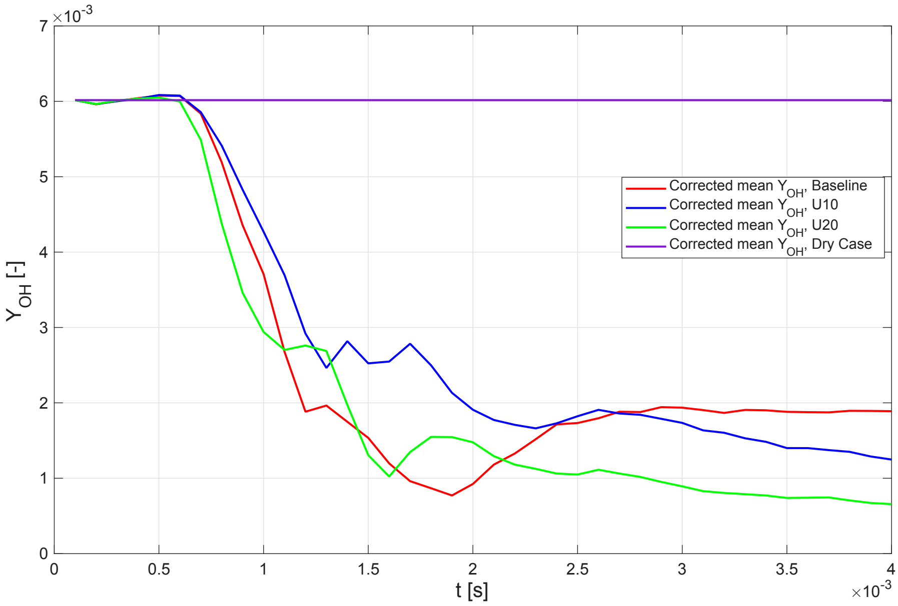

Figure 5.20: Mean Y_{OH} as a function of time. Effect of the injection velocity (see Table 4.4 and Table 4.5) and corrected to account for dilution.

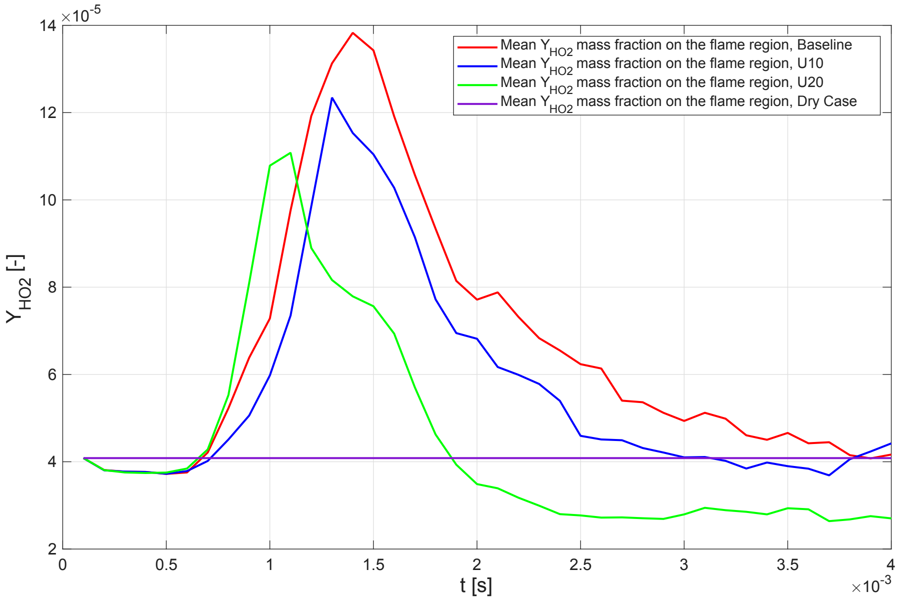

Figure 5.21: Mean $Y_{\mathrm{HO_2}}$ mass fraction on the flame region as a function of time. Effect of the injection velocity (see Table 4.4 and Table 4.5).

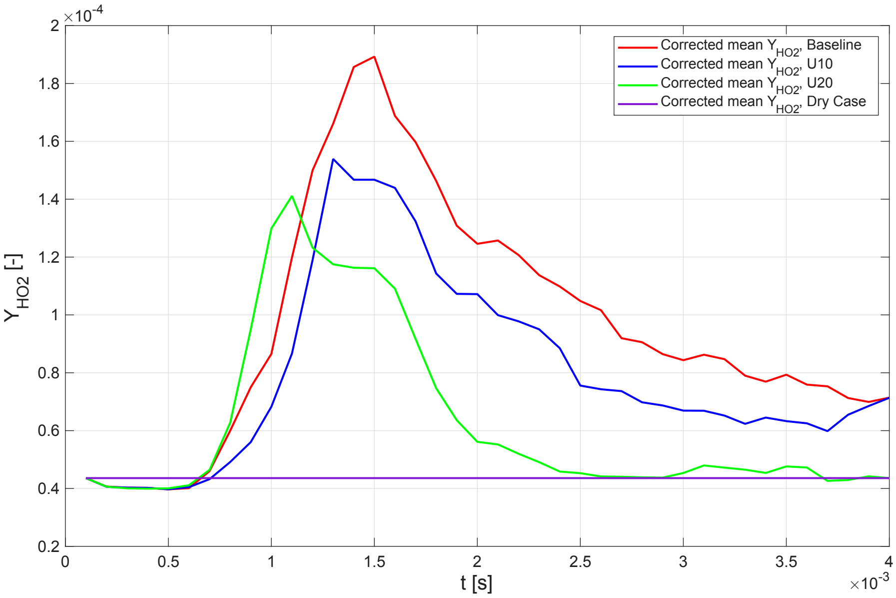

Figure 5.22: Mean $\mathrm{Y}_{\mathrm{HO_2}}$ as a function of time. Effect of the injection velocity (see Table 4.4 and Table 4.5) and corrected to account for dilution.

5.2.2. Temperature and Hydrogen Rate of Production

Regarding the effect on temperature and hydrogen rate of production caused by increasing the injection velocity of water, in order to analyze how the injection velocity impacts the reactivity, Figure 5.23 shows the mean hydrogen rate of production averaged across the domain at $t = 4$ ms. It is observable that after 4 ms, the hydrogen rate of production is less negative for the cases with the injection velocity of water higher than the baseline. Figure 5.24 also shows a reduction in mean temperature with increasing injection velocity in the domain region where the temperature is on the 10^{th} percentile of temperature. This effect is more pronounced when the injection velocity increases from 5% to 10%, than when it increases from 10% to 20%. In general, the results presented in these figures corroborate what would be expected from the analysis done in subsection 5.2.1: a decrease in the absolute value of the hydrogen rate of production is observed as the injection velocity of the droplets increases and a reduction in the mean temperature is observed. This occurs likely due to the increase in spray injection magnitude causing the droplets to travel with a higher momentum and evaporating closer to the flame front as a consequence.

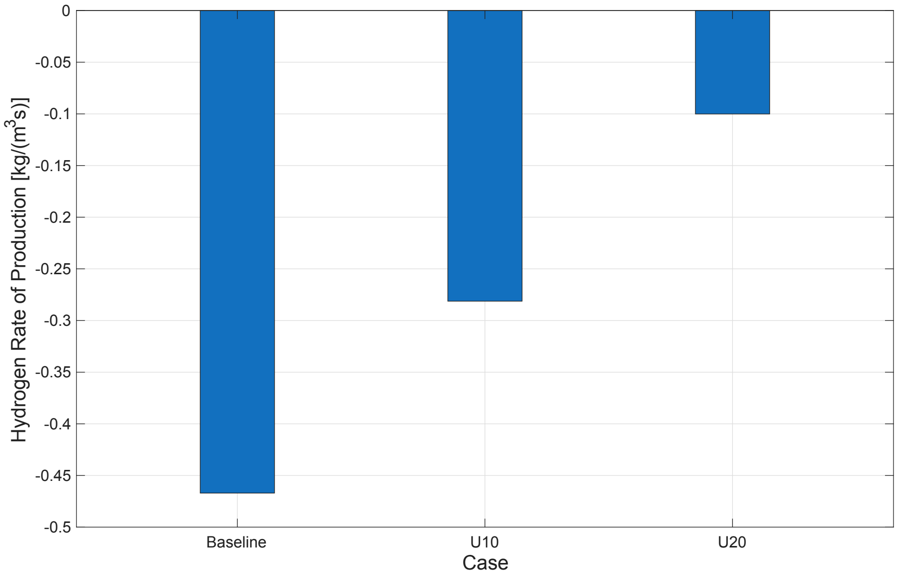

Figure 5.23: Mean over domain of hydrogen rate of production. Effect of the injection velocity (see Table 4.4 and Table 4.5)

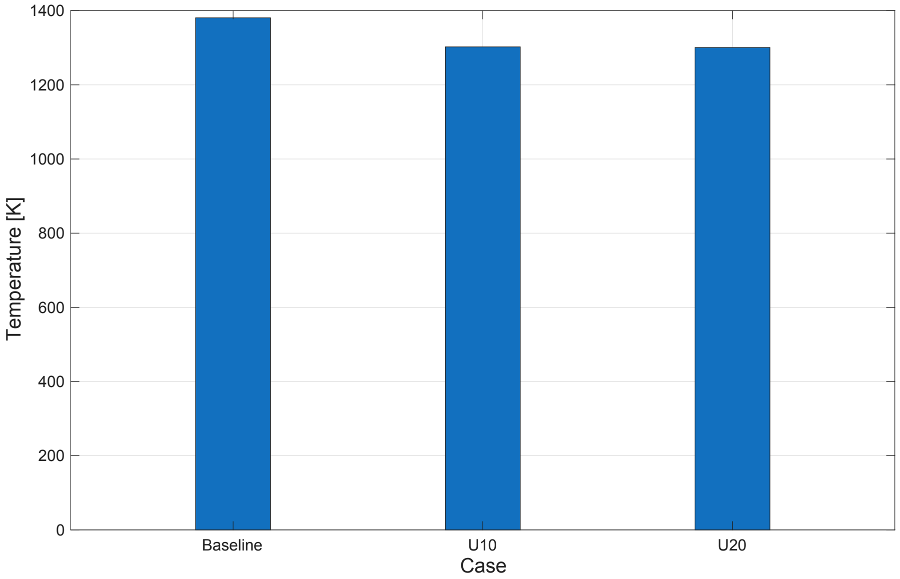

Figure 5.24: Mean cell temperature. Effect of the injection velocity (see Table 4.4 and Table 4.5)

Figure 5.25 corroborates the idea behind exposed in the last paragraph by showing the distribution of the temperature of each cell plotted against the molecular hydrogen progress variable. As it can be seen, even though the peak temperature's reduction is fairly small, the vast majority of the cells present a smaller temperature value scaling with the injection velocity, i.e, the higher the injection velocity, the smaller is the average cell temperature. This is made specially obvious when observing the trends exposed for each case conditional mean.

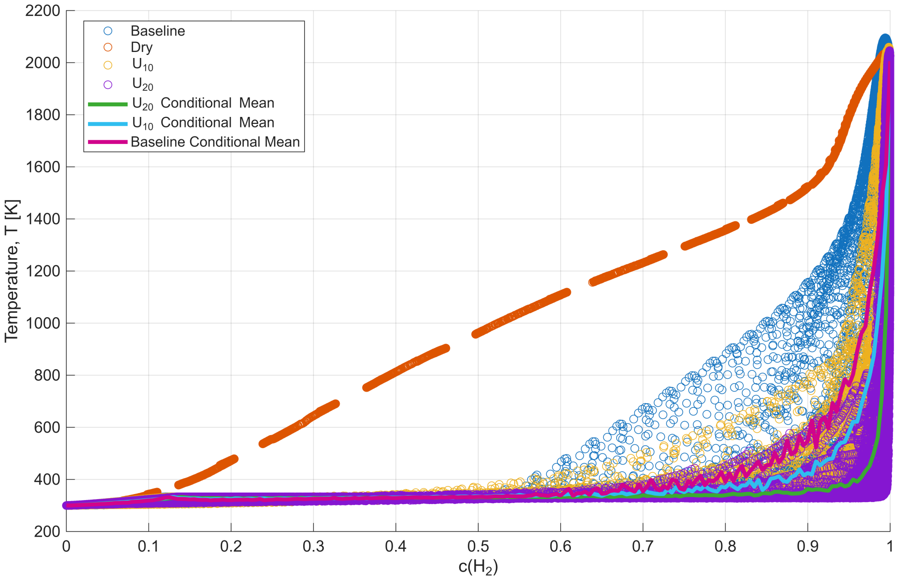

Figure 5.25: Temperature distribution at t = 4ms: injection velocity impact.

5.2.3. **NNH** Emission Results

Figure 5.26 shows the value of the gain figure f_I^{NNH} at $t = 4$ ms. As it can be observed, the increase in injection velocity causes an even further reduction in this species presence, since at $t = 4$ ms the reduction in f_I^{NNH} is 99% for the U10 and 99.6% for case U20, compared to the 97.4% from baseline, when not accounting for dilution. Once dilution is accounted for, the reduction observed is 97.1% for the baseline case, 98.9% for the U10 and 99.55% for case U20 (correspondent to a value of f_I^{NNH} of 0.029, 0.011, and 0.0045, respectively). These results are expected based on the reductions in radical presence observed in subsection 5.2.1 (specifically the sharp reduction in H radicals presented in Figure 5.17 and Figure 5.18) and the reduction in hydrogen rate of production described in Figure 5.23, however they are counterintuitive since injecting the water at higher velocities should result in a decrease in residence time, and thus negatively impact the emissions results. However, post processing in ParaView [64] revealed that while there is a small decrease in residence time with increasing water injection velocity, the evaporation of water droplets occurs closer to the flame front, which can possibly lead to a higher effectiveness of the water injection, and thus explaining the observed results and behavior.

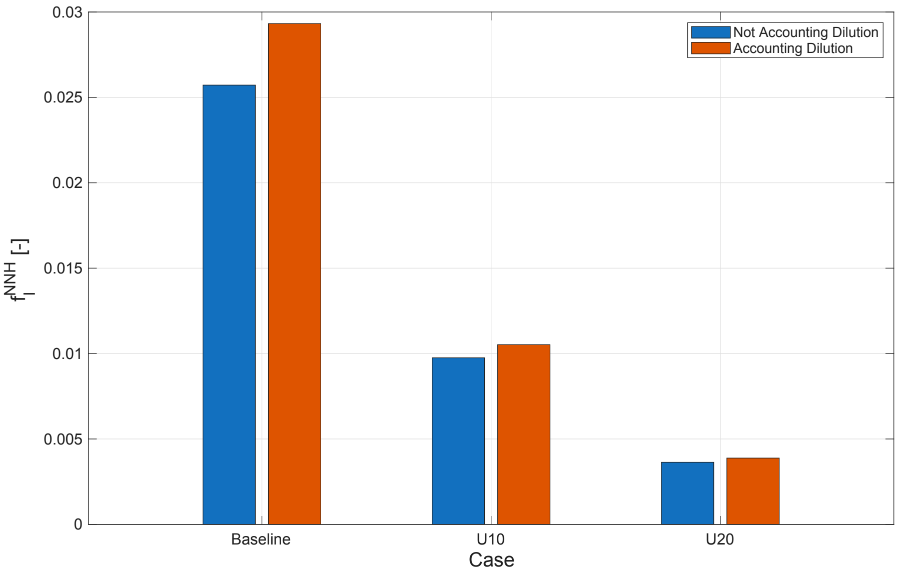

Figure 5.26: f_I^{NNH} at $t = 4$ ms. Effect of the injection velocity (see Table 4.4 and Table 4.5).

Furthermore, Figure 5.27 and Figure 5.28 provide information about the mass fraction of this species for all cells of the domain plotted against the molecular hydrogen progress variable (in the second figure it is presented accounting for the dilution effect). As it can be observed, the decrease is quite significant for all three cases, but it is specially observable for U20 as it is more clearly shown in Figure 5.27b and Figure 5.28b. Moreover, the phenomena of the peak Y_{NNH} being found closer to higher values of $c(\mathrm{H}_2)$ is more pronounced as the injection velocity magnitude increase, suggesting that as water is injected at a faster rate the flame reaction zone moves towards the products region, something clearly observed in Figure 5.27b.

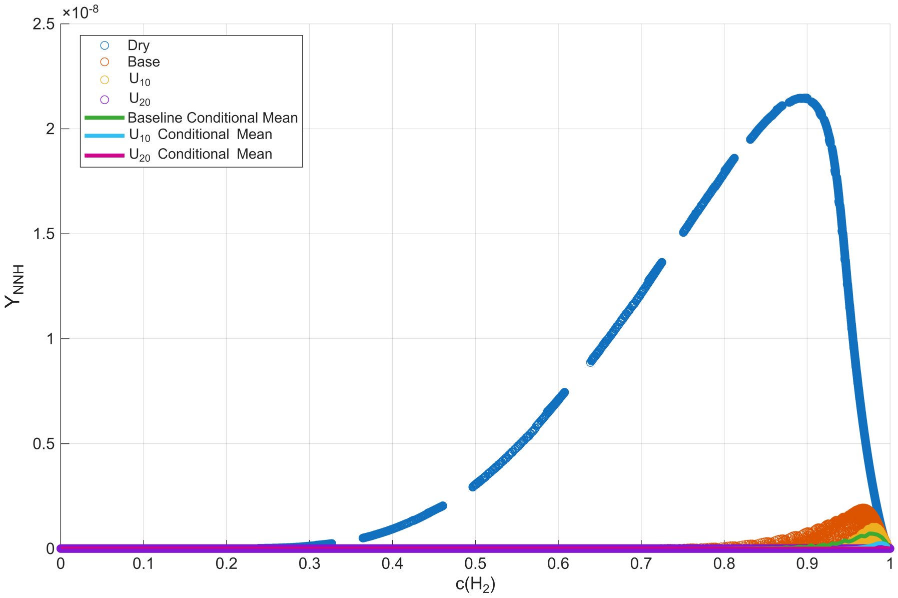

(a) NNH mass fraction distribution in function of the hydrogen progress variable at t = 4ms, with dry case.

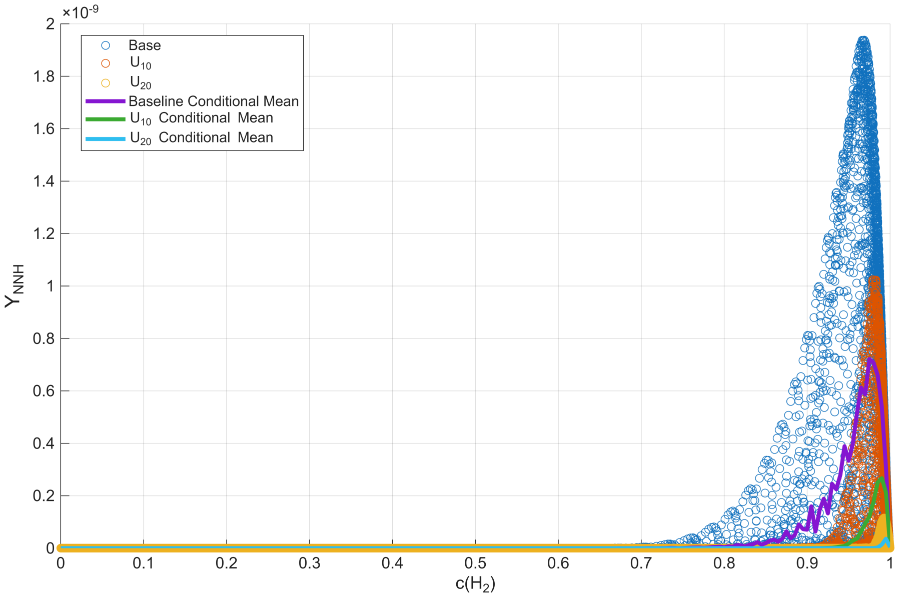

(b) NNH mass fraction distribution in function of the hydrogen progress variable at t = 4ms, without dry case.

Figure 5.27: NNH mass fraction distribution in function of the hydrogen progress variable at t = 4ms: injection velocity impact.

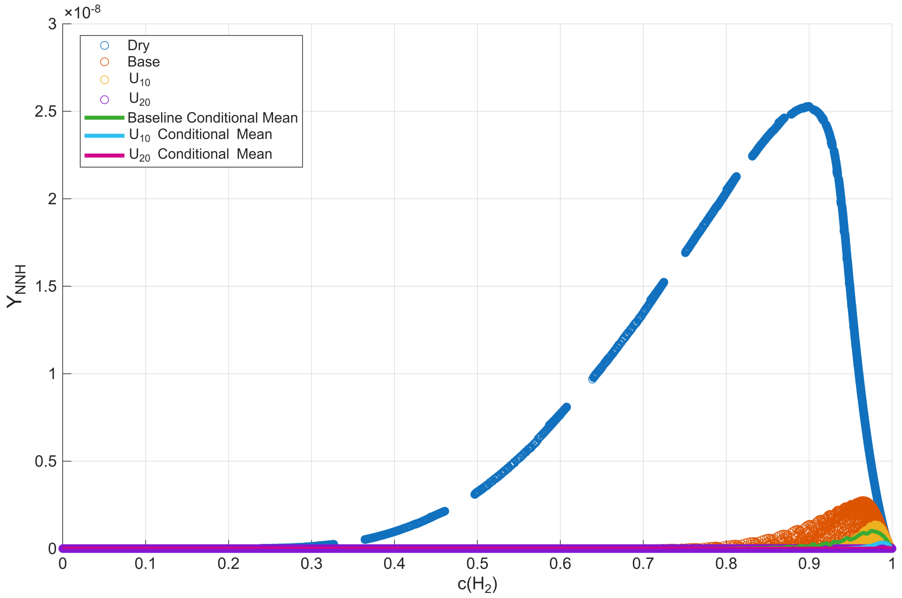

(a) NNH mass fraction distribution in function of the hydrogen progress variable at t = 4ms, with dry case & accounting for dilution.

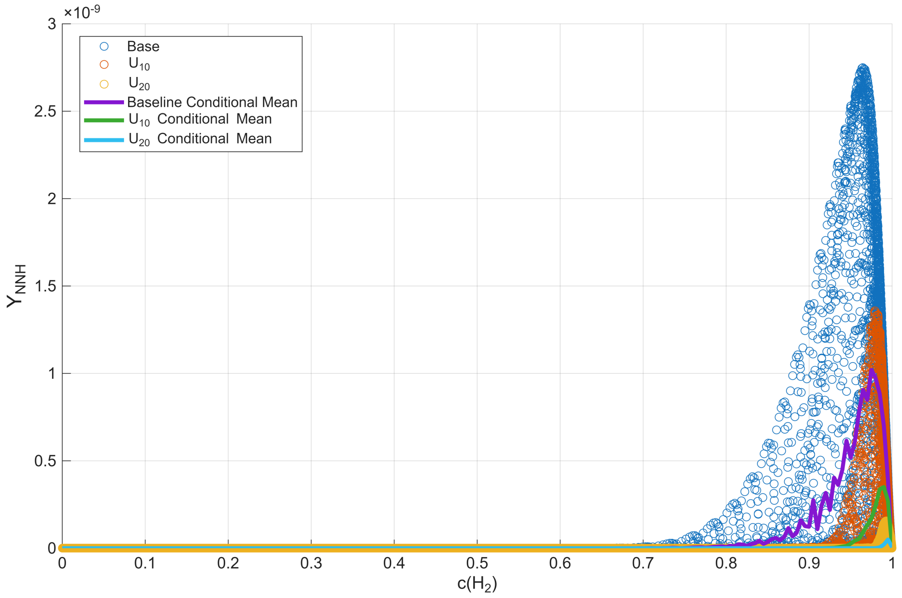

(b) NNH mass fraction distribution in function of the hydrogen progress variable at t = 4ms, without dry case & accounting for dilution.

Figure 5.28: NNH mass fraction distribution in function of the hydrogen progress variable at t = 4ms, accounting for dilution: injection velocity impact.

5.2.4. N_2O Emission Results

A similar trend to the one observed in Figure 5.10 is found for the cases U10 and U20. As it can be seen in Figure 5.29, he average reduction at $t = 4$ ms is approximately 72.6% for U10 and 88% for U20, while not accounting for dilution. When corrected to account for it, the reductions observed are approximately 56% for the baseline case, 68.5% for U10, and 86% for U20. They stem from the same reasons explained in subsection 5.1.4, but aggravated by an even further reduction in radical's presence, bigger reduction in hydrogen reactivity, and more significant decrease of flame temperature. These results are justifiable from what is observed in the analysis done in subsection 5.2.1: the N_2O mechanism for NOx formation initiates with the recombination of molecular nitrogen into N_2O by reacting with oxygen radicals, Figures 5.15 and 5.16 show that with increasing injection velocity a larger reduction of O is observed, so an overall reduction in this species presence as the injection velocity is increased is expected.

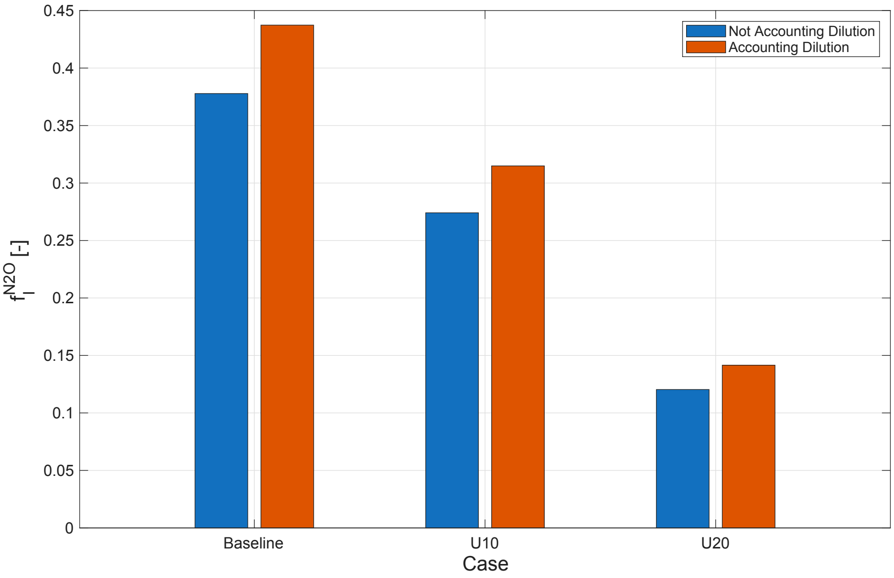

Figure 5.29: $f_I^{\mathrm{N_2O}}$ at $t = 4$ ms. Effect of the injection velocity (see Table 4.4 and Table 4.5).

In Figure 5.30 it is observable the mass fraction distribution of N_2O at $t = 4$ ms plotted against $c(\mathrm{H_2})$, while Figure 5.31 shows the mass fraction distribution of N_2O at $t = 4$ ms plotted against $c(\mathrm{H_2})$ and corrected for dilution. From these two figures it is possible to observe an even further reduction of N_2O formation closer to the product regions, in fact for the U20 case the absolute maximum of $Y_{\mathrm{N_2O}}$ occurs even before the flame front. Nevertheless, a small peak is still found for this case at $c(\mathrm{H_2}) = 0.99$. These two figures clearly illustrate how the increase in injection velocity, clearly reduces this species concentration not only due to dilution, but also by altering the chemical reactions and pathways favored, since the distribution of this species mass fraction severely changes as the injected water mass flow rate increases. The reasons for this were already discussed in subsection 5.1.4, but they likely stem from the sharp reduction in O radicals and the decrease in temperature and humidity favoring this species formation before the flame front.

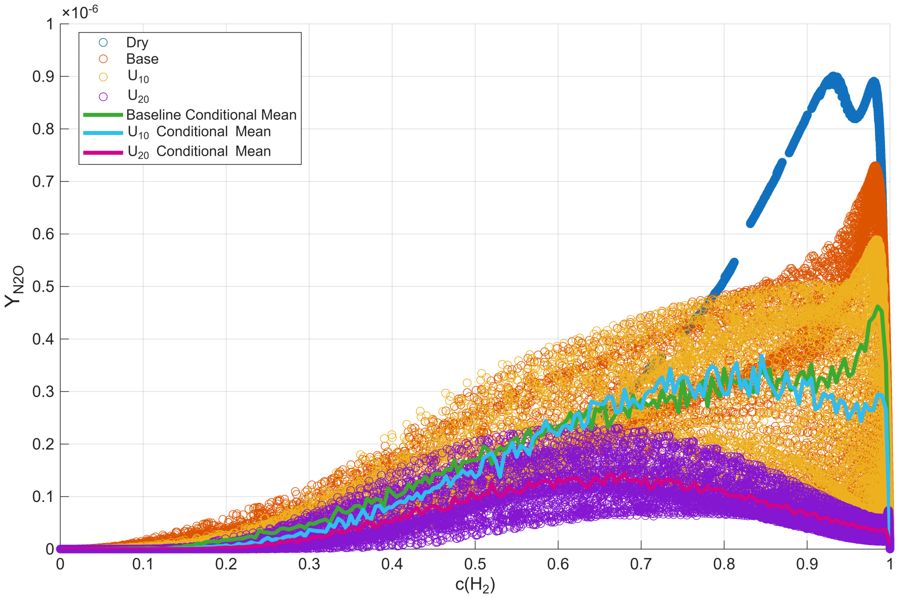

(a) N_2O mass fraction distribution in function of the hydrogen progress variable at t = 4ms, with dry case.

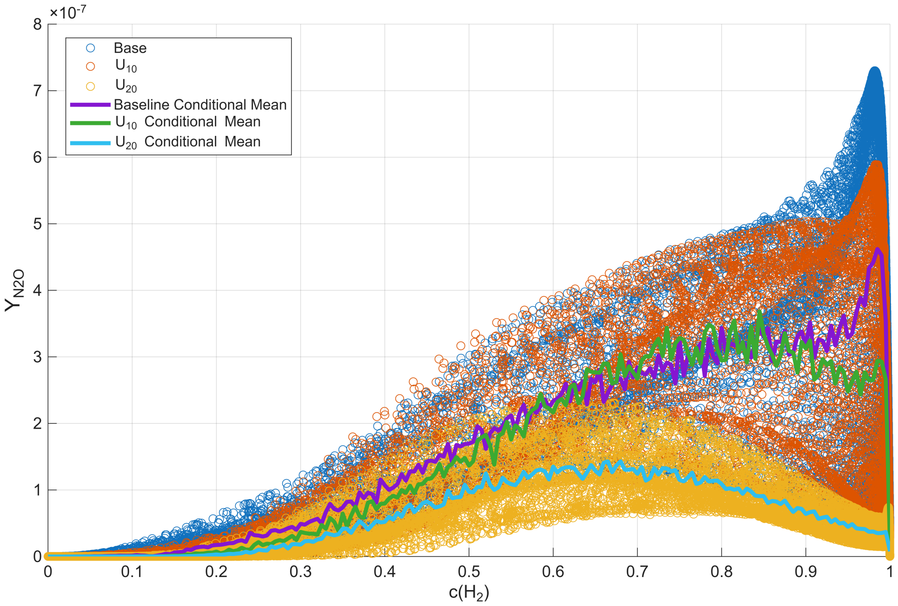

(b) N_2O mass fraction distribution in function of the hydrogen progress variable at t = 4ms, without dry case.

Figure 5.30: N_2O mass fraction distribution in function of the hydrogen progress variable at t = 4ms.

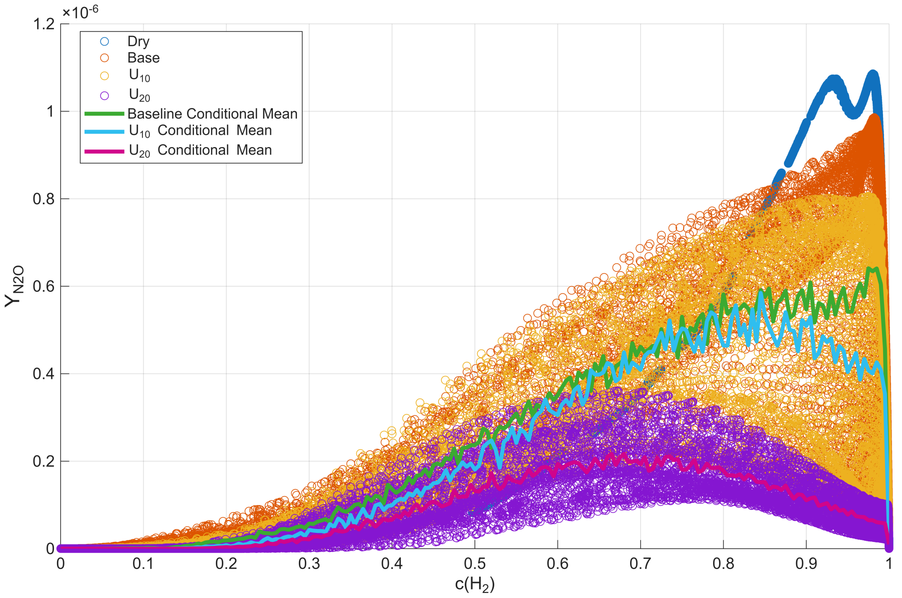

(a) N_2O mass fraction distribution in function of the hydrogen progress variable at t = 4ms, with dry case & accounting for dilution.

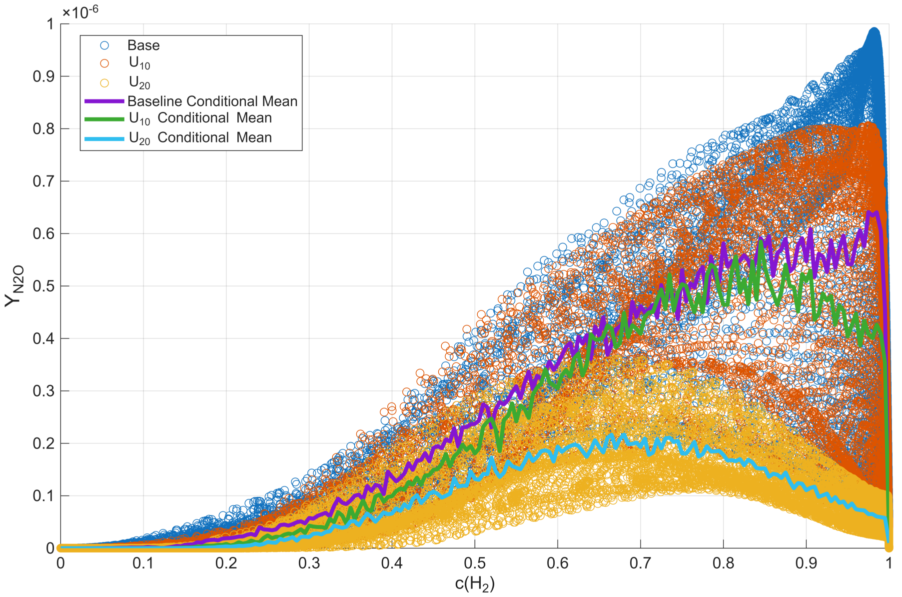

(b) N_2O mass fraction distribution in function of the hydrogen progress variable at t = 4ms, without dry case & accounting for dilution.

Figure 5.31: N_2O mass fraction distribution in function of the hydrogen progress variable at t = 4ms, accounting for dilution: injection velocity impact.

5.2.5. **NO** Emission Results

A similar trend to the one observed in Figure 5.12 is found for the cases U10 and U20. As it can be seen in Figure 5.32,the average reduction at $t = 4$ ms is approximately 90.9% for U10 and 97.7% for U20, without accounting for dilution. Once dilution is accounted for, the reductions observed are, approximately, 74% for the baseline case, 89.5% for U10, and 97.1% for U20. They stem from the reductions in radicals previously observed in subsection 5.2.1, which consequently lead to the reduction of the presence of NNH and N_2O - key species for NO formation through the NOx formation pathways discussed in section 2.1. The reduction average flame temperature and reduction of temperature across the domain in general also contribute significantly by hindering the Thermal NOx formation pathway.

Figure 5.33 and Figure 5.34, that plot the mass fraction distribution of NO at $t = 4$ ms against $c(H_2)$ with and without the dilution, respectively, help shine light into these differences. As it can be seen, the peaks of Y_{NO} close to the products zone (i.e, closer to $c(\mathrm{H}_2) = 1$) are severely reduced in U10 and U20. These peaks are mostly due to the Zeldovich mechanism, that is heavily reduced when the flame temperature is decreased. Furthermore, the injection of water also increases Y_{NO} closer to the reactants zone, likely due to the increase in N_2O caused by the lower temperatures, droplet evaporation, and higher humidity promoting the N_2O NOx formation pathway at before the flame front; however with increasing water injection velocity even Y_{NO} at this progress variable ranges seems to decrease. For both U10 and U20, the peak of NO mass fraction occurs before the flame front, showing the effectiveness of water in reducing the NOx formation through the Thermal NOx pathway.

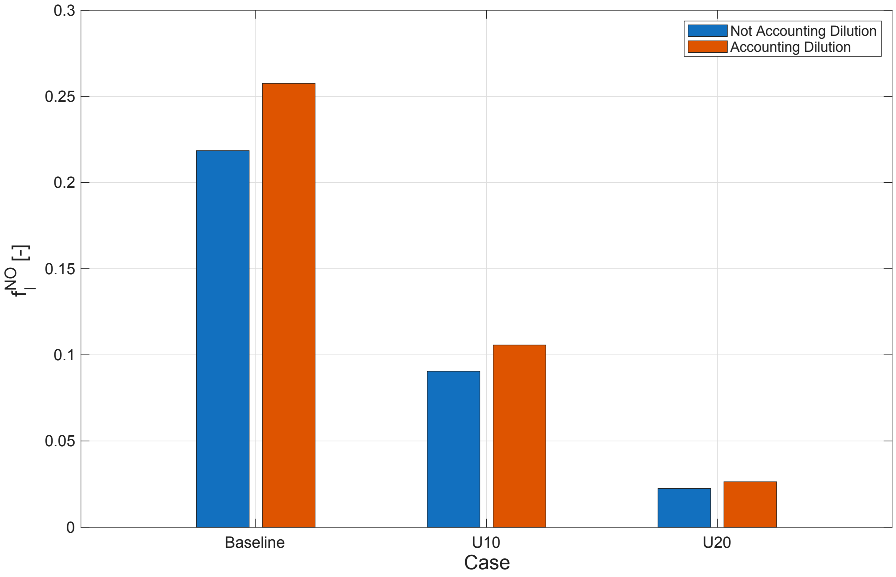

Figure 5.32: f_I^{NO} Time history with Water Injection Velocity (see Table 4.4 and Table 4.5).

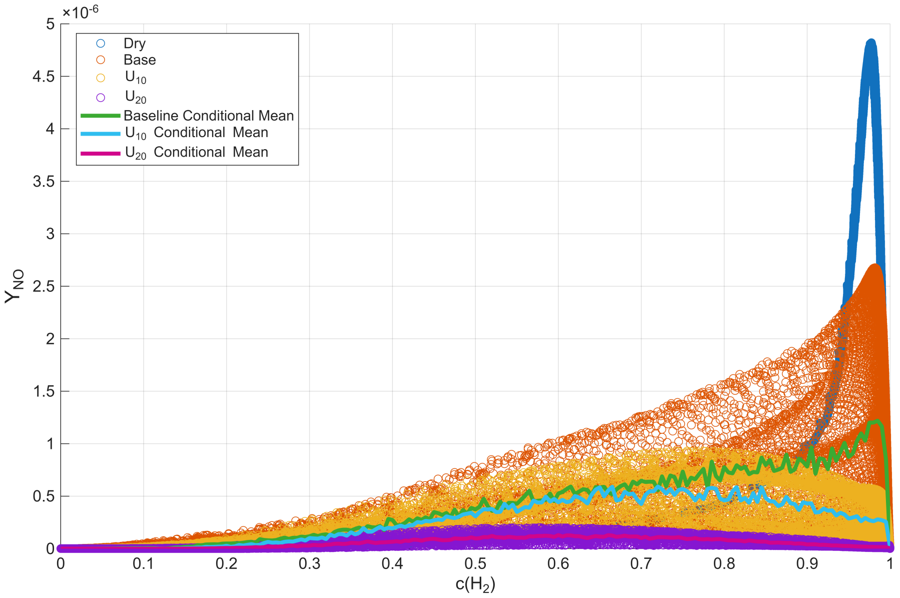

(a) NO mass fraction distribution in function of the hydrogen progress variable at t = 4ms, with dry case.

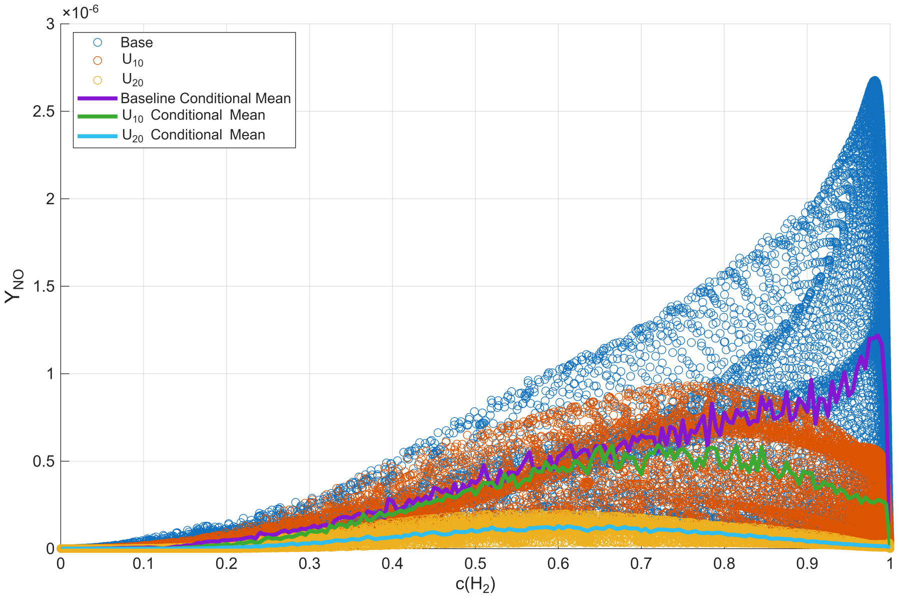

(b) NO mass fraction distribution in function of the hydrogen progress variable at t = 4ms, without dry case.

Figure 5.33: NO mass fraction distribution in function of the hydrogen progress variable at t = 4ms: injection velocity impact.

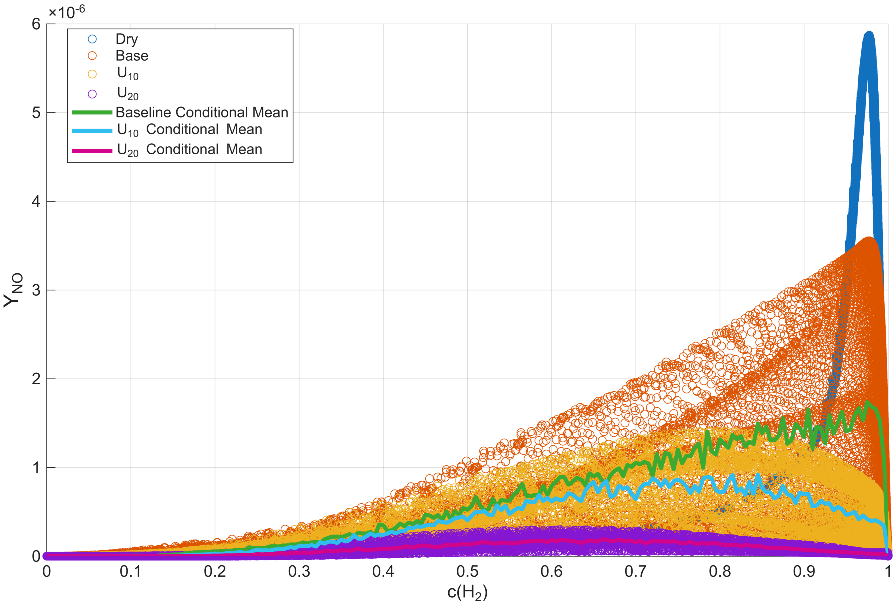

(a) NO mass fraction distribution in function of the hydrogen progress variable at t = 4ms, with dry case & accounting for dilution.

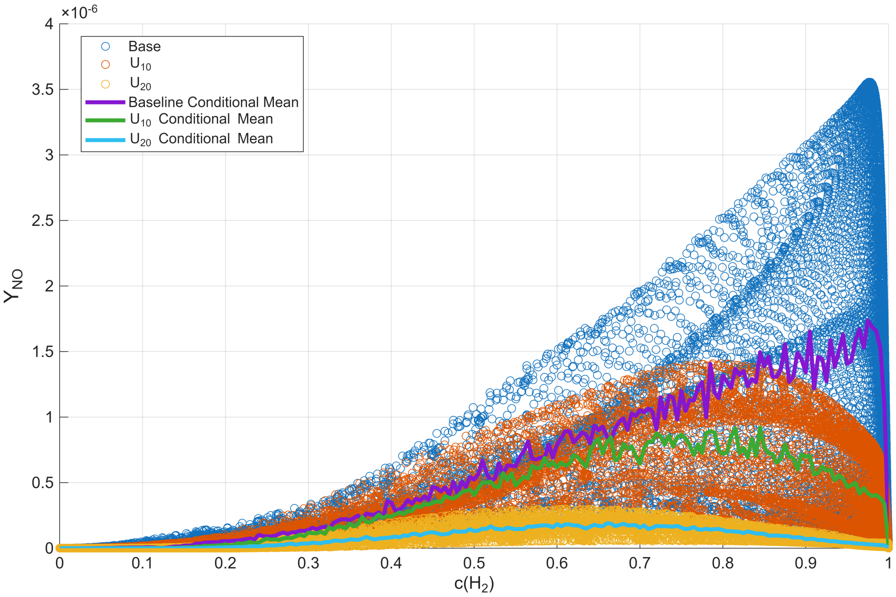

(b) NO mass fraction distribution in function of the hydrogen progress variable at t = 4ms, without dry case & accounting for dilution.

Figure 5.34: NO mass fraction distribution in function of the oxygen progress variable at t = 4ms, accounting for dilution: injection velocity impact.

5.2.6. Observations on the Emission Results

The results observed in this section shed light into the effects of increasing water injection velocity into the flamelet. As it is observable, increasing water injection velocity produces greater reductions in NO formation likely due to it's even further reduction of radical presence, diminishing hydrogen rate of consumption, and reduction of flame temperature possibly caused by the water particle higher momentum increasing their concentration around the midplane and preventing them from escaping through the domain sides. This is evident in the reductions seen in Y_{NO} after the flame front, closer to the products zone, which is usually associated with the Zeldovich NOx formation pathway. This formation pathway is specially relevant in the dry case and baseline case, but as the velocity of water injected increases it's importance diminishes greatly. The observed reduction is caused mainly by the temperature reduction observed in Figure 5.24 and Figure 5.25, as the chemical reactions behind the formation of Thermal

NOx require high temperatures to occur. The observed results concur with what [38], [40], and Banerjee et al. [13]observed: the temperature decreases serve to hamper the Thermal NOx formation, and thus help reduce the NOx emissions in flames.

5.3. Effect of Increasing Droplet SMD: Results and Observations

In this section the effects on the results caused by increasing the Rosin-Rammler SMD of the droplet will be analyzed. For that effect two case studies - SMD15 and SMD25 where the droplet SMD was increased by a factor of 15$\%$ and 25% in relation to the baseline case.

5.3.1. Radical Concentrations on the Flame Region

Figures 5.35, 5.37, 5.39, and 5.41 provide information regarding the variation in relevant radical's mass fraction across the simulated time frame for the baseline, SMD15, and SMD25 cases. As it can be observed, across the four aforementioned figures, as the SMD is increased the necessary time to reach a quasi-steady state slightly increases as well, likely due to difference in how the droplets physically interact with the simulation domain. Nevertheless, once this state is reached, the observable results show a small variance in Y_{O} and Y_{H} when the SMD is incremented, with the values for this species mass fractions being slightly lower with increasing SMD (the changes correspond to a approximate 8% decrease in Y_{O} from the baseline case to the SMD25 case and a reduction of 17.5% in Y_{H} between the baseline case and SMD25); moreover, a reduction of 7% between SMD25 and baseline is verified for Y_{OH} and an increase of 11% in $Y_{\mathrm{HO_2}}$ is observable between SMD25 and the baseline case.

These percentages are kept fairly similar once dilution is accounted for, as seen in figures 5.36, 5.38, 5.40, and 5.42, since the mass flow rate of water in all cases is the same and thus once water is removed the consequential increment in mass fraction is similar for all three cases.

The overall reasons for the changes observed in radical concentration are discussed in subsection 5.1.1. The presented data suggests that increasing SMD has a small positive impact in reducing important radicals present, likely due to larger droplet volume requiring more energy to evaporate, thus evaporating closer to the flame front, and consequently being more effective. From these results one expects to see slight reductions in hydrogen rate of production and on emissions of NOx related species, albeit much less significant as the ones observed in the previous section where the injection velocity of the water spray was varied.

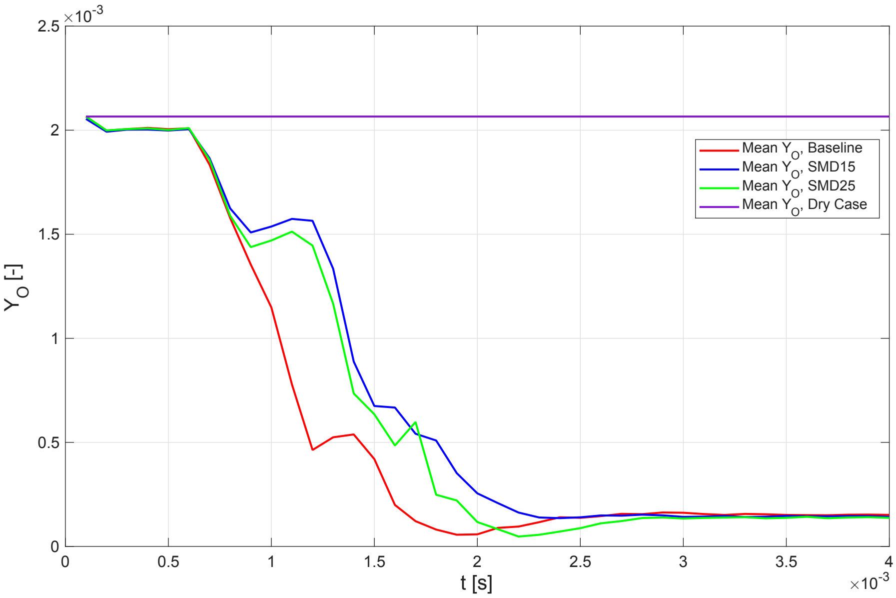

Figure 5.35: Mean Y_{O} as a function of time. Effect of SMD increment (see Table 4.4 and Table 4.5).

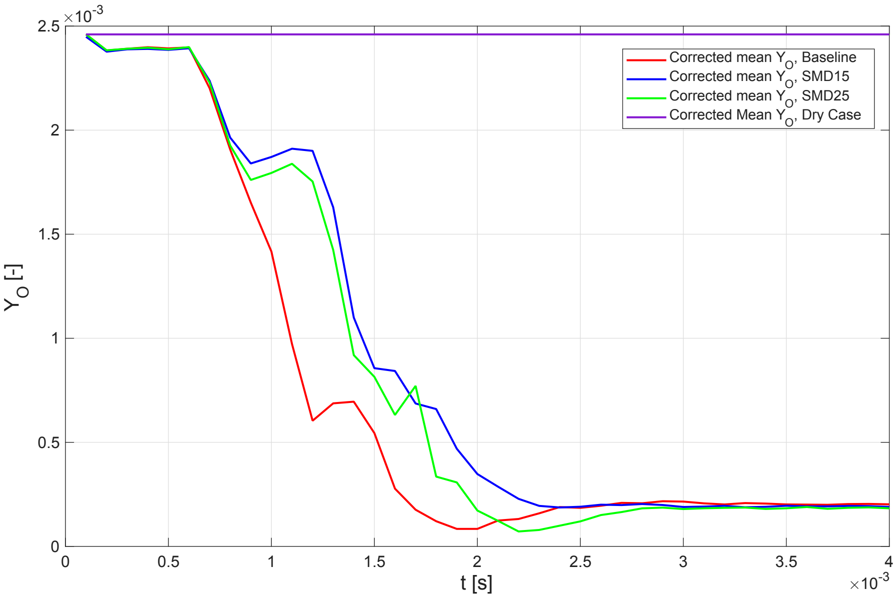

Figure 5.36: Mean $\mathrm{Y_O}$ as a function of time. Effect of SMD increment (see Table 4.4 and Table 4.5) and corrected to account for dilution.

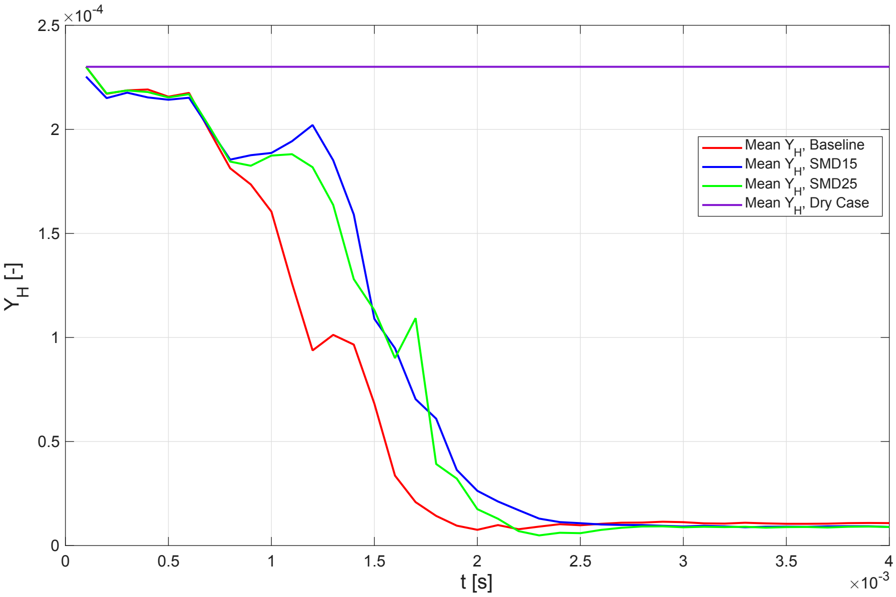

Figure 5.37: Mean $\mathrm{Y_H}$ as a function of time. Effect of SMD increment (see Table 4.4 and Table 4.5).

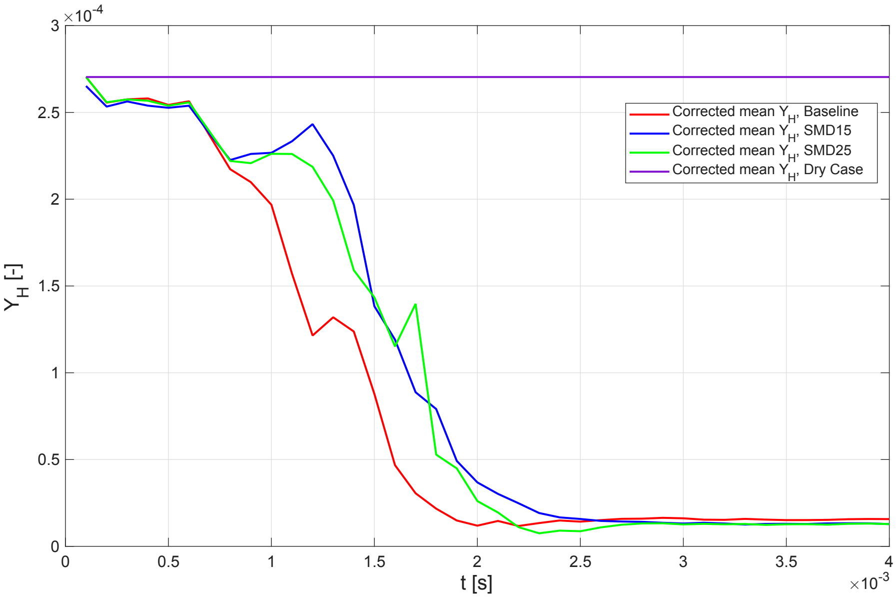

Figure 5.38: Mean $\mathrm{Y_H}$ as a function of time. Effect of SMD increment (see Table 4.4 and Table 4.5) and corrected to account for dilution.

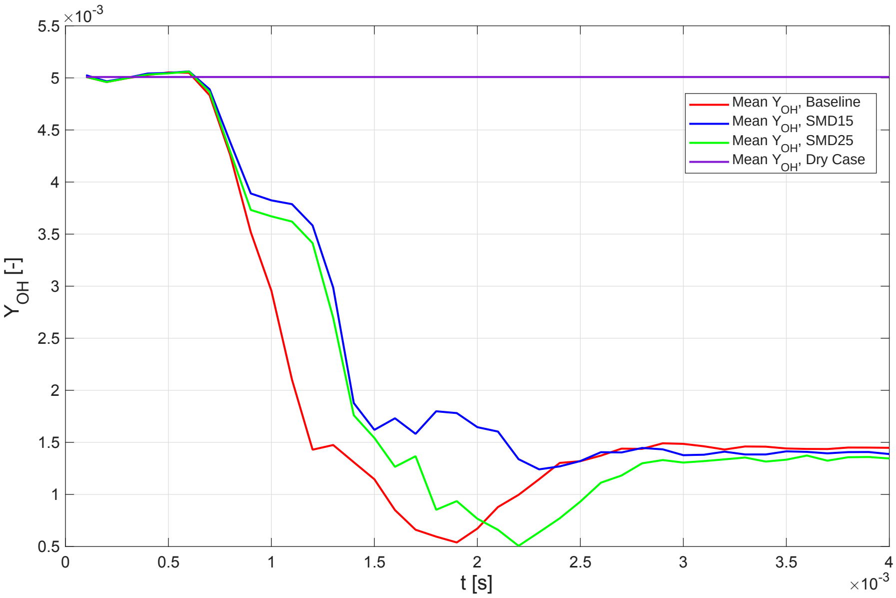

Figure 5.39: Mean $\mathrm{Y_{OH}}$ as a function of time. Effect of SMD increment (see Table 4.4 and Table 4.5).

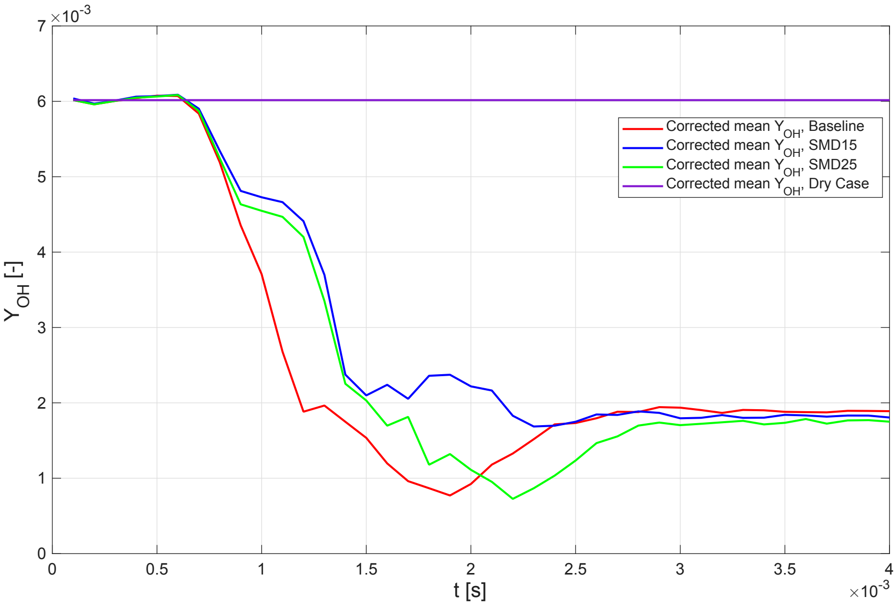

Figure 5.40: Mean $\mathrm{Y_{OH}}$ as a function of time. Effect of SMD increment (see Table 4.4 and Table 4.5) and corrected to account for dilution.

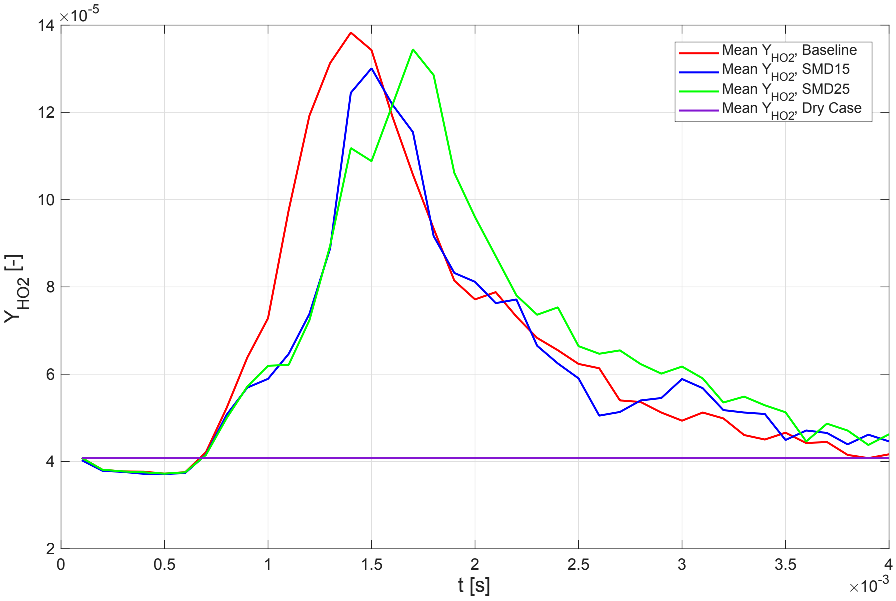

Figure 5.41: Mean $\mathrm{Y_{HO_2}}$ as a function of time. Effect of SMD increment (see Table 4.4 and Table 4.5).

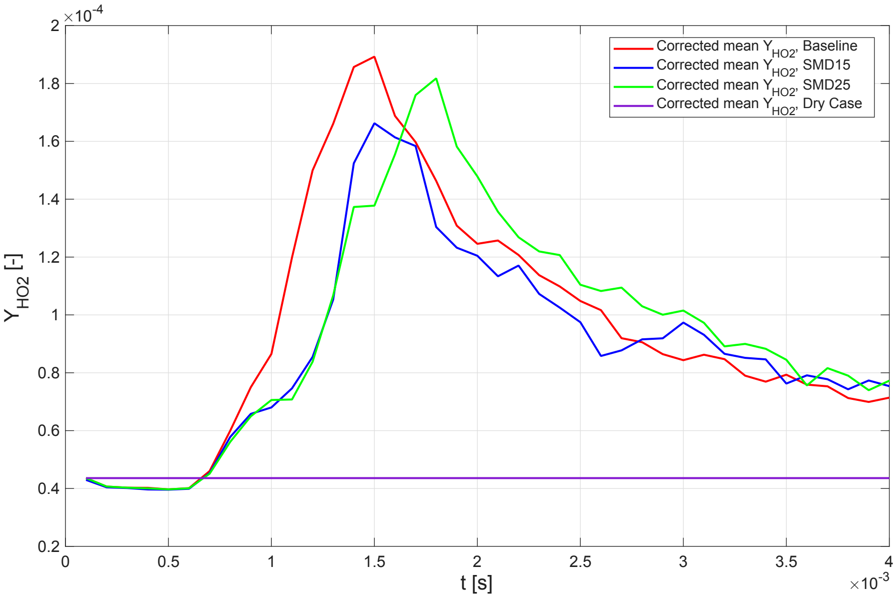

Figure 5.42: Mean $\mathrm{Y}_{\mathrm{HO}_2}$ as a function of time. Effect of SMD increment (see Table 4.4 and Table 4.5) and corrected to account for dilution.

5.3.2. Temperature and Hydrogen Rate of Production

Figure 5.43 shows the variation of hydrogen rate of production at $t = 4$ ms for the baseline, SMD15, and SMD25 cases. As it can be observed, no significant changes can be found in hydrogen rate of production once a quasi-steady state is reached, but increasing SMD having slightly lower reactivity, likely due to the higher droplet volume.

On the other hand, Figure 5.44 shows that at $t = 4$ ms increasing SMD is correlated to slightly lower average temperatures in the flame zone, with case SMD25 having a mean flame temperature 18K lower to the baseline case, and SMD15 presenting a mean temperature 8K lower. In general, the results presented in these figures corroborate what would be expected from the analysis done in subsection 5.3.1: a small decrease in the absolute value of the hydrogen rate of production as the diameter of the droplets increases and a small reduction in the mean temperature due to the fact that larger droplets require more energy to evaporate and thus are more effective.

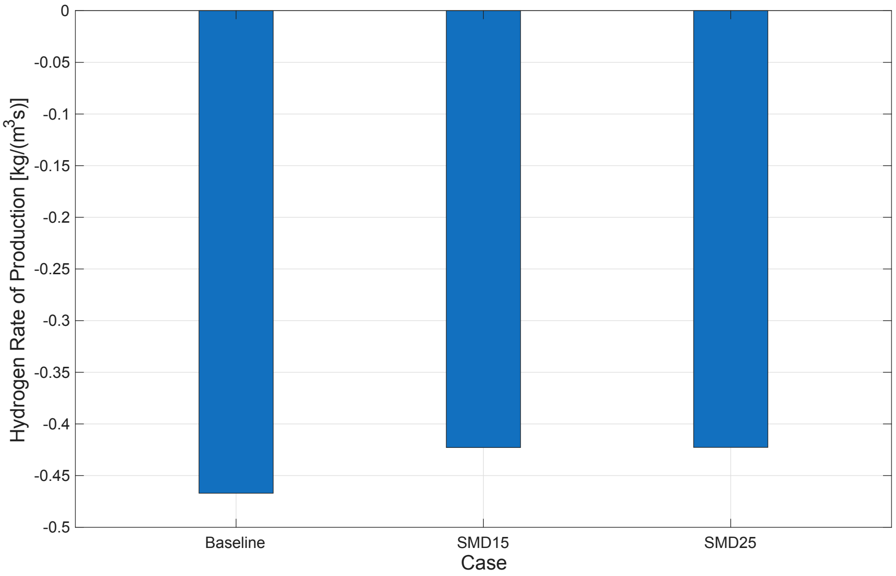

Figure 5.43: Mean hydrogen rate of production on the flame region: SMD increment impact.

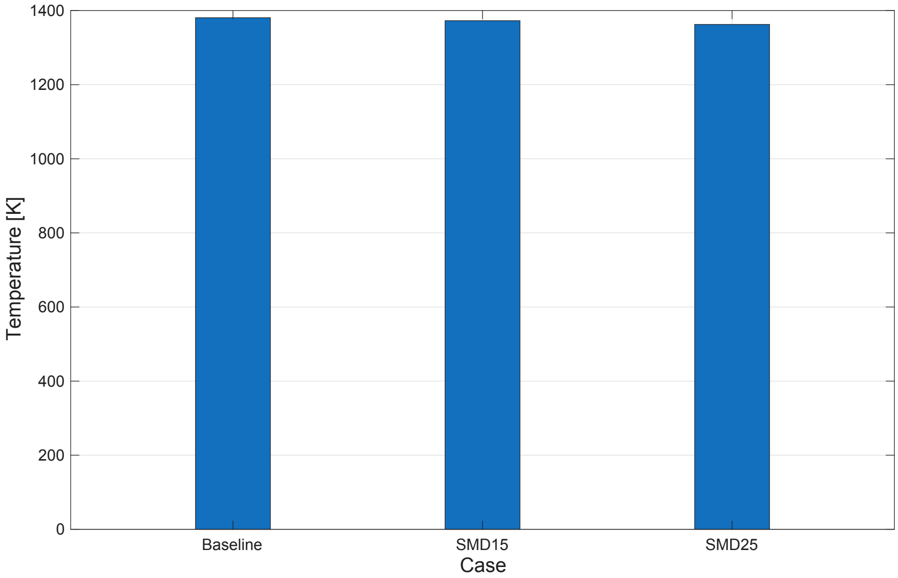

Figure 5.44: Mean Temperature on the flame region: SMD increment impact.

Figure 5.45 provides information regarding the temperature value for each cell in the domain in function of the molecular hydrogen progress variable. As it can be observed, lower temperatures at lower values for $c(\text{H}_2)$ are verified for both SMD15 and SMD25 compared to the baseline case. Moreover, it is easily observable that the temperature peaks are slightly higher at lower values of SMD.

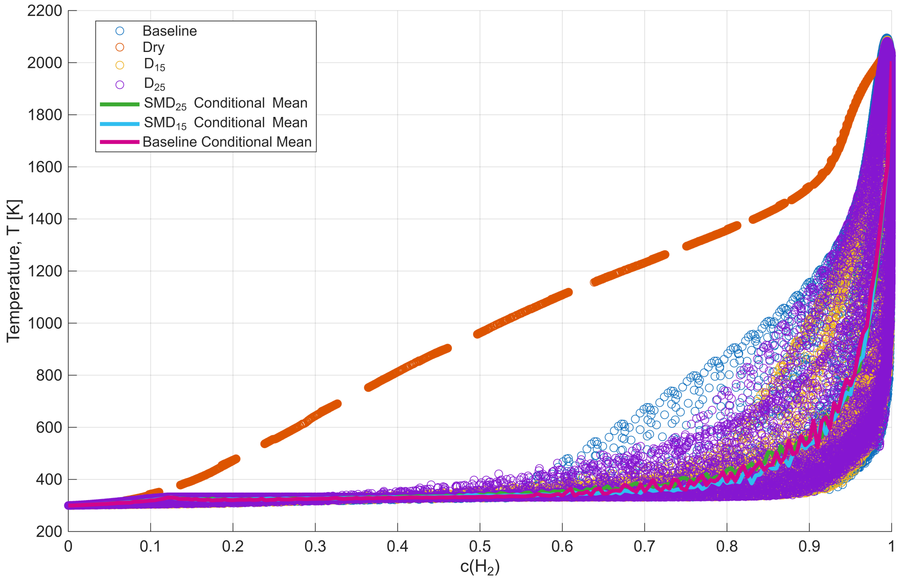

Figure 5.45: Temperature distribution at t = 4ms: SMD increment impact.

5.3.3. **NNH** Emission Results

No significant changes are observed when discussing NNH emissions after increasing SMD. In Figure 5.46, shows vaules of f_I^{NNH} after 4 ms of simulation time. As it can a reduction similar in NNH is found for all three cases, with SMD25 verifying the largest reduction in NNH presence at 97.9% of the original dry case and the baseline case showing the smallest reduction at 97.4% of the original dry case. Accounting for dilution translates into a reduction of 97.1% for the baseline case, 97.5% for SMD15 , and 97.6% for SMD25, indicating what was already verified for the baseline case: while dilution plays a part in reducing these species mass fractions in the domain, the vast majority of the reduction is due to the chemical and physical effects.

Figure 5.47 and Figure 5.48 confirm this observations, by showing the Y_{NNH} cell value distributed in function of $c(\mathrm{H}_2)$, with and without the dilution effect. As it can be observed, a small decrease in Y_{NNH} is observed at lower $c(\mathrm{H}_2)$ values, with this reduction being specifically noticeable for SMD15. Moreover, the peaks of Y_{NNH} also are slightly lower for the cases with increased SMD compared to the baseline, specifically SMD15. Nevertheless, the conditional means plotted indicate that the SMD25 case shows a lower average value for Y_{NNH} specially at higher progress variable values, thus being slightly more effective at suppressing NNH.

These results are in line with what would be expected from the results presented in subsection 5.3.1: the NNH formation in the NNH mechanism start with the recombination of molecular nitrogen with H, the heavy suppression of H radicals presented in Figure 5.37 and Figure 5.38 leads to the formation of NNH being heavily reduced. Moreover, the reduction in NNH observed combined with the reduction in O radicals observed in Figure 5.35 and Figure 5.36 should heavily reduce the formation of NO from the NNH mechanism as is described in section 2.1. The small increments in radical reductions observed as the droplet diameter is increased results in the reductions observed in Figure 5.46.

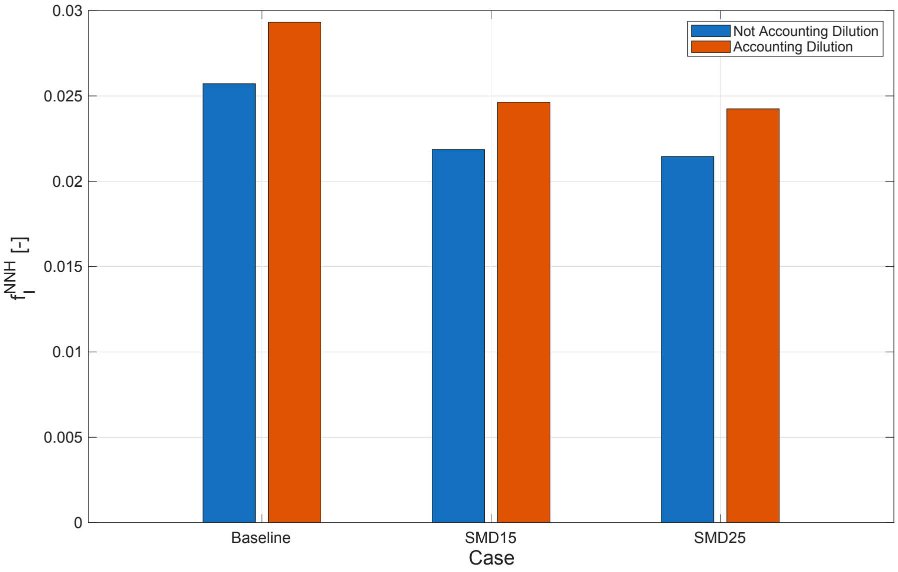

Figure 5.46: f_I^{NNH} at $t = 4$ ms. Effect of SMD variation (see Table 4.4 and Table 4.5).

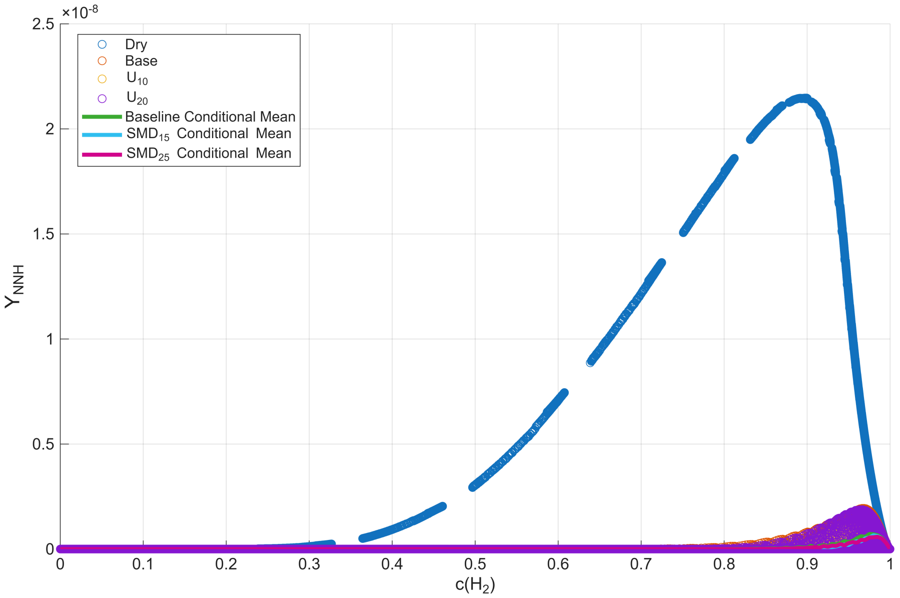

(a) NNH mass fraction distribution in function of the hydrogen progress variable at t = 4ms.

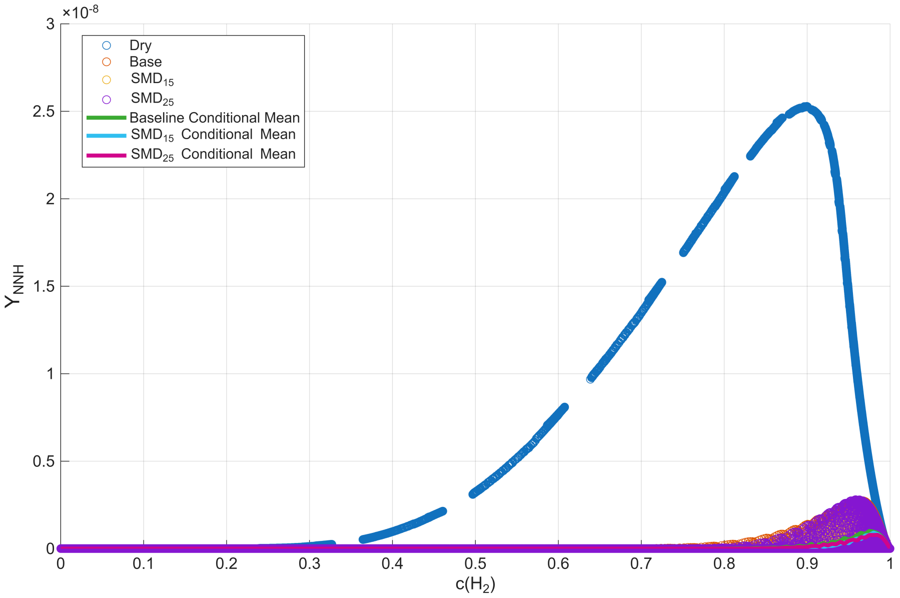

(b) NNH mass fraction distribution in function of the hydrogen progress variable at t = 4ms, accounting dilution.

Figure 5.47: NNH mass fraction distribution in function of the hydrogen progress variable at t = 4ms: SMD increment impact.

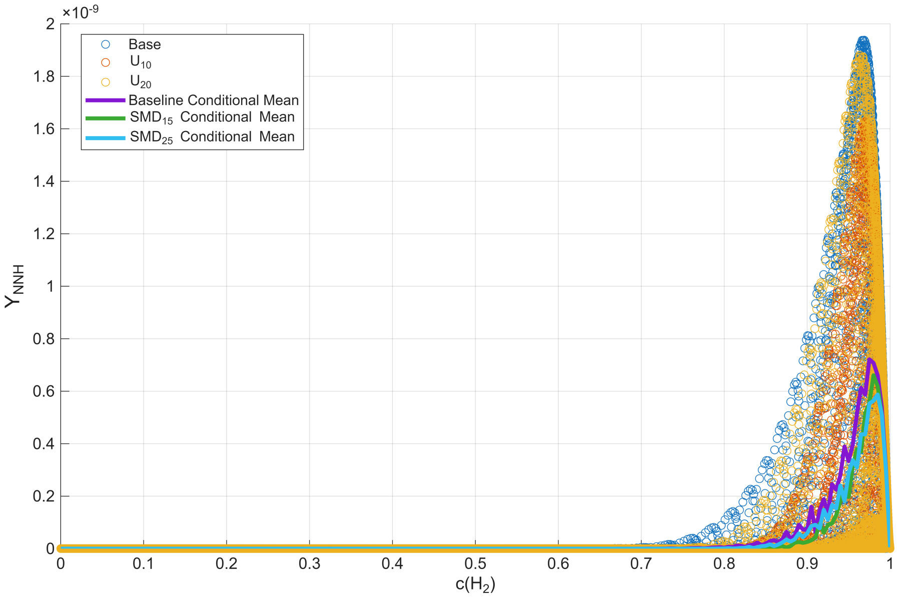

(a) NNH mass fraction distribution in function of the hydrogen progress variable at t = 4ms, without dry case.

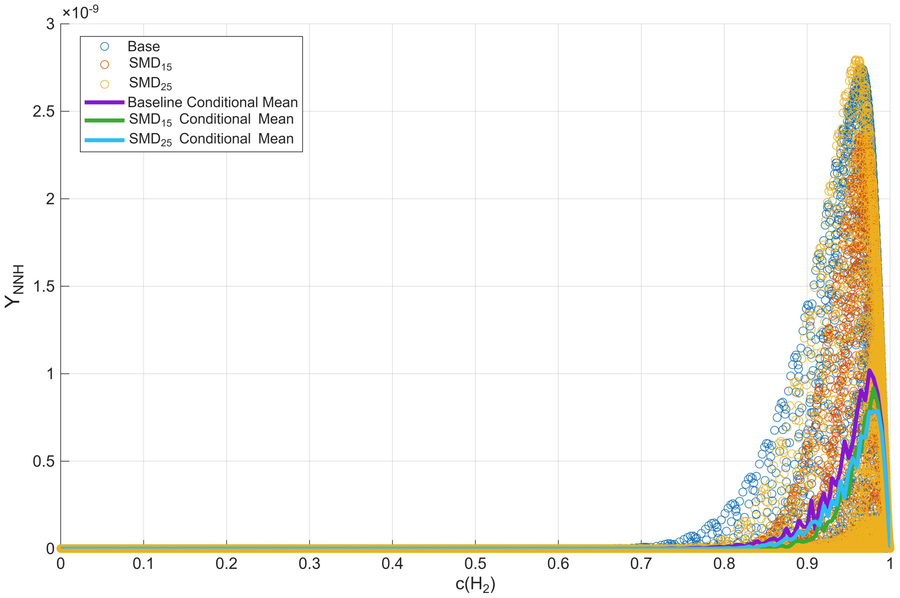

(b) NNH mass fraction distribution in function of the hydrogen progress variable at t = 4ms without dry case & accounting dilution.

Figure 5.48: NNH mass fraction distribution in function of the hydrogen progress variable at t = 4ms: SMD increment impact and without dry case.

5.3.4. N_2O Emission Results

Observing Figure 5.49 it is possible to observe an increase in $f_I^{\mathrm{N_2O}}$ as the SMD is incremented between cases. This translates into a reduction of N_2O presence in the domain with increasing SMD. For SMD25 case, at $t = 4$ ms, the value for $f_I^{\mathrm{N_2O}}$ is approximately 0.355, for SMD15 it is approximately 0.359, numbers that suggest a decrease of $Y_{\mathrm{N_2O}}$ when compared to the baseline value of 0.378. Accounting for dilution, the values for $f_I^{\mathrm{N_2O}}$ become, approximately, 0.437 for the baseline case, 0.413 for SMD15, and 0.408 for SMD25, once again demonstrating that the reduction observed is majority caused by the chemical-physical effects from the injection of water, rather then its dilution effect. From Figure 5.50a and Figure 5.50b it is observable that this reduction mostly occurs at higher values of $c(\mathrm{H_2})$ (between $c(\mathrm{H_2}) = 0.8$ and $c(\mathrm{H_2}) = 1.0$, indicating that this reduction is occurring primarily right before the flame front and after it closer to the products region, possibly due to the changes in radical concentrations previously found, specially the O radical changes since this radical is essential for the formation of N_2O.

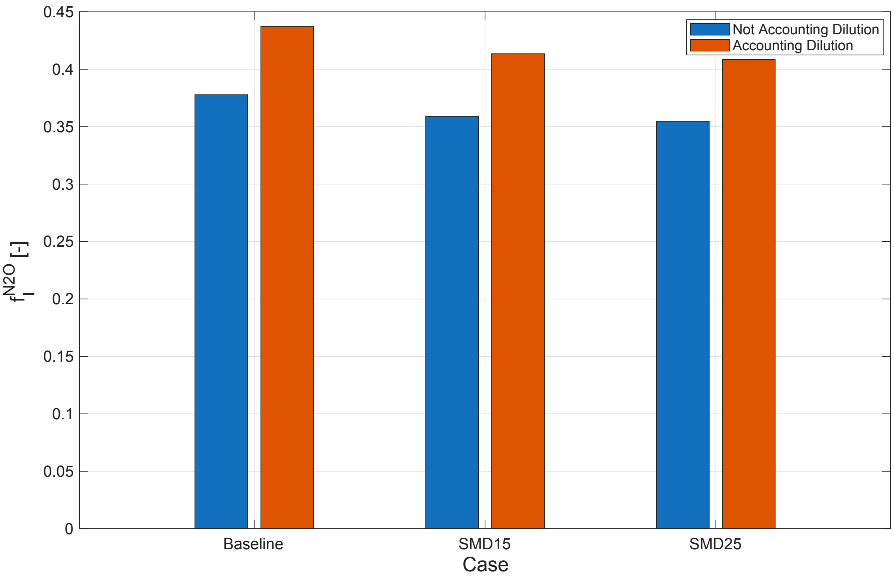

Figure 5.49: $f_I^{\mathrm{N_2O}}$ at $t = 4$ ms. Effect of SMD variation (see Table 4.4 and Table 4.5).

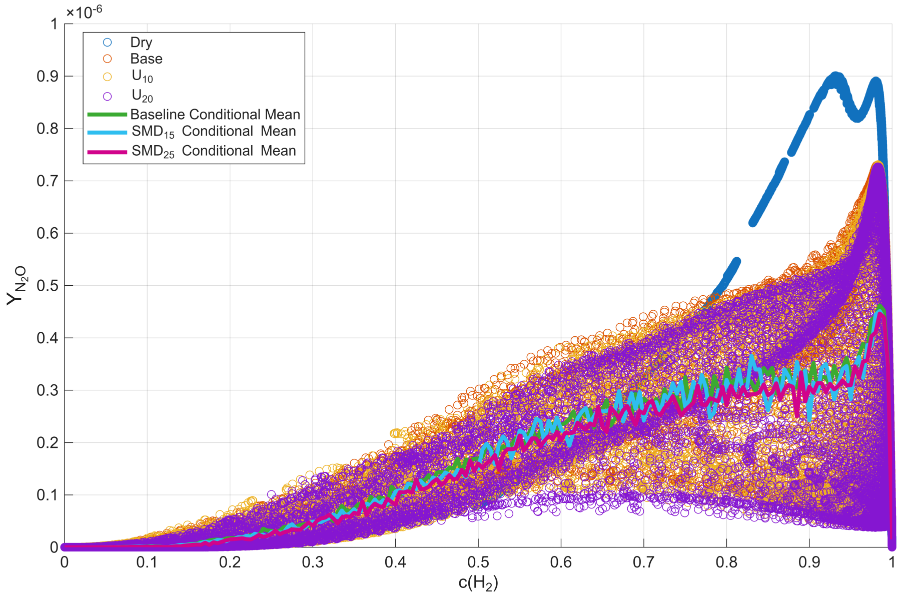

(a) N_2O mass fraction distribution in function of the hydrogen progress variable at t = 4ms.

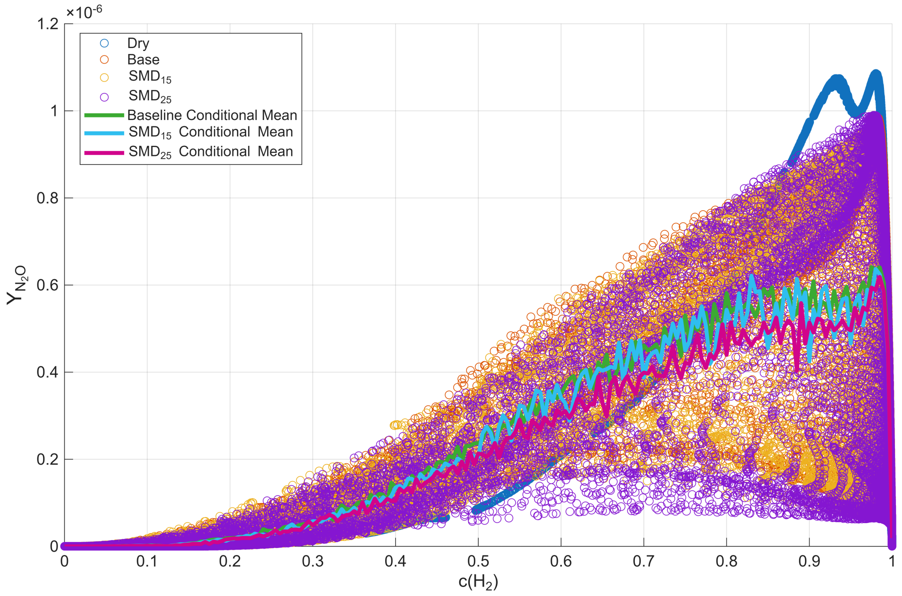

(b) N_2O mass fraction distribution in function of the hydrogen progress variable at t = 4ms, accounting dilution.

Figure 5.50: N_2O mass fraction distribution in function of the hydrogen progress variable at t = 4ms: SMD increment impact.

5.3.5. NO Emission Results

Regarding the changes observed in NO emissions, it was observed that increasing SMD yield positive reduction on the presence of NO in the domain. As it can be observed in Figure 5.51, when $t = 4$ ms, the value of f_I^{NO} decreases to 0.167 for SMD25 and 0.215 for SMD15 from the baseline value of 0.218. Accounting for dilution, these values become, approximately, 0.196 for SMD25 and 0.254 for SMD15 compared to the baseline value of 0.258.

Expanding on this information, Figure 5.52 shows how the value for Y_{NO} is distributed against the molecular hydrogen. As it can be seen, for SMD15 a reduction in NO presence near the product region, likely corresponding to Thermal NOx, is verified, however a small increase in NO around the regions of smaller $c(\mathrm{H}_2)$ is also observed and brings the overall emissions close to the ones observed for the baseline case. Regarding SMD25, a bigger reduction for late progress variable values Y_{NO} is observed and in this case it is also coupled with a reduction in NO for lower values of c.

The reductions seen in late domain NO likely correspond to reductions in thermal NOx formation. These changes are likely caused by the small reduction in temperature observed in Figure 5.44. Since the average diameter of the droplets increases, their individual mass and volume also increase which translates into more energy being necessary to evaporate them, resulting in a lower flame temperature. Furthermore, the reductions observed in O, H, and OH mass fractions, as well as the increase of the less reactive HO_2 help mitigate Zeldovich NOx production due to changes in the chemical reactions pathways, as described in section 2.1 and subsection 5.1.5. This results concur with what Banerjee et al. [13] observed: as long as the droplets are small enough to guarantee their evaporation, higher droplet mean diameters are associated with bigger reductions in NOx production.

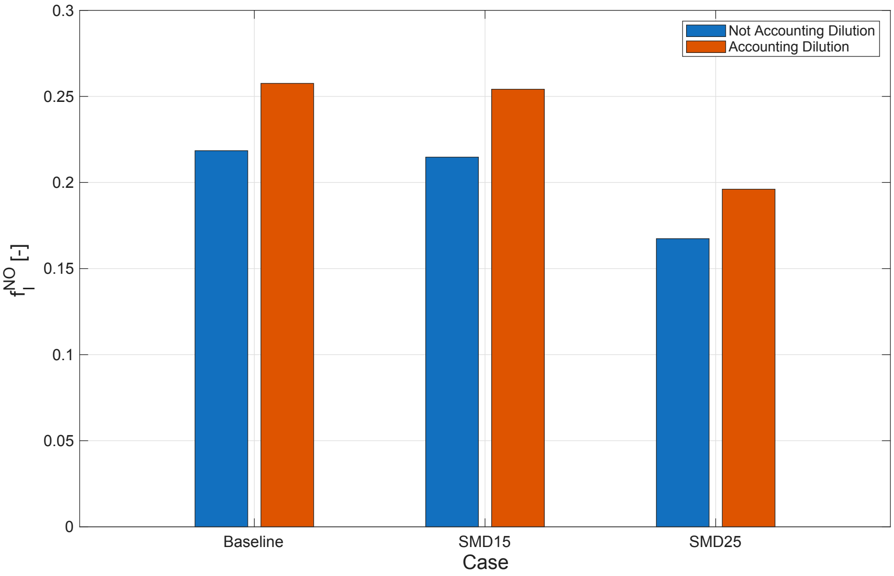

Figure 5.51: f_I^{NO} at $t = 4$ ms. Effect of SMD variation (see Table 4.4 and Table 4.5).

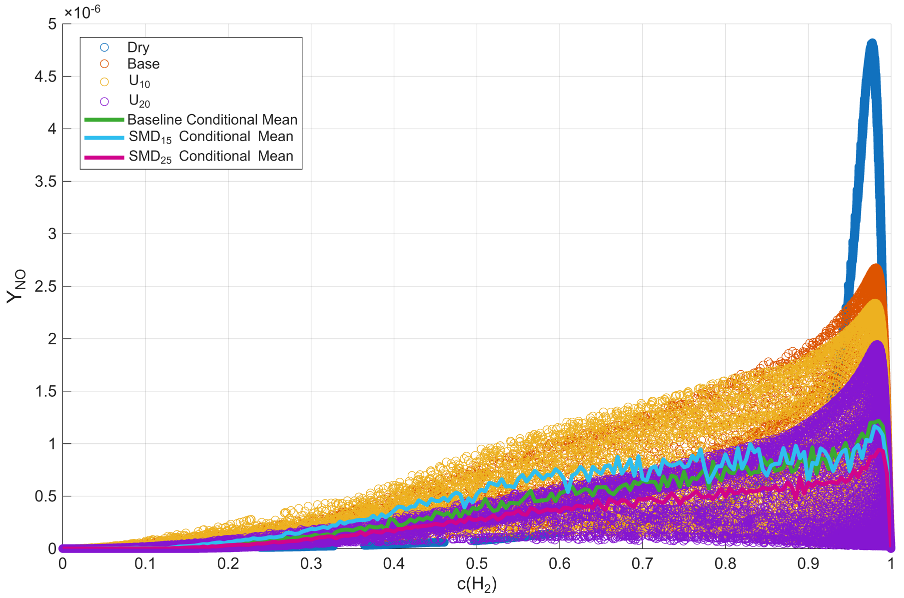

(a) NO mass fraction distribution in function of the hydrogen progress variable at t = 4ms.

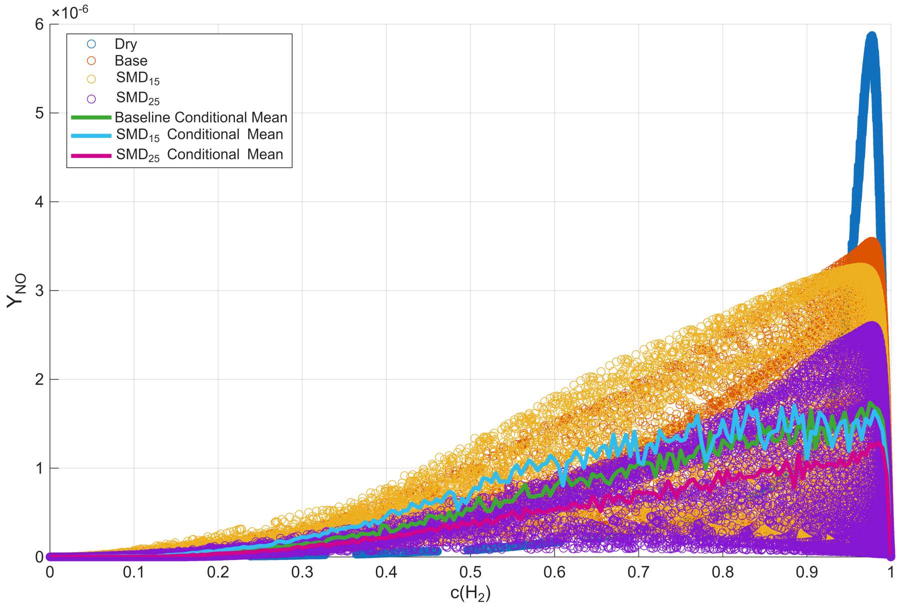

(b) NO mass fraction distribution in function of the hydrogen progress variable at t = 4ms, accounting dilution.

Figure 5.52: NO mass fraction distribution in function of the hydrogen progress variable at t = 4ms: SMD increment impact.

5.3.6. Observations on Emissions Results

In this section the results associated with increasing SMD were analyzed. As it was observed, in general, as SMD is increased the presence of N_2O and NO are reduced due to the changes in radical concentrations discussed in subsection 5.3.1 and the temperature changes seen in Figure 5.44 and Figure 5.45. The observed changes stem from the higher diameter of the average droplet increasing the volume and mass of the droplets requiring more energy to evaporate. Contrary to the trend observed in N_2O and NO, while a decrease in NNH production when compared to the baseline case, this decrease is more noticeable for the case SMD15 than for the case SMD25. This is somewhat unexpected since the sharper reduction in H radicals and lower flame temperature in case SMD25 should result in less Y_{NNH} in this case than in case SMD15; however the higher values of Y_{NNH} present in SMD25 compared against SMD15 are likely caused by the higher temperatures observed in this case before the flame front, as seen in Figure 5.45.

Overall, the attained results are in agreement with what was observed by Banerjee et al. [13] and Sharkey and Zare [38]: as long as the droplet size is small enough to guarantee it's evaporation, the larger the mean droplet diameter, the higher the emission reductions observed are.

5.4. Effect of Increasing Flame Strain With Water Injection: Results and Observations

In this section, the effects of water injection are compared in two flames with different strain rates. The intention is to observe whether increasing the strain in conjunction with water injection results in a greater reduction in emissions and radical concentration by coupling the benefits discussed in section 2.2 and section 2.3. For this purpose, the baseline case analyzed in section 5.1 will be compared with the simulation setup S2, whose key operating conditions and parameters are exposed in Table 4.4.

5.4.1. Radical Concentrations on the Flame Region

Figure 5.53, Figure 5.55, Figure 5.57, and Figure 5.59 show the time variation of the mass fraction of the radicals O, H, OH, and HO_2 for the baseline case and the S2 case. In Figure 5.53 it can be observed that for the case with higher strain, the mass fraction of the oxygen radical starts higher than the baseline case. Moreover, it is observable that by the end of the simulated time Y_{O} is smaller in the case with a strain rate of $8000\ \mathrm{s}^{-1}$ than it is for the baseline case, with a reduction in Y_{O} of 98.6% being verified for case S2 over the analyzed time period. A similar trend is seen in Figure 5.55, where initially the mass fraction of H radical is higher in case S2, but after 4 ms the mass fraction reduces by 99.7%, compared to a flame without water injection and strain rate of $8000\ \mathrm{s}^{-1}$. It is observable from Figure 5.57 that before water is injected the mass fraction of OH is highest on the baseline case, contrary to the previously discussed species, and after the simulated time is ends this holds true; however, while the reduction in OH radicals is of 71% as discussed in section 5.1, the drop in Y_{OH} is even more accentuated in case S2, where a reduction of 88.5% in this species mass fraction is seen. In figure Figure 5.59 a trend akin to the cases expressed in Figure 5.53 and Figure 5.55 is observed: at the beginning, the mass fraction of HO_2 is more accentuated in the case with higher strain, but after 4 ms the presence of this species is greatly reduce. This contrasts with the baseline case where after the simulated time the mass fraction of HO_2 is slightly higher than the original. Nevertheless, in both baseline and S2 a peak in this species mass fraction is verified before dropping.

Figure 5.54, Figure 5.56, Figure 5.58, and Figure 5.60 show the same time variation of the mass fraction of the O, H, OH, and HO_2 radicals, but corrected to account for the dilution effect caused by the addition of water into the system. As it can be observed, the behavior is similar the cases where dilution is unaccounted for, but the changes in these species mass fractions are less pronounced. These figures allows the quantification of how much of these reductions are cause by chemical and physical changes due to the water injection and how much of them are simply due to the extra water injected. As it can be inferred, the majority of the reductions observed are due to the chemical and physical effects on radical formation pathways. The reasons for these changes are the same as discussed for the baseline case in subsection 5.1.1, overall the water injection provokes changes in the chemical pathways and reduces temperature and hydrogen reactivity that lead to a reduction in these intermediate species on the flame region. The lower quantities of OH radicals in the initial timestep for case S2 are in line with what Porcarelli, Kruljević, and Langella [14] and Porcarelli and Langella [42] as it was observed a sharp decrease in this radical's mass fraction with increasing strain. Moreover, the same studies verified local peaks of O and H radicals with increasing strain, which help justify the initial values for this species mass fractions before water is injected. Finally, it is interesting to note is that for the two cases a similar water loading was introduced and the flame with the higher strained responded to this injection faster and with a higher degree of reduction than the one observed in the baseline case. This seems to suggest that coupling increasing flame strain rate with water injection results in a greater reduction of the presence of these intermediate chemical species than each of these methods individually.

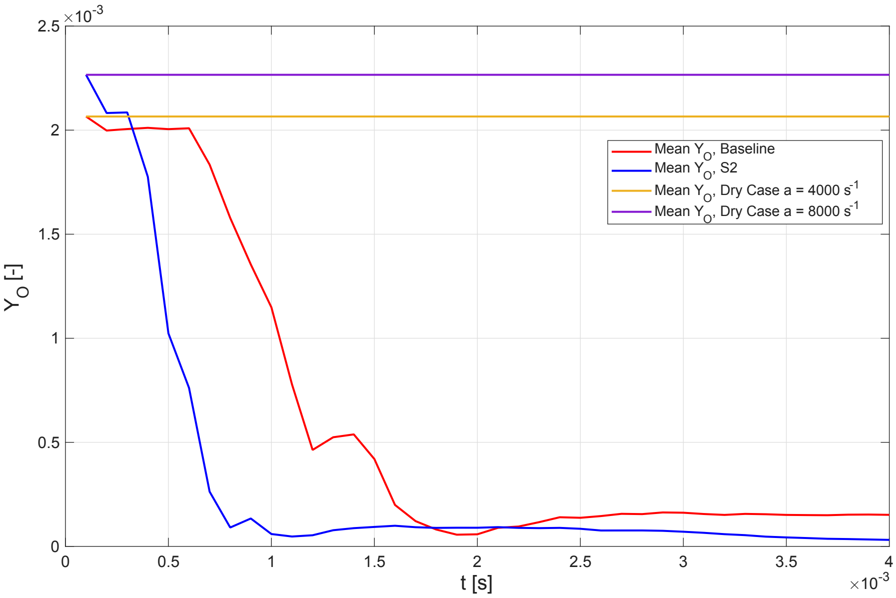

Figure 5.53: Mean Y_O as a function of time. Effect of increasing strain with water injection (see Table 4.4 and Table 4.5).

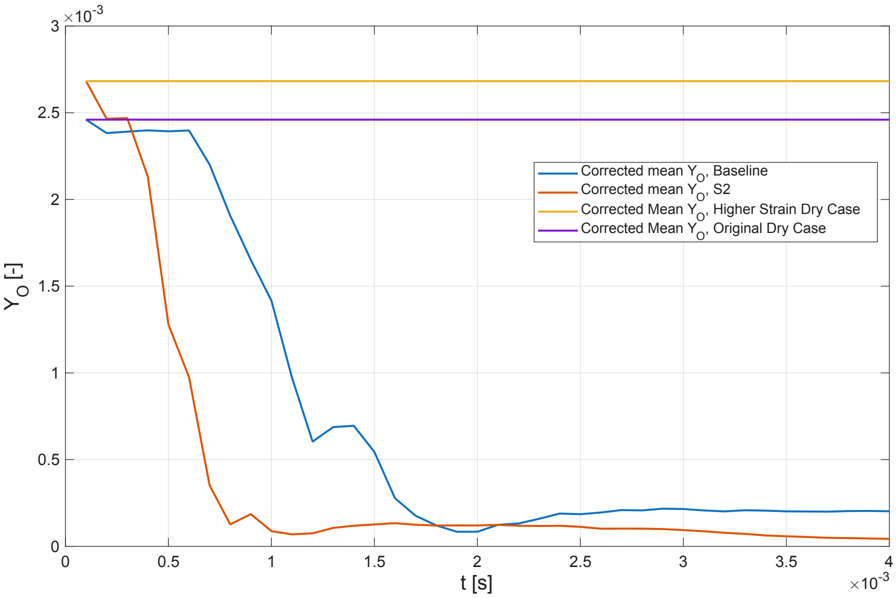

Figure 5.54: Mean Y_O as a function of time. Effect of increasing strain with water injection (see Table 4.4 and Table 4.5) and correcting to account for dilution.

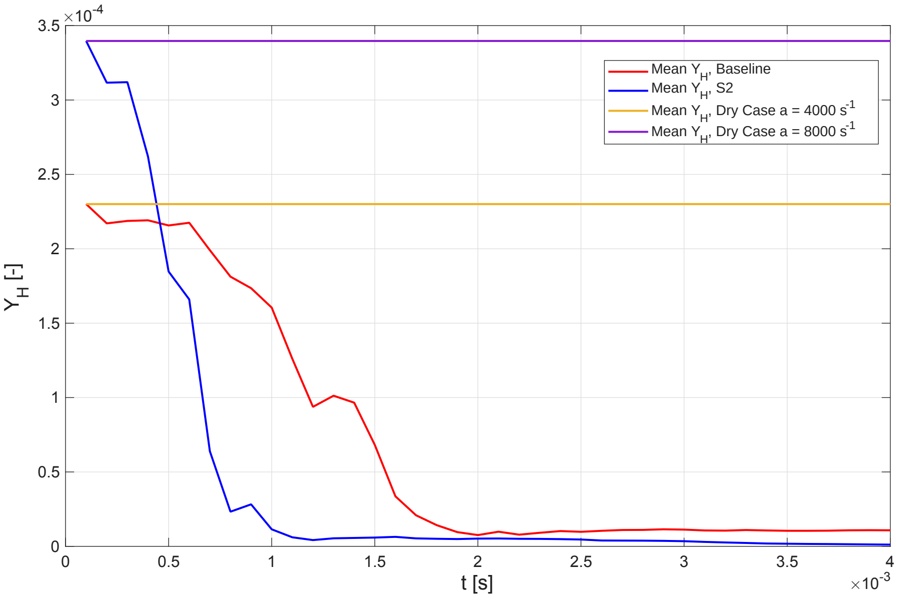

Figure 5.55: Mean Y_{H} as a function of time. Effect of increasing strain with water injection (see Table 4.4 and Table 4.5).

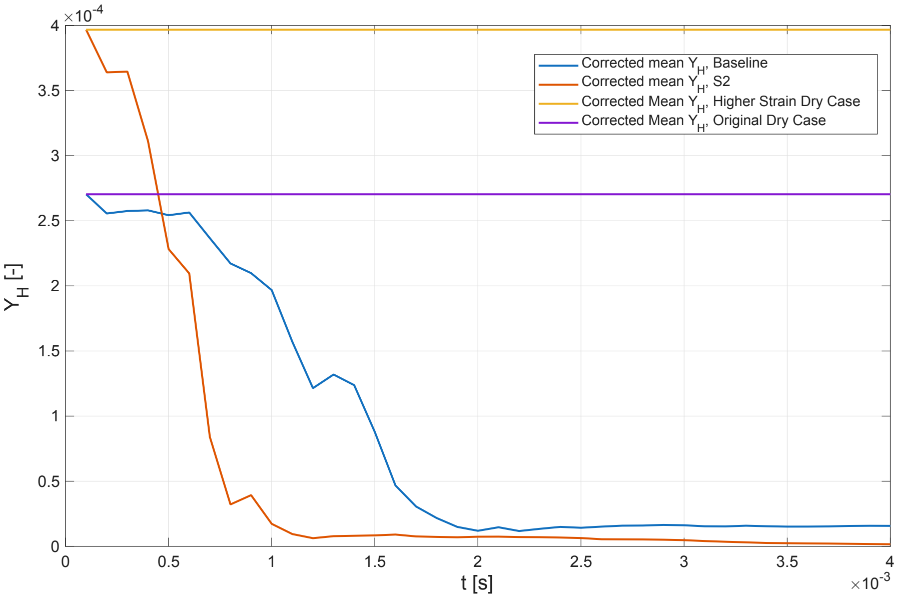

Figure 5.56: Mean Y_{H} as a function of time. Effect of increasing strain with water injection (see Table 4.4 and Table 4.5) and correcting to account for dilution.

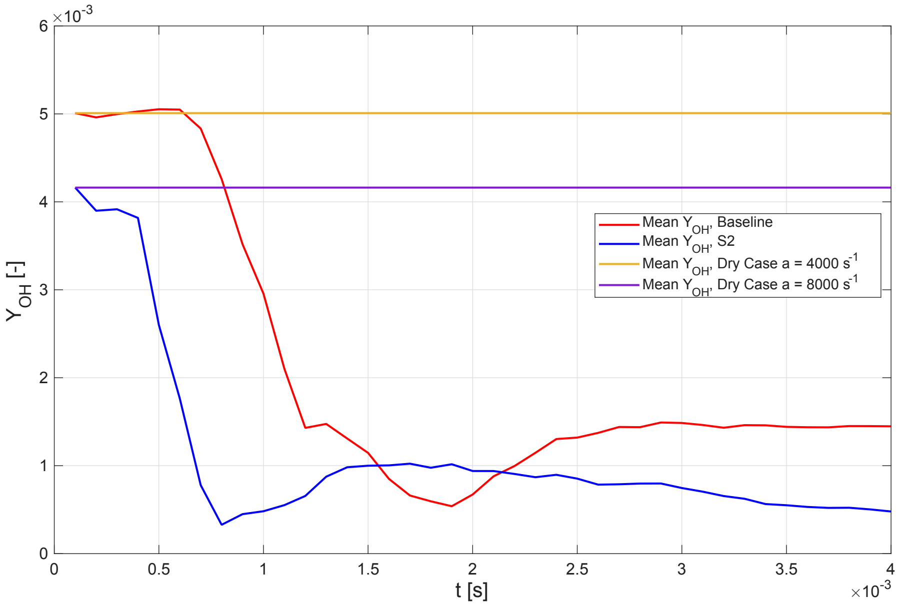

Figure 5.57: Mean Y_{OH} as a function of time. Effect of increasing strain with water injection (see Table 4.4 and Table 4.5).

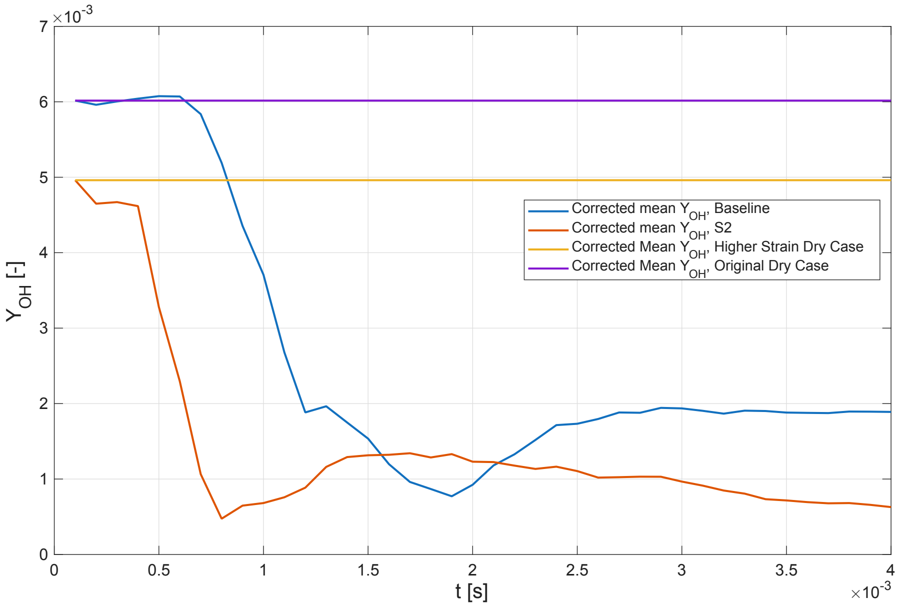

Figure 5.58: Mean Y_{OH} as a function of time. Effect of increasing strain with water injection (see Table 4.4 and Table 4.5) and correcting to account for dilution.

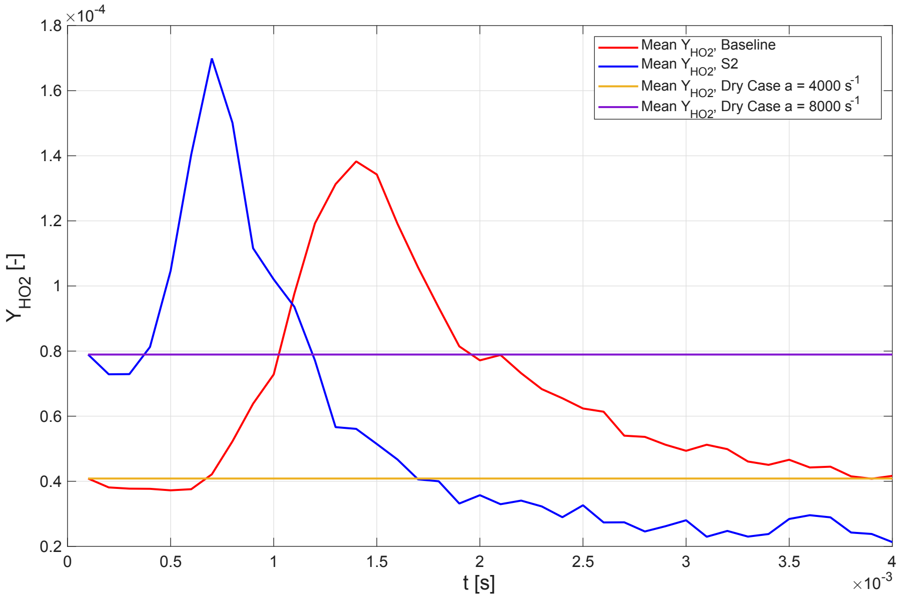

Figure 5.59: Mean Y_{HO_2} as a function of time. Effect of increasing strain with water injection (see Table 4.4 and Table 4.5).

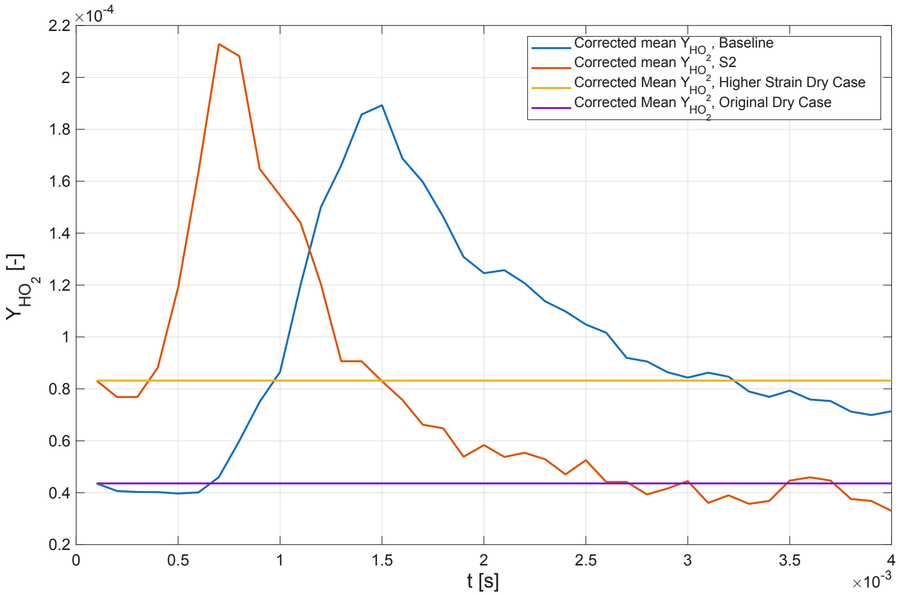

Figure 5.60: Mean Y_{HO_2} as a function of time. Effect of increasing strain with water injection (see Table 4.4 and Table 4.5) and correcting to account for dilution.

5.4.2. Temperature and Hydrogen Rate of Production

Figure 5.61 shows the values of the hydrogen rate of production at $t = 0$ and at $t = 4$ ms for the baseline and S2 cases. It is observable that the initial timestep, the rate of production is more negative for the S2 setup, this indicates a higher hydrogen consumption for the case with higher strain. This is in line with what is observed in literature, specifically [14] and [42], where higher reactivities are observed has hydrogen flame strain is incremented. As water is injected into the domain, a shaper reduction in reactivity is verified for the case S2, when compared to the baseline case: after 4 ms hydrogen rate of consumption decreased 99.5% in case S2 and 96.8% in the baseline. This is similar to what was observed in the previous section, the effects of water injection are more pronounced in the case with a more strained flame.

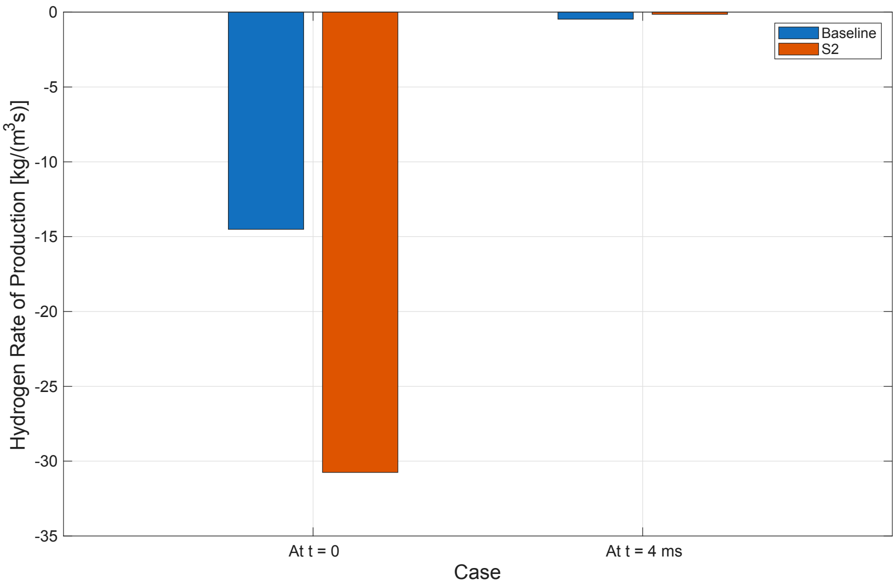

Figure 5.61: Mean Hydrogen Rate of Production 10^{th} percentile of hydrogen rate of production. Effect of increasing strain with water injection: baseline case (blue) and case S2 (orange) (see Table 4.4 and Table 4.5)

Figure 5.62 provides the variation of mean temperature for the region on the 10^{th} percentile of temperature at $t = 0$ and at $t = 4$ ms for the baseline case and the S2 case. It can be observed that in the initial time step the mean temperature is more than 200 K lower in the case with higher strain. This goes against the trend that is found in [65] where strained flames rich in hydrogen are seen to present higher flame temperature at higher strain level; however, the aforementioned paper does not consider flames with higher strain rates than 500 s^{-1}, and as such it can not be verified that this trend would continue for values of strain as high as the ones being analyzed here.

After 4 ms of simulation time, a reduction in mean temperature of 356 K is observed for the baseline case, while S2 presents a reduction of 346 K. In relative terms, this translates to a 22.8% reduction in mean temperature for case S2 and a reduction of 20.5% for the baseline case. As such, this observation corroborates what was previously stated: for similar water loading conditions, the effects of water injection are more noticeable in the case with higher flame strain rate.

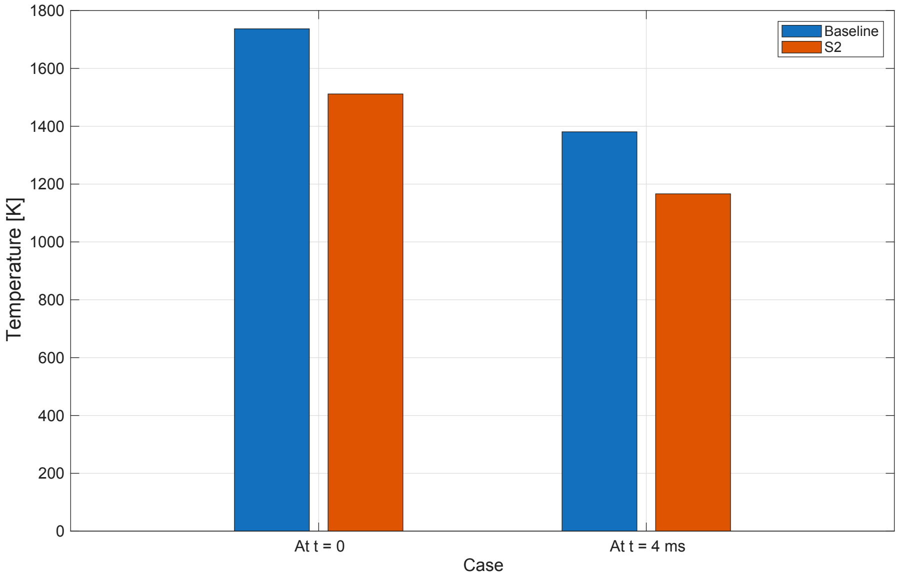

Figure 5.62: Mean Temperature 10^{th} percentile of temperature region. Effect of increasing strain with water injection: baseline case (blue) and case S2 (orange) (see Table 4.4 and Table 4.5)

Figure 5.63 shows the temperature distribution at $t = 4$ ms in function of $c(\text{H}_2)$ (in Figure 5.63). As it can be observed, after 4 ms of continuous water injection and for these two cases with similar water loading values, case S2 shows a lower peak temperature and lower mean values of temperature at all progress variable values. Moreover, it is also possible to observe that the average cell temperature presents a higher variation for the same values of c in the baseline case. Finally, it is possible to observe that case S2 has its reaction zone at slightly higher values of $c(\text{H}_2)$ suggesting that not only is the reaction occurring slightly closer to the products zone.

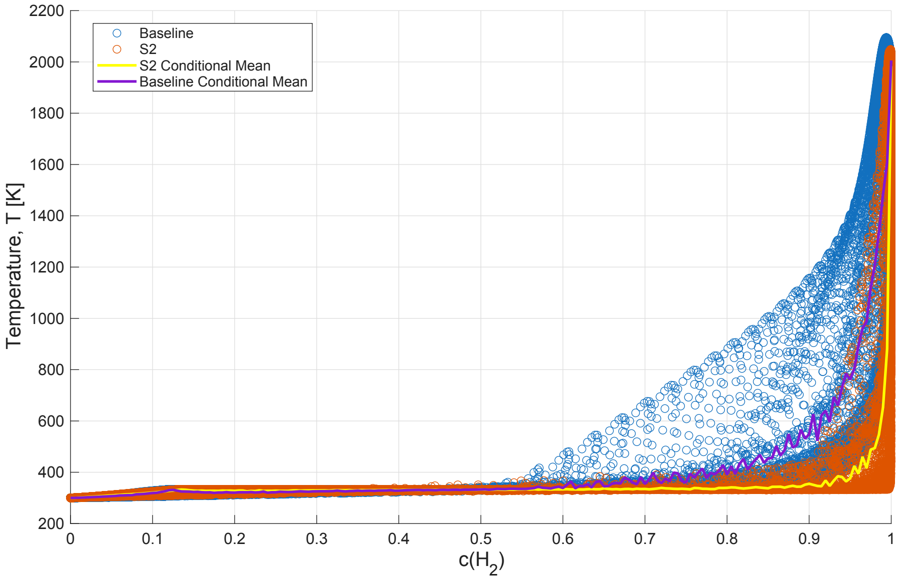

Figure 5.63: Temperature distribution at t = 4ms in function of $c(\text{H}_2)$: Two Different Strains with Water Injection.

5.4.3. Effect on **NOx** Emissions

Figure 5.64 and Figure 5.65 provide the variation of f_I^{NNH} across 4 ms for the baseline case and S2. For Figure 5.64 f_I^{NNH} for the S2 case is calculated using a dry case with a strain rate equal to 8000 s^{-1} and according to the expression defined in Eq.(4.24), for Figure 5.65 f_I^{NNH} is calculated using the original dry case I_{NNH}. This is done in order to isolate the impact caused by water injection and the impact of the increased strain rate on this specie's concentration. As it can be observed in Figure 5.64, a 99.55% drop in f_I^{NNH} is verified for case S2 exclusively due to the injection of water, i.e, compared to a case without water injection and a strain rate, $a = 8000$ s^{-1}, f_I^{NNH} is reduced by 99.55%. Moreover, it is observable in Figure 5.65 that coupling an increase in strain rate with water injection results in an overall decrease in f_I^{NNH} of approximately 99.65%. The initial reduction in I_{NNH} exclusively due to increasing the strain rate from 4000 s^{-1} to 8000 s^{-1} is of approximately 21.7%. As such, it is possible to conclude that the vast majority of NNH reduction observed being due to the effects of water injection, which were discussed in detail in subsection 5.1.3.

In Figure 5.66 the values for f_I^{NNH} are presented at $t = 4$ ms, with and without account for dilution. It can be observed, the dilution effect accounts for a minor percentage of the emissions reduction observed, similar to what was observed in the cases where injection velocity and SMD were changed.

Overall, it can be observed that the emission reduction caused by injecting water is enhanced by the higher strain and coupled with the reduction in emissions caused by the higher strain, this results in an even more significant suppression of NNH emissions.

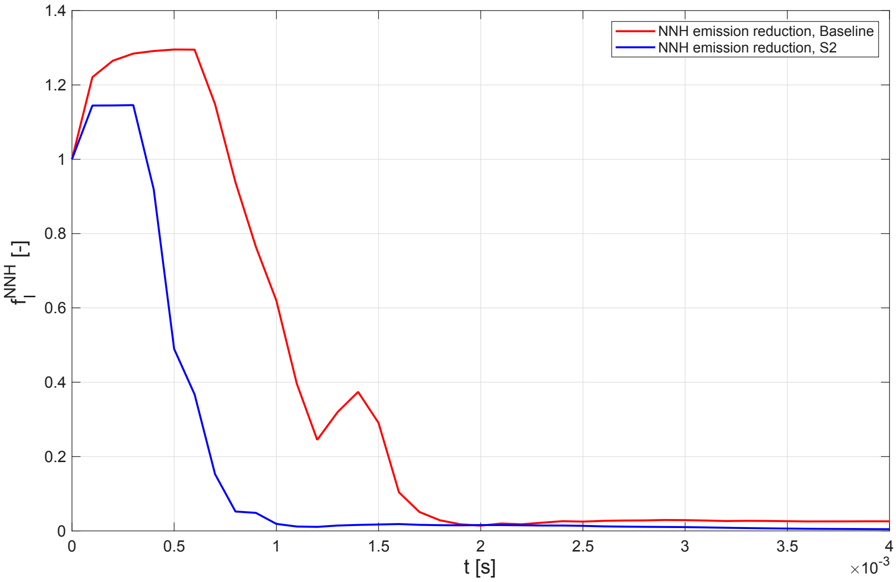

Figure 5.64: f_I^{NNH} Time history with Water Injection: Two Different Strains with Water Injection and integral of S2 case being based on a dry case with a $= 8000$ s^{-1} (see Table 4.4 and Table 4.5).

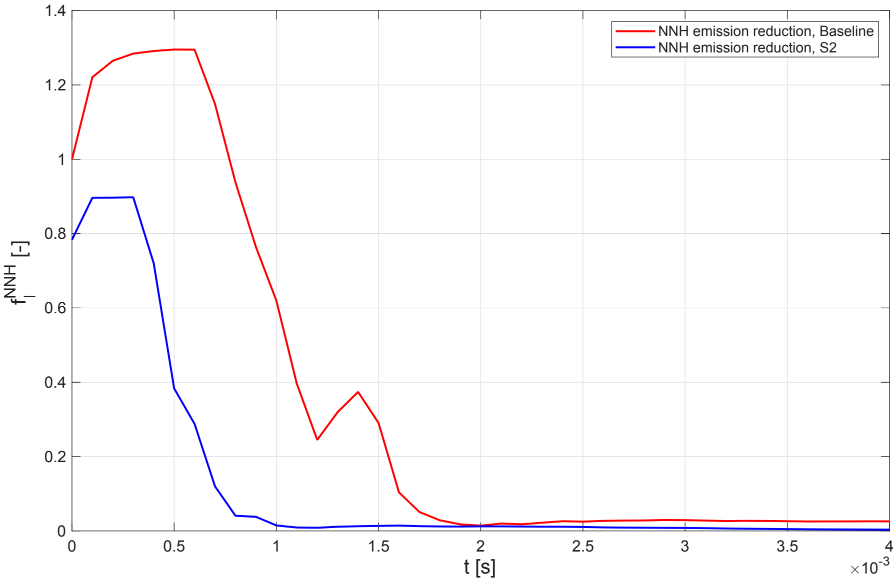

Figure 5.65: f_I^{NNH} Time history with Water Injection: Two Different Strains with Water Injection and integral of S2 case being based on the original dry case (see Table 4.4 and Table 4.5).

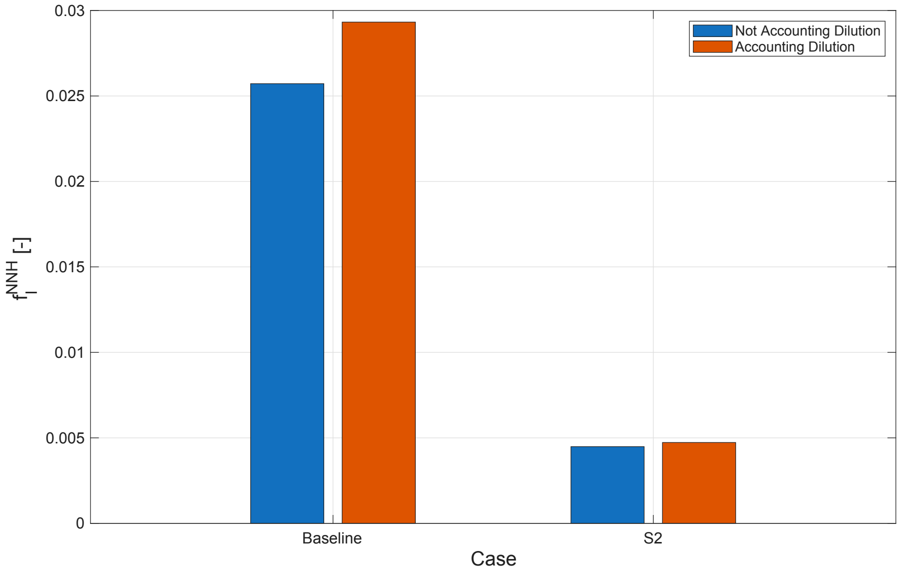

Figure 5.66: f_I^{NNH} value at t = 4 ms: Effect of Two Different Strains with Water Injection (see Table 4.4 and Table 4.5).

Figure 5.67 presents the distribution of the cell values for the NNH mass fractions for the baseline case and S2 in function of the hydrogen progress variable (expressed in Figure 5.67a) without accounting for dilution and correcting it for dilution (shown in Figure 5.67b). The observations done in the previous subsection regarding the changes in position of the reaction zone are corroborated by this figure: it is possible to observe that case S2 has its reaction zone at slightly higher values of $c(\mathrm{H}_2)$ the reaction is occurring slightly closer to the products zone. Moreover, it is possible to observe that compared to the previous cases analyzed in Figure 5.27 and Figure 5.47, only U20 presented a sharper reduction in Y_{NNH} than S2, which shows that coupling increasing strain with water injection proves to be very effective at reducing this species presence in the domain.

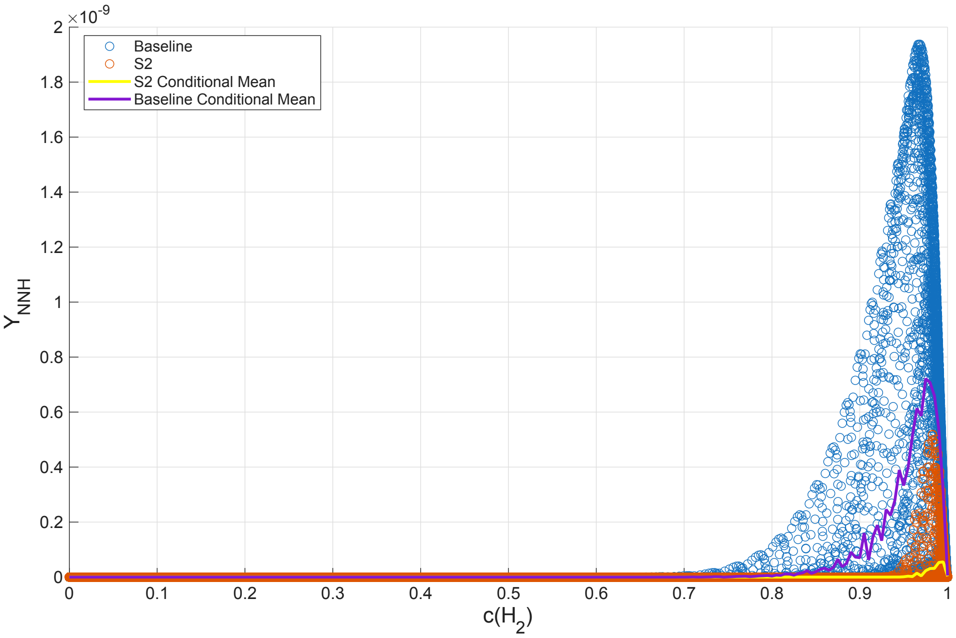

(a) NNH mass fraction distribution in function of $c(\mathrm{H}_2)$ at t = 4ms: Two Different Strains with Water Injection.

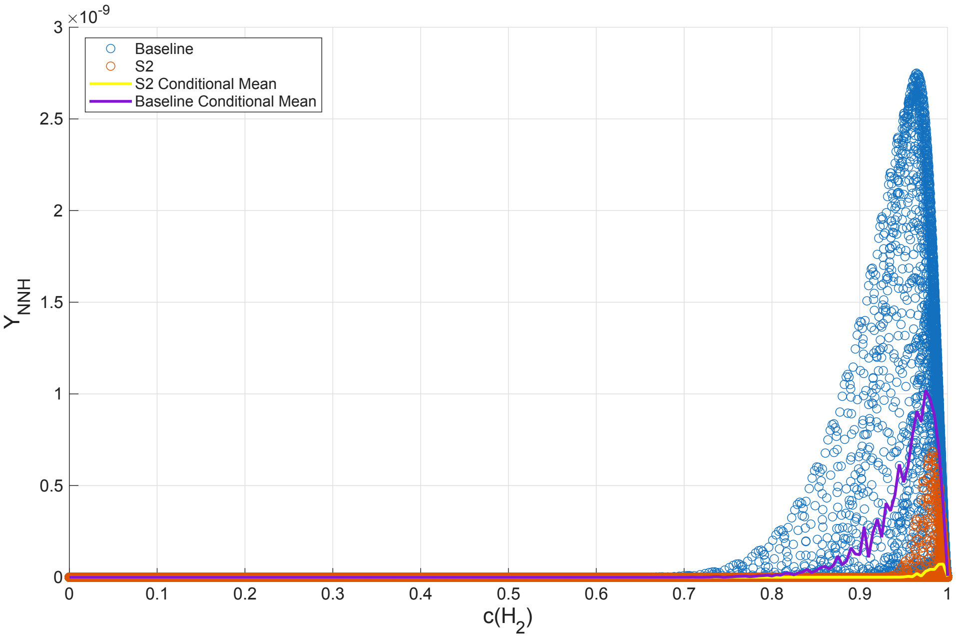

(b) NNH mass fraction distribution in function of $c(\mathrm{H}_2)$ at t = 4ms: Two Different Strains with Water Injection, accounting for dilution.

Figure 5.67: NNH mass fraction distribution in function of the hydrogen progress variable at t = 4ms: Two Different Strains with Water Injection.

Figure 5.68 and Figure 5.69 provide the variation of $f_I^{N_2O}$ across 4 ms for the baseline case and S2. For Figure 5.68 $f_I^{\mathrm{N_2O}}$ for the S2 case is calculated using a dry case with a strain rate equal to 8000 s^{-1} and according to the expression defined in Eq.(4.25), for Figure 5.69 $f_I^{\mathrm{N_2O}}$ is calculated using the original dry case $I_{\mathrm{N_2O}}$. This is done in order to isolate the impact caused by water injection and the impact of the increased strain rate on this specie's concentration. As it can be observed in Figure 5.68, a 79.6% drop in N_2O presence is verified for case S2 exclusively due to the injection of water, i.e, compared to a case without water injection and a strain rate, $a = 8000$ s^{-1}, the value of $f_I^{\mathrm{N_2O}}$ is 0.204. Moreover, it is observable in Figure 5.69 that coupling an increase in strain rate with water injection results in an overall decrease in N_2O presence of approximately 89.0%. The initial reduction in $I_{\mathrm{N_2O}}$ exclusively due to increasing the strain rate from 4000 s^{-1} to 8000 s^{-1} is of approximately 46.3%. As such, it is possible to infer that the reduction observed in N_2O presence is almost equal parts due to the effect of strain and water injection.

In Figure 5.70 the values for $f_I^{\mathrm{N_2O}}$ are presented at $t = 4$ ms, with and without account for dilution. It can be observed, the dilution effect accounts for a minor percentage of the emissions reduction observed, similar to what was observed in the cases where injection velocity and SMD were changed.

Overall, it can be observed that the emission reduction caused by injecting water is enhanced by the higher strain and coupled with the reduction in emissions caused by the higher strain, this results in an even more significant suppression of N_2O emissions.

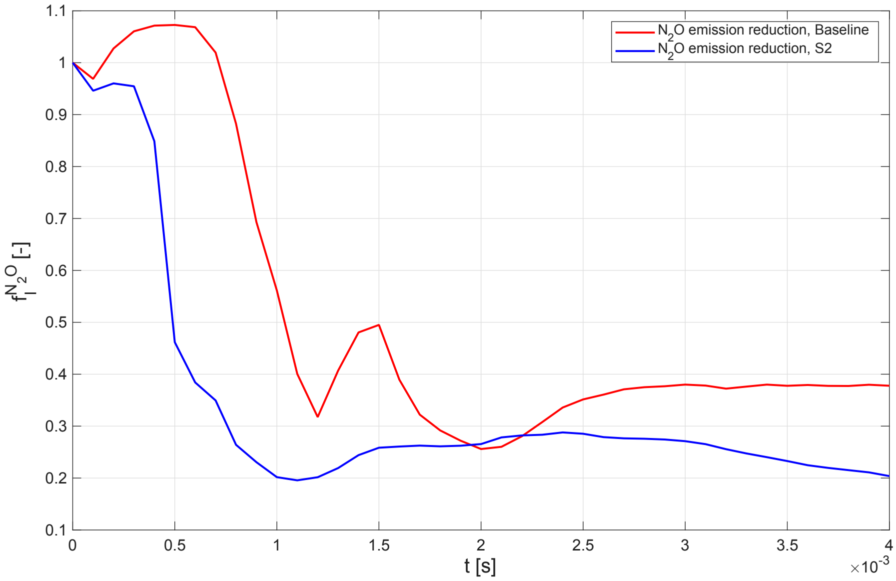

Figure 5.68: $f_I^{\mathrm{N_2O}}$ Time history with Water Injection: Two Different Strains with Water Injection and integral of S2 case being based on a dry case with a $= 8000$ s^{-1} (see Table 4.4 and Table 4.5).

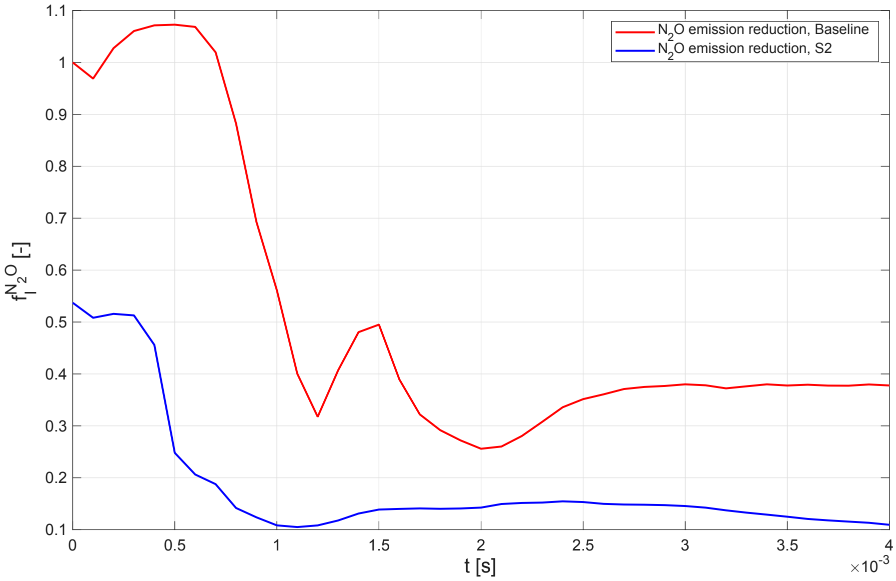

Figure 5.69: $f_I^{\mathrm{N_2O}}$ Time history with Water Injection: Two Different Strains with Water Injection and integral of S2 case being based on a dry case with a $= 8000$ s^{-1} (see Table 4.4 and Table 4.5).

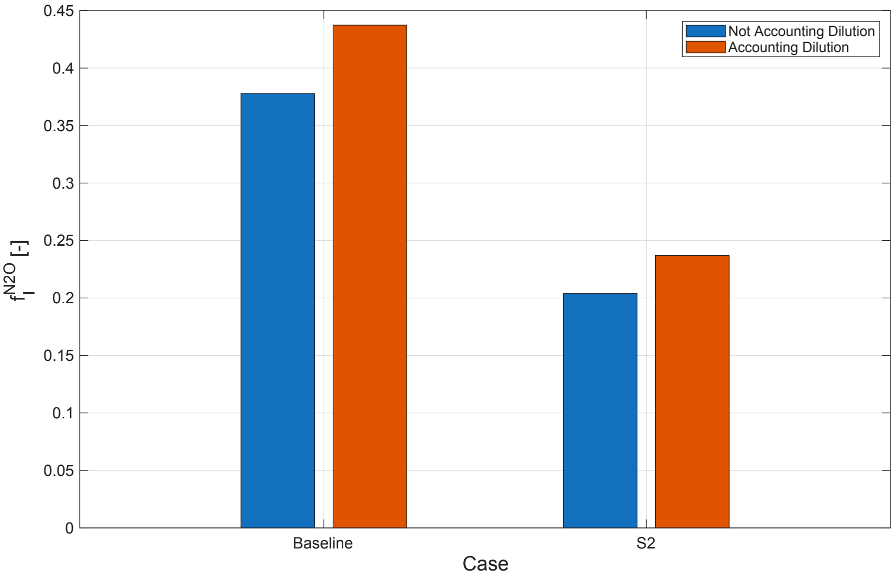

Figure 5.70: $f_I^{\mathrm{N_2O}}$ value at t = 4 ms: Effect of Two Different Strains with Water Injection (see Table 4.4 and Table 4.5).

Furthermore, Figure 5.71 shows the distribution of the cell values for the N_2O mass fractions for the baseline case and S2 in function of the hydrogen progress variable (expressed in Figure 5.71a) and in function of the hydrogen progress variable but with a correction to account for the dilution effect (shown in Figure 5.71b). It can be observed that a reduction in this species presence is observed for all values of c, but with a shaper decline being verified at latter values of progress variable. This is likely due to the deficit in O radicals observable in Figure 5.53, as the O radical is specially important for the formation of N_2O as discussed in section 2.1 and as [20, 17] discussed in their work.

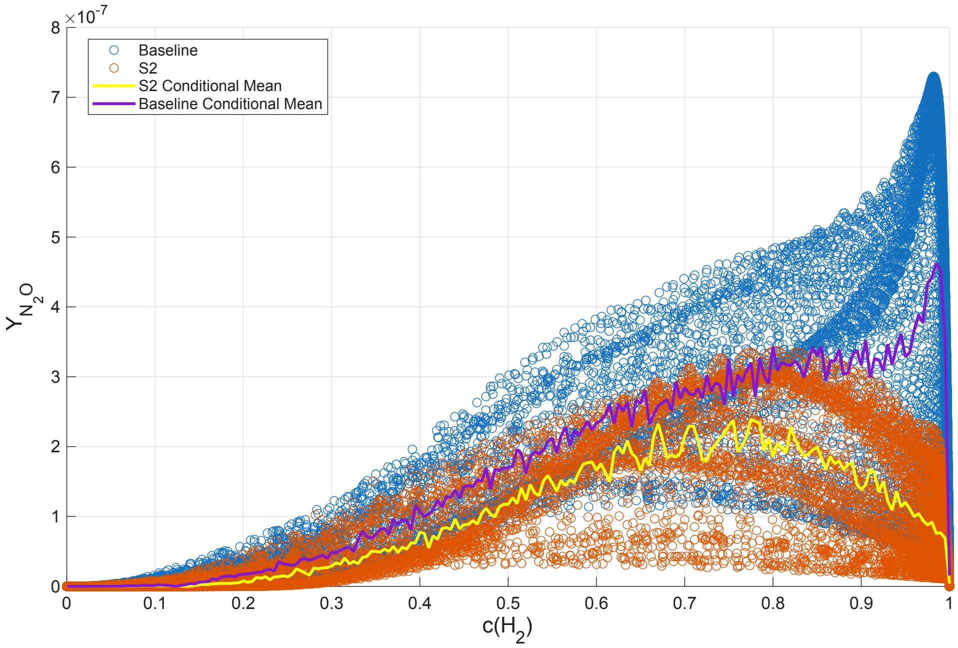

(a) N_2O mass fraction distribution in function of $c(\mathrm{H}_2)$ at t = 4ms: Two Different Strains with Water Injection.

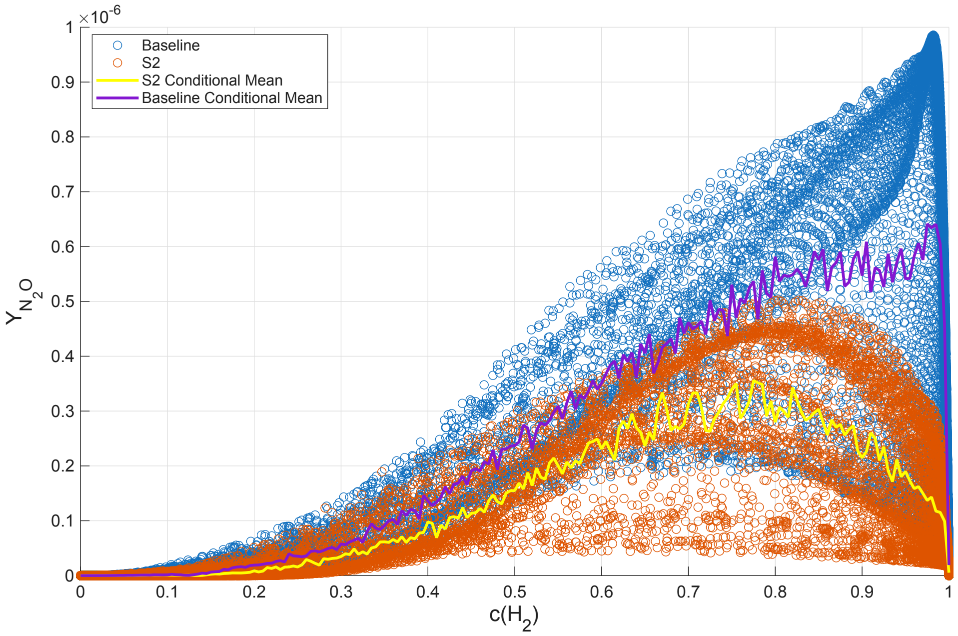

(b) N_2O mass fraction distribution in function of $c(\mathrm{H}_2)$ at t = 4ms: Two Different Strains with Water Injection, accounting dilution.

Figure 5.71: N_2O mass fraction distribution in function of the hydrogen progress variable at t = 4ms: Two Different Strains with Water Injection.

Figure 5.72 and Figure 5.73 provide the variation of f_I^{NO} across 4 ms for the baseline case and S2. For Figure 5.72 f_I^{NO} for the S2 case is calculated using a dry case with a strain rate equal to 8000 s^{-1} and according to the expression defined in Eq.(4.26), for Figure 5.73 f_I^{NO} is calculated using the original dry case I_{NO}. This is done in order to isolate the impact caused by water injection and the impact of the increased strain rate on this specie's concentration. As it can be observed in Figure 5.72, a 92.64% drop in f_I^{NO} is verified for case S2 exclusively due to the injection of water, i.e, compared to a case without water injection and a strain rate, $a = 8000$ s^{-1}, f_I^{NO} is reduced by 92.64%. Moreover, it is observable in Figure 5.73 that coupling an increase in strain rate with water injection results in an overall decrease in f_I^{NO} of approximately 97.48%. The initial reduction in I_{NO} exclusively due to increasing the strain rate from 4000 s^{-1} to 8000 s^{-1} is of approximately 65.8%. As such, it is possible to infer that the reduction observed in NO presence mostly due to the effects of increasing the strain of the flame from 4000 s^{-1} to 8000 s^{-1}. Nevertheless, from Figure 5.72 it is also possible to infer that the effects of water injection are more effective on the case with water injection than they are on the baseline case, even if the reduction observed is in its most part caused by the higher strain rate.

In Figure 5.74 the values for $f_I^{\mathrm{N_2O}}$ are presented at $t = 4$ ms, with and without account for dilution. It can be observed, the dilution effect accounts for a minor percentage of the emissions reduction observed, similar to what was observed in the cases where injection velocity and SMD were changed.

Overall, it can be observed that the emission reduction caused by injecting water is enhanced by the higher strain and coupled with the reduction in emissions caused by the higher strain, this results in an even more significant suppression of N_2O emissions.

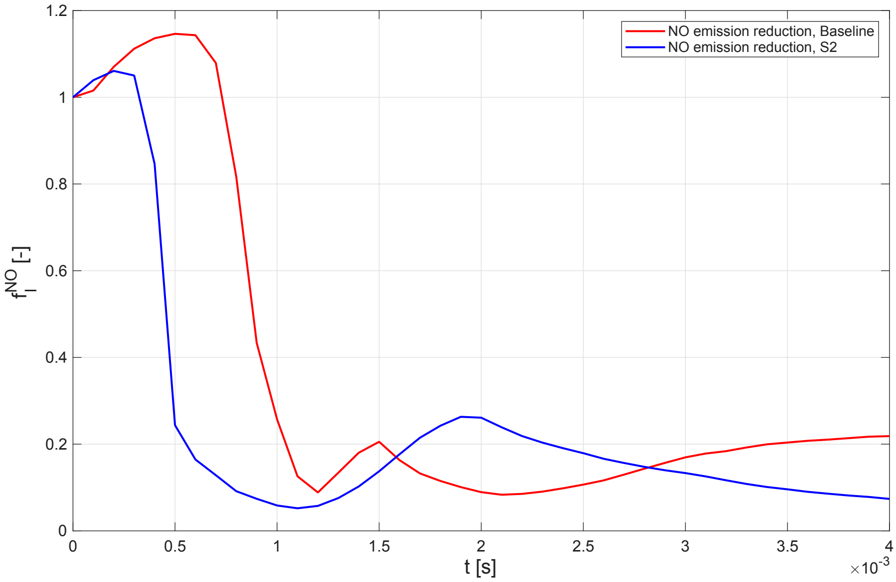

Figure 5.72: f_I^{NO} Time history with Water Injection: Two Different Strains with Water Injection and integral of S2 case being based on a dry case with a $= 8000$ s^{-1} (see Table 4.4 and Table 4.5).

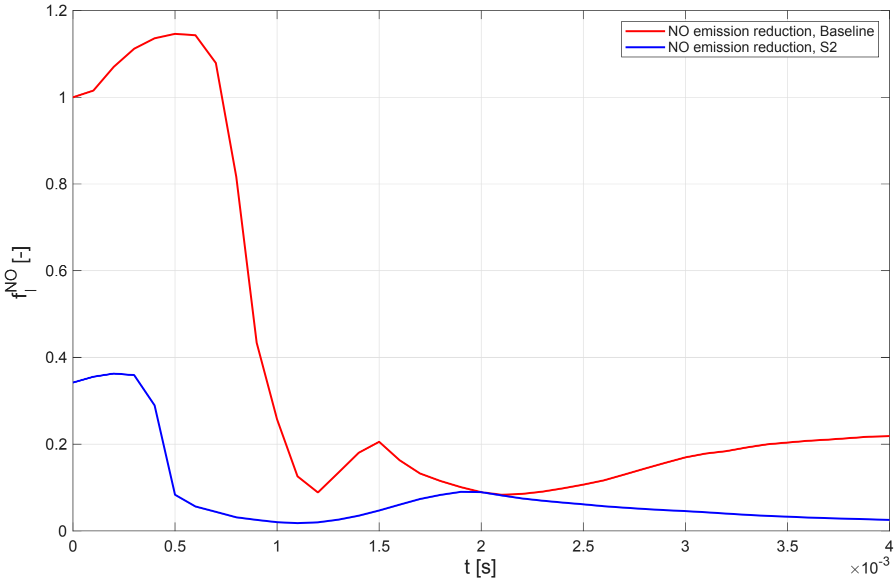

Figure 5.73: f_I^{NO} Time history with Water Injection: Two Different Strains with Water Injection and integral of S2 case being based on a dry case with a $= 8000$ s^{-1} (see Table 4.4 and Table 4.5).

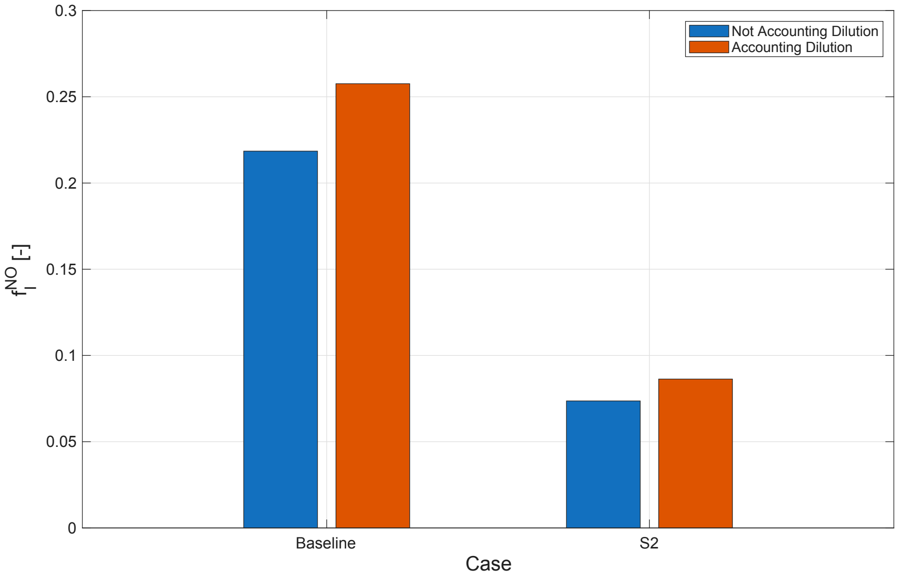

Figure 5.74: f_I^{NO} value at t = 4 ms: Effect of Two Different Strains with Water Injection (see Table 4.4 and Table 4.5).

Additionally, Figure 5.75 shows the distribution of the cell values for the NO mass fractions for the baseline case and S2 in function of the hydrogen progress variable (expressed in Figure 5.75a) and with a correction to account for the dilution effect (shown in Figure 5.75b). As it is observable, there is a reduction in this species presence observed for all values of c, but with a shaper decline being verified at latter values of progress variable. It is specially noticeable, that at high $c(\mathrm{H}_2)$ values there is no longer a peak for S2. This is likely due to the higher strain (as shown by [14] and [15]) coupled with the lower temperatures (verified in Figure 5.62) are extremely effective at reducing thermal NOx formation, whose mechanism was discussed in section 2.1. Moreover, [14] and [16] also identified OH and O radical presence of high importance for the formation of thermal NOx, and as observed in Figure 5.57 and Figure 5.53 the S2 case presents a considerable deficit in these radical's mass fractions, which significantly contribute to this NOx formation pathway suppression. As such, it is possible to conclude that this combination of emission suppression strategies is effective for all NOx formation mechanism, as observed due to the reduction in NO across the entire array of progress variable values, but is specially effective at suppressing thermal NO.

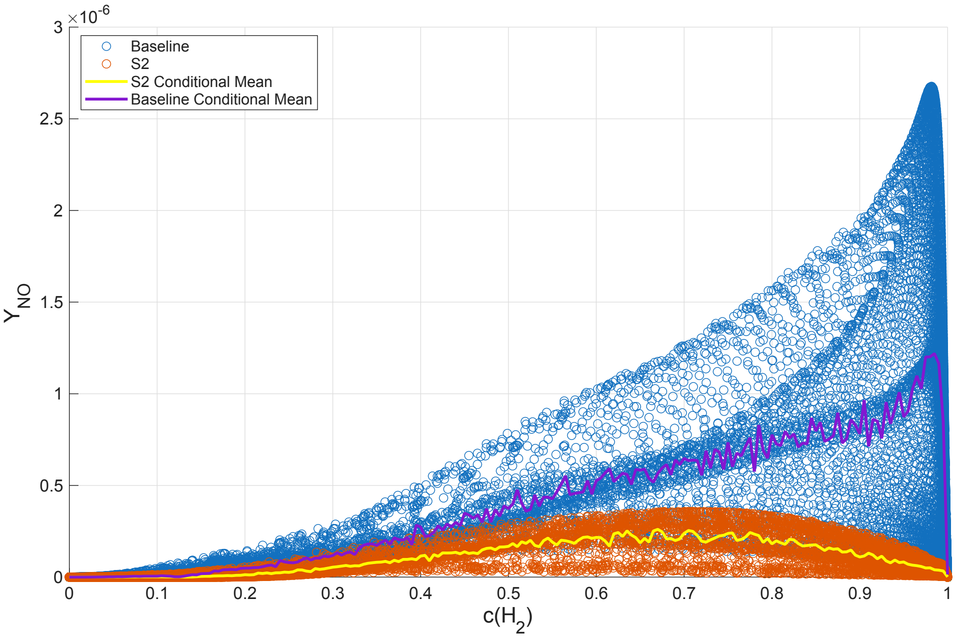

(a) NO mass fraction distribution in function of $c(\mathrm{H}_2)$ at t = 4ms: Two Different Strains with Water Injection.

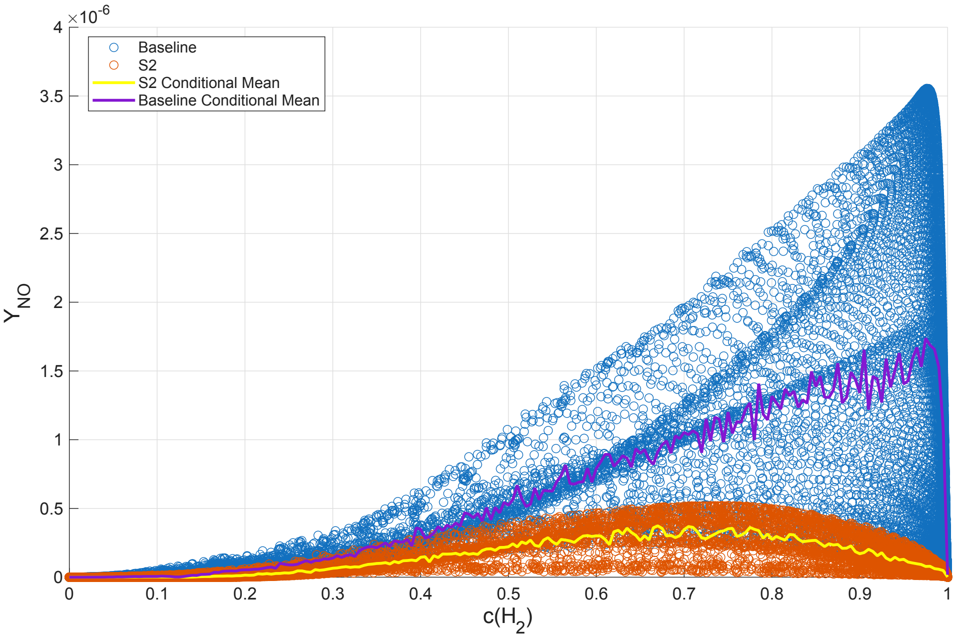

(b) NO mass fraction distribution in function of $c(\mathrm{H}_2)$ at t = 4ms: Two Different Strains with Water Injection, accounting for dilution.

Figure 5.75: NO mass fraction distribution in function of both progress variables at t = 4ms: Two Different Strains with Water Injection.

6

Conclusions and Next Steps

This thesis project was conducted with the aim to qualitatively and quantitatively analyze the effect of water injection on highly strained premixed laminar hydrogen flames through the use of computational methods and in this way infer about the possibility of combining this two methods in order to reduce NOx emissions in hydrogen combustion. This chapter aims to provide a synthesis of the results and observations obtained through computational analysis of different simulation setups in order to answer the research questions defined in chapter 3. For that purpose, in this section, these research questions will be revisited and an answer to them based on the attained results will be given. Then, to conclude the chapter, several recommendations for future work based on the present research will be given to guide future research on the thesis topic.

First, a baseline case was analyzed. The results for the baseline case show an immediate reduction of the presence of O, H, and OH radicals of around approximately 93%, 95%, and 71%, respectively when not accounting for dilution and 91%, 93%, and 69% when a correction is applied to account for dilution effect when compared to the dry case. However, an increase in HO_2 radicals is also observed due to changes in the chemical pathways due to the presence of water, which has a positive impact on emissions since it's less reactive then the aforementioned radicals. A sharp decrease in hydrogen rate of consumption and temperature is observed in this case. The mean temperature decrease observed after 4 ms exceeds 300 K and the consumption rate of hydrogen also decreases from 14.5 kg/(m^3s) to approximately 0.45 kg/(m^3s) in the same time period. Regarding the emissions of NOx related species, reductions of approximately 97.1%, 56.3%, and 74.2% were verified for the gain figures used to study the emissions of NNH, N_2O, and NO once dilution is accounted for, respectively.

The first research sub-question concerns the impact of water injection velocity on NOx emissions and flame structure of highly strained hydrogen flames. The results from this research concluded that with increasing injection velocity the presence of the key radicals mentioned in the last paragraph is reduced even further. Comparing to the case without water injection, the reduction in O, H, and OH was of 95.3%, 98.0%, and 79.3% (accounting for dilution), respectively, when increasing the injection velocity from 5% to 10% of the reactants injection velocity. Similarly, when increasing from 5% to 20%, a reduction of O radicals of 98.4% , a reduction of H radicals of 99.5%, and a reduction of OH radicals of89.1% was verified when also accounting for dilution. Regarding HO_2, the mass fraction values remain similar between the two cases with lower injection velocity, but once velocity is increased to 20% of the reactants injection velocity it diminishes significantly, likely due to the changes observed in hydrogen reactivity and flame temperature. Similarly to the trend verified for the radicals, increasing velocity of injection also results in a reduction in hydrogen rate of consumption and temperature. Moreover, the emissions of NOx related species also were significantly reduced, with the case with water injection velocity equal to 10% of the reactants injection velocity exhibiting reductions in the gain figures used to study the emissions of NNH, N_2O, and NO of 99.0%, 68.5%, and 89.5%, whilst the case with water injection velocity equal to 20% of the reactants injection velocity having reductions of 99.6%, 86.0%, and 97.1% of the same parameters. It was also noted that the reductions observed for N_2O and NO occurred mostly at later values of hydrogen progress variable, whilst at lower values of hydrogen progress variable a slight increase was observed. From these observations coupled with the reductions in reactivity and temperature found, it was concluded that the main NOx formation mechanism being suppressed was the thermal NOx pathway. The observed reductions in radical mass fraction and emissions of NOx related species as injection velocity is increased are likely tied to the increasing relative velocity between the droplet and the surrounding flow, which directly affects the droplet Reynolds number. Moreover, since the Reynolds number governs the convective heat and mass transfer around the droplet, a higher relative velocity leads to enhanced evaporation rates due to stronger convective effects.

The second research sub-question concerns the impact of varying droplet diameters on NOx emissions and flame structure of highly strained hydrogen flames. The results from this research concluded that with increasing diameter the presence of the key radicals mentioned in the last paragraph is slightly reduced. Comparing to the baseline case, the reduction in O, H, and OH when increasing the standard mean diameter (SMD) by 25% was of 8.0%, 17.5%, and 7.0%, respectively. Similarly, when increasing SMD by 15%, a reduction of O radicals of H radicals, and a reduction of OH radicals was verified, but slightly less considerable than the ones observed for the previous case. Regarding HO_2, a small increased scaling with increasing SMD is observed. An average temperature reduction of 8 K and 18 K was found when increasing the SMD by 15% and 25%, respectively with a decrease in hydrogen rate of consumption as well. The changes is rate of consumption are relatively larger than the ones in temperature. These changes are likely tied to the larger diameter requiring a larger amount of energy to evaporate and in doing so evaporate closer to the flame front as well, resulting in a small decrease of flame temperature and a small decrease in hydrogen reactivity. Due to this, a reduction in the gain figures used to study the emissions of NNH, N_2O, and NO of 97.5%, 58.7%, and 74.6% for the case where SMD is increased by 15% and a reduction in the gain figures used to study the emissions of NNH, N_2O, and NO of 97.6%, 59.2%, and 80.4% when SMD is increased by 25%. It is important to note that the decreases in NO mass fractions observed occur mostly at later values of hydrogen progress variable, which indicates that the main mechanism being suppressed when droplet diameter is incremented is also the thermal NOx pathway.

Finally, the third research sub-question concerns the impact of flame strain increment on NOx emissions and flame structure of highly strained hydrogen flames. In order to do that an additional case was considered where the strain rate of the flame was doubled from the baseline case, but the injected water mass loading was kept constant. The results show a sharper reduction in ceO, H, OH, and HO_2 radicals once coupling water injection with a higher flame strain, with the mass fractions of these species being reduced further than the baseline case, even though at the initial time step they concentration was higher. Similarly, coupling water injection with a higher strain, resulted in sharper decreases in hydrogen consumption rate and temperature. Due to the reductions in temperature, consumption rate and radical presence, this case with higher flame strain rate demonstrated even sharper reductions in the gain figures used to study the emissions of NNH, N_2O, and NO. To separately analyze the effects of increasing strain rate and the coupling of water injection with increased strain rate the analysis was done for two different methods of computing the gain figures: in the first the gain figures of the case with higher strain was computed based on a dry case with flame strain rate $a = 8000$ s$^-1$; whilst in the second case the same gain figures were computed based on the original dry case with $a = 4000$ s$^-1$. The results revealed that the benefits of water injection in hydrogen flames is coupled with increasing strain, i.e, the benefits of emission reduction are increased for higher strain rates and the same water loading being injected. It was also possible to conclude that water the majority of NNH emission reductions found was due to the injection of water, while for NO this patterned is reversed. For N_2O both methods contribute similarly, with strain rate being very slightly more important at reducing this species emissions. Overall, this thesis project aimed to qualitatively and quantitatively analyze the effect of water injection on highly strained premixed laminar hydrogen flames through the use of computational methods and in this way infer about the possibility of combining these two methods in order to reduce NOx emissions in hydrogen combustion and in this regard it was possible to conclude, based on the results obtained, that the benefits of water injection in highly strained hydrogen counter flow flames under laminar conditions seem to be more effective in flames where the strain is higher.

6.1. Recommendations & Next Steps

Several recommendations for future work are outlined below:

- **Expand the array of conditions studied.** In this work only three different injection velocities, three different SMD values and 2 different strain rates were analyzed. Future research could be done in order to cover a wider array of values to ensure that the observed trends and results are kept as these parameters are varied even further.
- **Extend the research to turbulent conditions**. The research done in this thesis was limited to laminar counter-flow hydrogen flames. As such, to analyze how highly strained hydrogen turbulent flames interact with water injection it is necessary to expand on the research done and conducted further computational analysis under turbulent conditions.
- **Acquire experimental data on the effects of water injection in highly strained hydrogen flames.** In order to compared the results of this research and future works it might be productive to conduct experimental analysis in a controlled environment in order to properly validate the results and model used in this and further researches.
- **Analyze the effects of water injection on preferential diffusion.** An attempt to do this was done for this project, however it proved to be impossible to compare the results on preferential diffusion between the dry cases and the cases with water injection due to the dilution effect. Attempts were made to mitigate said dilution effect, but it proved impossible to do so with the present data sets. As such, it might be beneficial for future research an analysis on the impact of water injection on hydrogen preferential diffusion.

References

[1] International Energy Authority. *World Energy Outlook*. en. Tech. rep. International Energy Authority, Oct. 2023.

[2] I.S. Anufriev. “Review of water/steam addition in liquid-fuel combustion systems for NOx reduction: Waste-to-energy trends”. In: *Renewable and Sustainable Energy Reviews* 138 (Mar. 2021), p. 110665. DOI: `10.1016/j.rser.2020.110665`.

[3] Christoph Gatzen. *The economics of power storage: Theory and empirical analysis for central Europe*. de. Ed. by Energiewirtschaftliches Energiewirtschaftliches Institut. Munchen, Germany: Deutscher Industrieverlag, 2008.

[4] Daniel Kroniger. “Prediction of NOx Emissions for a Hydrogen Fueled Industrial Gas Turbine Combustor with Water Injection”. en. MA thesis. Aachen: Rheinisch-Westfälische Technische Hochschule Aachen, 2019.

[5] Nicolas G. M. Moirou, Drewan S. Sanders, and Panagiotis Laskaridis. “Advancements and prospects of boundary layer ingestion propulsion concepts”. en. In: *Progress in aerospace sciences* 138.100897 (2023), p. 100897. ISSN: 0376-0421. DOI: `10.1016/j.paerosci.2023.100897`. URL: `http://dx.doi.org/10.1016/j.paerosci.2023.100897`.

[6] Gregg G Fleming, Ivan de Lépinay, and Roger Schaufele. “CHAPTER ONE Aviation & Environmental Outlook : Environmental Trends in Aviation to 2050”. en. In: *ICAO Environmental Report*. International Civil Aviation Organization, 2022.

[7] Xiting Wang, Ai He, and Zhongzhi Hu. “Transient modeling and performance analysis of hydrogen-fueled Aero engines”. en. In: *Processes (Basel)* 11.2 (2023), p. 423.

[8] Guy Norris. *Pratt outlines hydrogen steam-injection engine concept*. en. Apr. 2022. URL: `https://aviationweek.com/special-topics/sustainability/pratt-outlines-hydrogen-steam-injection-engine-concept`.

[9] Xiaoxiao Sun et al. *Final report for the single sector H2 micromix combustor segment performance and NOx emissions assessment*. en. 2023. DOI: `10.3030/769241`. URL: `https://cordis.europa.eu/project/id/769241/results`.

[10] L Das. “Hydrogen-oxygen reaction mechanism and its implication to hydrogen engine combustion”. In: *International Journal of Hydrogen Energy* 21.8 (Aug. 1996), pp. 703–715. DOI: `10.1016/0360-3199(95)00138-7`.

[11] Mohamed Mohamed et al. “Exploring the benefits of hydrogen-water injection technology in internal combustion engines: A rigorous experimental study”. In: *International Journal of Engine Research* 0.0 (0). DOI: `10.1177/14680874241288624`. eprint: `https://doi.org/10.1177/14680874241288624`. URL: `https://doi.org/10.1177/14680874241288624`.

[12] Marcus Ó Conaire et al. “A comprehensive modeling study of hydrogen oxidation”. In: *International Journal of Chemical Kinetics* 36.11 (Aug. 2004), pp. 603–622. DOI: `10.1002/kin.20036`.

[13] A. Banerjee et al. “The effects of steam and water spray addition on nox emissions from a combustor using simple reactor models”. In: *Lecture Notes in Mechanical Engineering* (2023), pp. 521–526. DOI: `10.1007/978-981-19-6970-6_87`.

[14] Alessandro Porcarelli, Boris Kruljević, and Ivan Langella. “Suppression of NOx emissions by intensive strain in lean premixed hydrogen flamelets”. In: *International Journal of Hydrogen Energy* 49 (Jan. 2024), pp. 413–431. DOI: `10.1016/j.ijhydene.2023.08.110`.

[15] Tian Fang Xie and Pei Yong Wang. “Analysis of NO formation in counterflow premixed hydrogen-air flame”. In: *Applied mechanics and materials* 284–287 (2013), pp. 601–607. ISSN: 1660-9336. DOI: `10.4028/www.scientific.net/amm.284-287.601`. URL: `http://dx.doi.org/10.4028/www.scientific.net/amm.284-287.601`.

[16] Peter Glarborg et al. “Modeling nitrogen chemistry in combustion”. In: *Progress in Energy and Combustion Science* 67 (July 2018), pp. 31–68. DOI: `10.1016/j.pecs.2018.01.002`.

[17] Pablo Rouco Pousada. “Reheat Hydrogen Combustion with Water Injection at High Pressures: Sensitivity and Flashback Analysis”. en. MA thesis. Delft: Technische Universität Delft, 2023.

[18] Craig T. Bowman. “Control of combustion-generated nitrogen oxide emissions: Technology driven by regulation”. In: *Symposium (International) on Combustion* 24.1 (Jan. 1992), pp. 859–878. DOI: `10.1016/s0082-0784(06)80104-9`.

[19] VIttorio De Lauso. “Hydrogen-Enriched Methane Flames in a Swirl Stabilized Combustor with Axial Air Injection”. en. MA thesis. Delft: Technische Universität Delft, 2024. URL: `https://resolver.tudelft.nl/uuid:5d233be1-d8bb-4369-bd2e-6ed5278fb8eb`.

[20] *An Experimental and Modeling Study of Humid Air Premixed Flames*. Vol. Volume 2: Coal, Biomass and Alternative Fuels; Combustion and Fuels; Oil and Gas Applications; Cycle Innovations. Turbo Expo. June 1999, V002T02A002. DOI: `10.1115/99-GT-008`. eprint: `https://asmedigitalcollection.asme.org/GT/proceedings-pdf/GT1999/78590/V002T02A002/4218300/v002t02a002-99-gt-008.pdf`. URL: `https://doi.org/10.1115/99-GT-008`.

[21] Jrgen Warnatz, Ulrich Maas, and Robert W. Dibble. *Combustion: Physical and chemical fundamentals, modeling and simulation, experiments, pollutant formation*. en. 4th ed. Berlim, Germany: Springer, 2006. ISBN: 9783540453635.

[22] Marc S. Day et al. “Numerical simulation of nitrogen oxide formation in lean premixed turbulent H2/O2/N2 flames”. en. In: *Proceedings of the Combustion Institute. International Symposium on Combustion* 33.1 (2011), pp. 1591–1599. ISSN: 1540-7489. DOI: `10.1016/j.proci.2010.06.128`. URL: `http://dx.doi.org/10.1016/j.proci.2010.06.128`.

[23] C.P. Fenimore. “Formation of nitric oxide in premixed hydrocarbon flames”. In: *Symposium (International) on Combustion* 13.1 (Jan. 1971), pp. 373–380. DOI: `10.1016/s0082-0784(71)80040-1`.

[24] James A. Miller and Craig T. Bowman. “Mechanism and modeling of nitrogen chemistry in combustion”. In: *Progress in Energy and Combustion Science* 15.4 (Jan. 1989), pp. 287–338. DOI: `10.1016/0360-1285(89)90017-8`.

[25] Riccardo Concetti et al. “Effects of liquid water addition on turbulent premixed hydrogen/air combustion”. In: *Fuel* 373 (Oct. 2024), p. 132314. DOI: `10.1016/j.fuel.2024.132314`.

[26] J Richard et al. “Chemical and physical effects of water vapor addition on diffusion flames”. en. In: *Fire Saf. J.* 38.6 (2003), pp. 569–587.

[27] Colette Nicoli, Pierre Haldenwang, and Bruno Denet. “Premixed flame dynamics in presence of mist”. en. In: *Combust. Sci. Technol.* 191.2 (2019), pp. 197–207.

[28] A M Lentati and H K Chelliah. “Dynamics of water droplets in a counterflow field and their effect on flame extinction”. en. In: *Combust. Flame* 115.1-2 (1998), pp. 158–179.

[29] T. Le Cong and P. Dagaut. “Experimental and Detailed Modeling Study of the Effect of Water Vapor on the Kinetics of Combustion of Hydrogen and Natural Gas, Impact on NO$_x$”. In: *Energy & amp; Fuels* 23.2 (Jan. 2009), pp. 725–734. DOI: `10.1021/ef800832q`.

[30] Tim C Lieuwen. *Unsteady combustor physics*. en. 2nd ed. Cambridge, England: Cambridge University Press, 2021.

[31] J Fritz, M Kröner, and T Sattelmayer. “Flashback in a swirl burner with cylindrical premixing zone”. en. In: *J. Eng. Gas Turbine. Power* 126.2 (2004), pp. 276–283.

[32] G. Willems (author) , S. A. Klein (mentor) , M. J. Tummers (mentor). “Unraveling Flashback Phenomena of Turbulent premixed Hydrogen-Natural Gas-Air Flames”. en. MA thesis. TU Delft, 2022.

[33] Alireza Kalantari and Vincent McDonell. “Boundary layer flashback of non-swirling premixed flames: Mechanisms, fundamental research, and recent advances”. en. In: *Prog. Energy Combust. Sci.* 61 (2017), pp. 249–292.

[34] Ali Cemal Benim and Khawar J. Syed. *Flashback Mechanisms in Lean Premixed Gas Turbine Combustion*. en. Academic Press, 2015. DOI: `10.1016/C2013-0-18847-2`.

[35] Alessio Pappa et al. “Can Water Dilution Avoid Flashback on a HydrogenEnriched Micro-Gas Turbine Combustion?—A Large Eddy Simulations Study”. en. In: *Journal of Engineering for Gas Turbines and Power* 143 (2021).

[36] Pablo Rouco Pousada et al. “Flashback prevention in a hydrogen-fueled reheat combustor by water injection optimized with global sensitivity analysis”. In: *Volume 3B: Combustion, Fuels, and Emissions*. American Society of Mechanical Engineers, 2024.

[37] Timothy C. Lieuwen and Vigor Yang. *Gas Turbine Emissions*. en. Cambridge University Press, 2013. ISBN: 978-0-521-76405-6. URL: `https://app.knovel.com/hotlink/khtml/id:kt00C3UYV9/gas-turbine-emissions/thermal-no`.

[38] Ashley Sharkey and Ali Zare. “The Impact of Water Injection and Hydrogen Fuel on Performance and Emissions in a Hydrogen/Diesel Dual-Fuel Engine”. In: *Energies* 17.23 (Nov. 2024), p. 5838. DOI: `10.3390/en17235838`.

[39] Ricardo Novella et al. “Numerical assessment of water injection for improved thermal efficiency and emissions control in a medium-duty hydrogen engine for transportation applications”. In: *Fuel* 359 (Mar. 2024), p. 130455. DOI: `10.1016/j.fuel.2023.130455`.

[40] Puyan Xu et al. “Effects of direct water injection on engine performance in engine fueled with hydrogen at varied excess air ratios and spark timing”. In: *Fuel* 269 (June 2020), p. 117209. DOI: `10.1016/j.fuel.2020.117209`.

[41] Denis Veynante and Thierry Poinsot. *Theoretical and numerical combustion*. en. Afnil, 2022. ISBN: 9782746639904.

[42] Alessandro Porcarelli and Ivan Langella. “Mitigation of preferential diffusion effects by intensive strain in lean premixed hydrogen flamelets”. In: *Proceedings of the Combustion Institute* 40.1-4 (Jan. 2024), p. 105728. DOI: `10.1016/j.proci.2024.105728`.

[43] Hongchao Chu et al. “Effects of differential diffusion on hydrogen flame kernel development under engine conditions”. In: *Proceedings of the Combustion Institute* 39.2 (2023), pp. 2129–2138. ISSN: 1540-7489. DOI: `https://doi.org/10.1016/j.proci.2022.07.042`.

[44] Faizan Habib Vance et al. “Flame Stabilization and Blow-Off of Ultra-Lean H2-Air Premixed Flames”. In: *Energies* 14.7 (Apr. 2021), p. 1977. DOI: `10.3390/en14071977`.

[45] Eun-Seong Cho and Suk Ho Chung. “Improvement of flame stability and NOx reduction in hydrogen-added ultra lean premixed combustion”. In: *Journal of Mechanical Science and Technology* 23.3 (Mar. 2009), pp. 650–658. DOI: `10.1007/s12206-008-1223-x`.

[46] Daoguan Ning, Aiwu Fan, and Hong Yao. “Effects of fuel composition and strain rate on NO emission of premixed counter-flow H2/CO/air flames”. In: *International Journal of Hydrogen Energy* 42.15 (Apr. 2017), pp. 10466–10474. DOI: `10.1016/j.ijhydene.2016.12.059`.

[47] Gregory S. Jackson et al. “Influence of H2 on the response of lean premixed CH4 flames to high strained flows”. In: *Combustion and Flame* 132.3 (Feb. 2003), pp. 503–511. DOI: `10.1016/s0010-2180(02)00496-0`.

[48] Mohamad Fathi et al. “Effects of intense strain on flame structure and NOx generation in turbulent counterflow lean-premixed hydrogen flames”. In: *Combustion and Flame* 282 (2025), p. 114459. ISSN: 0010-2180. DOI: `https://doi.org/10.1016/j.combustflame.2025.114459`.

[49] J. Serrano, F.J. Jiménez-Espadafor, and A. López. “Analysis of the effect of the hydrogen as main fuel on the performance of a modified compression ignition engine with water injection”. In: *Energy* 173 (Apr. 2019), pp. 911–925. DOI: `10.1016/j.energy.2019.02.116`.

[50] *Alternative Fuel*. en. URL: `https://www.rtx.com/en/prattwhitney/future-of-flight/alternative-fuel`.

[51] Antonio L. Sánchez and Forman A. Williams. “Recent advances in understanding of flammability characteristics of hydrogen”. In: *Progress in Energy and Combustion Science* 41 (Apr. 2014), pp. 1–55. DOI: `10.1016/j.pecs.2013.10.002`.

[52] T. Capurso et al. “NO_x pathways in lean partially premixed swirling H2air turbulent flame”. In: *Combustion and Flame* 248 (Feb. 2023), p. 112581. DOI: `10.1016/j.combustflame.2022.112581`.

[53] W Yang and R Kee. “The effect of monodispersed water mists on the structure, burning velocity, and extinction behavior of freely propagating, stoichiometric, premixed, methane-air flames”. en. In: *Combust. Flame* 130.4 (2002), pp. 322–335.

[54] Abhijit U Modak et al. “The effect of mono-dispersed water mist on the suppression of laminar premixed hydrogen–, methane–, and propane–air flames”. en. In: *Combust. Flame* 144.1-2 (2006), pp. 103–111.

[55] Anish Pal. “Risk Assessment Of SARS-COV-2 Due To Respiratory Droplet Transmission Inside An Elevator Under Various Climatic Conditions And Ventilation Scenarios”. en. PhD thesis. Kolkata: Jadavpur University, 2022.

[56] P.Aarne Vesilind. “The Rosin-Rammler particle size distribution”. In: *Resource Recovery and Conservation* 5.3 (Sept. 1980), pp. 275–277. DOI: `10.1016/0304-3967(80)90007-4`.

[57] Christopher M. Douglas et al. “Pollutant Emissions Reporting and Performance Considerations for Hydrogen–Hydrocarbon Fuels in Gas Turbines”. In: *Journal of Engineering for Gas Turbines and Power* 144.9 (July 2022), p. 091003. ISSN: 0742-4795. DOI: `10.1115/1.4054949`. eprint: `https://asmedigitalcollection.asme.org/gasturbinespower/article-pdf/144/9/091003/6901076/gtp_144_09_091003.pdf`. URL: `https://doi.org/10.1115/1.4054949`.

[58] Harshit Gupta, Omkejan J. Teerling, and Jeroen A. van Oijen. “Effect of progress variable definition on the mass burning rate of premixed laminar flames predicted by the Flamelet Generated Manifold method”. In: *Combustion Theory and Modelling* 25.4 (May 2021), pp. 631–645. DOI: `10.1080/13647830.2021.1926544`.

[59] Josef Hasslberger et al. “Physical effects of water droplets interacting with turbulent premixed flames: A Direct Numerical Simulation analysis”. In: *Combustion and Flame* 229 (July 2021), p. 111404. DOI: `10.1016/j.combustflame.2021.111404`.

[60] David G. Goodwin et al. *Cantera: An Object-oriented Software Toolkit for Chemical Kinetics, Thermodynamics, and Transport Processes*. `https://www.cantera.org`. Version 3.2.0. 2025. DOI: `10.5281/zenodo.17620923`.

[61] OpenFOAMFoundation. *OpenFOAM User Guide*. Version 6. 2018.

[62] Maria Rosaria Acquaviva, Alessandro Porcarelli, and Ivan Langella. “Influence of Soret effect on flame structure and NOx emissions in highly strained lean premixed counterflow hydrogen flames”. In: *Fuel* 395 (Sept. 2025), p. 134939. DOI: `10.1016/j.fuel.2025.134939`.

[63] Lukas Berger, Antonio Attili, and Heinz Pitsch. “Synergistic interactions of thermodiffusive instabilities and turbulence in lean hydrogen flames”. In: *Combustion and Flame* 244 (Oct. 2022), p. 112254. DOI: `10.1016/j.combustflame.2022.112254`.

[64] James Ahrens, Berk Geveci, and Charles Law. “ParaView: An End-User Tool for Large Data Visualization”. In: *Visualization Handbook*. ISBN 978-0123875822. Elesvier, 2005.

[65] Raymond L. Speth and Ahmed F. Ghoniem. “Using a strained flame model to collapse dynamic mode data in a swirl-stabilized syngas combustor”. In: *Proceedings of the Combustion Institute* 32.2 (Jan. 2009), pp. 2993–3000. DOI: `10.1016/j.proci.2008.05.072`.